EFFECT OF PLAGIOCLASE CRYSTALLIZATION ON LIQUID AND MAGMA VISCOSITY IN THE ANORTHITE-DIOPSIDE-FORSTERITE-QUARTZ SYSTEM

A Thesis presented to the Faculty of the Graduate School
University of Missouri-Columbia

In Partial Fulfillment
of the Requirements for the Degree

Masters of Science

---

by
JACKIE GETSON

Dr. Alan G. Whittington, Thesis Supervisor

AUGUST 2006

The undersigned, appointed by the Dean of the Graduate School, have examined the thesis entitled:

EFFECT OF PLAGIOCLASE CRYSTALLIZATION ON LIQUID AND MAGMA VISCOSITY IN THE ANORTHITE-DIOPSIDE-FORSTERITE-QUARTZ SYSTEM

Presented by Jackie Getson

a candidate for the degree of Master of Science

And hereby certify that in their opinion it is worthy of acceptance.

_____

Alan G. Whittington

_____

Carol Wicks

_____

Steve Lombardo

To Dad-

For being the first person to spark my interest in science and letting me run with it.

"No day in which you learn something is a complete loss."
Belgarath, the Eternal Man
David Eddings

ACKNOWLEDGEMENTS

The completion of this work is due to more than just the effort of the author, and for this reason I must thank a number of individuals. First and foremost, I must thank my advisor, Dr. Alan Whittington, for his support, guidance, and patience through the entirety of my Masters, particularly in times of lab malfunctions/crises. Second, thank you to Dr. Carol Wicks and Dr. Steve Lombardo for participating on my thesis committee. Your comments were greatly appreciated and enhanced the final result of my research. The field work in Guatemala was a joint effort and required collaboration with INSIVUMEH and funding from the National Science Foundation to make the trip possible. So thank you to NSF and INSIVUMEH. I must also acknowledge Oto Matias, and Julio Cornejo for navigating us through the jungle and guiding us around Santiaguito (and getting us out again). Next, I must thank my friends and officemates (especially Angie) for putting up with me (and my music) for the past two years. I must deeply thank my family for the encouragement (in particular my mom), listening endlessly as I went on about my research, helping in lab (thanks Bec!), and creating as many rock puns as possible (good work Jen). And finally, to Brady Hardiman, a warm thank you for keeping me company as I polished a seemingly endless number of samples (and even polishing a few yourself) and for taking care of the little things.

TABLE OF CONTENTS

LIST OF FIGURES

LIST OF TABLES

EFFECT OF PLAGIOCLASE CRYSTALLIZATION ON LIQUID AND MAGMA VISCOSITY IN THE ANORTHITE-DIOPSIDE-FORSTERITE-QUARTZ SYSTEM

Jackie Getson

Dr. Alan Whittington, Thesis Advisor

ABSTRACT

In order to compare the chemical effect of changing composition on residual liquid viscosity to the physical effect of entrained crystals, seventeen CaO-MgO-Al_2O_3-SiO_2 (CMAS) glasses were synthesized as analogs for dacitic and basaltic lavas. Liquid viscosities were measured between 10^1 and 10^{13} Pa s, over the temperature range of approximately 1600 to 700˚C, using concentric cylinder and parallel plate viscometry. Phase diagrams combined with calculations of the crystal fraction during cooling were used to calculate the viscosity of the magma as a function of temperature.

The results demonstrate that magma viscosities increase during cooling and crystallization as expected. However, in basaltic systems the residual liquid viscosities change little during cooling, due to removal of the anorthite component and the depolymerization of the melt with progressive crystallization. Changing liquid composition counteracts decreasing temperature and increasing crystal content, until the physical effect of crystals begins to dominate at crystal fractions greater than about 40%, assuming crystals remain in the magma. In contrast to basalts, liquid and magma viscosity in dacitic systems always increases during cooling. This suggests that the viscosity of cooling basaltic magma chambers may change little over extended temperature intervals.

CHAPTER 1 – INTRODUCTION AND BACKGROUND

". . . its feet founded in ashen ruin, its huge cone rising to a great height, where its reeking head was swathed in cloud. Its fires were now dimmed, and it stood in smoldering slumber, as threatening and dangerous as a sleeping beast."

–J.R.R. Tolkien

1.1 Introduction

Volcanoes are one of the most spectacular and perhaps one of the more elusive geological phenomena. The globe is peppered with volcanoes, most dramatically along the aptly named "Ring of Fire" that surrounds the Pacific Ocean (Figure 1.1). Despite their splendor, volcanoes are also one of the most destructive natural forces. The 1980 explosion of Mt St. Helens shocked the nation with its violence. The eruption caused an enormous blast, avalanches of debris, overpowering ash falls, and fifty-seven deaths (Fisher et al. 1997). Perhaps the most concerning aspect of volcanic eruptions is that there is currently no accurate way to predict how, why, and especially when these destructive eruptions will occur. For vulcanologists, this is a most tantalizing problem.

Volcanology research has been performed at both large scale (plate tectonics) and small scale (magma melt structure). This study's primary investigation is in the small scale in terms of magma rheology with the eventual goal of applying the results to larger scale processes. Magma rheology is defined by Spera (2000) as "the science of deformation and flow of magma." The flow of magma is described by its viscosity. Lava viscosity is an outwardly visible property of lava, which makes it a simple way of characterizing erupted lava. Viscosity has a large effect on both petrological and volcanological processes. One of the primary purposes in petrological research is to determine and understand the factors that create the multitude of different magmatic

rocks. When first introduced to igneous rocks, geologists are taught to identify these rocks based on their composition and textural features. These features can then be interpreted in terms of processes affecting the origin of the magma and its subsequent history, cooling and solidification. Volcanic rocks are quenched relatively rapidly, which presents an insight into plutonic rocks by preserving a freeze frame image of the composition of natural melts (Spera 2000).

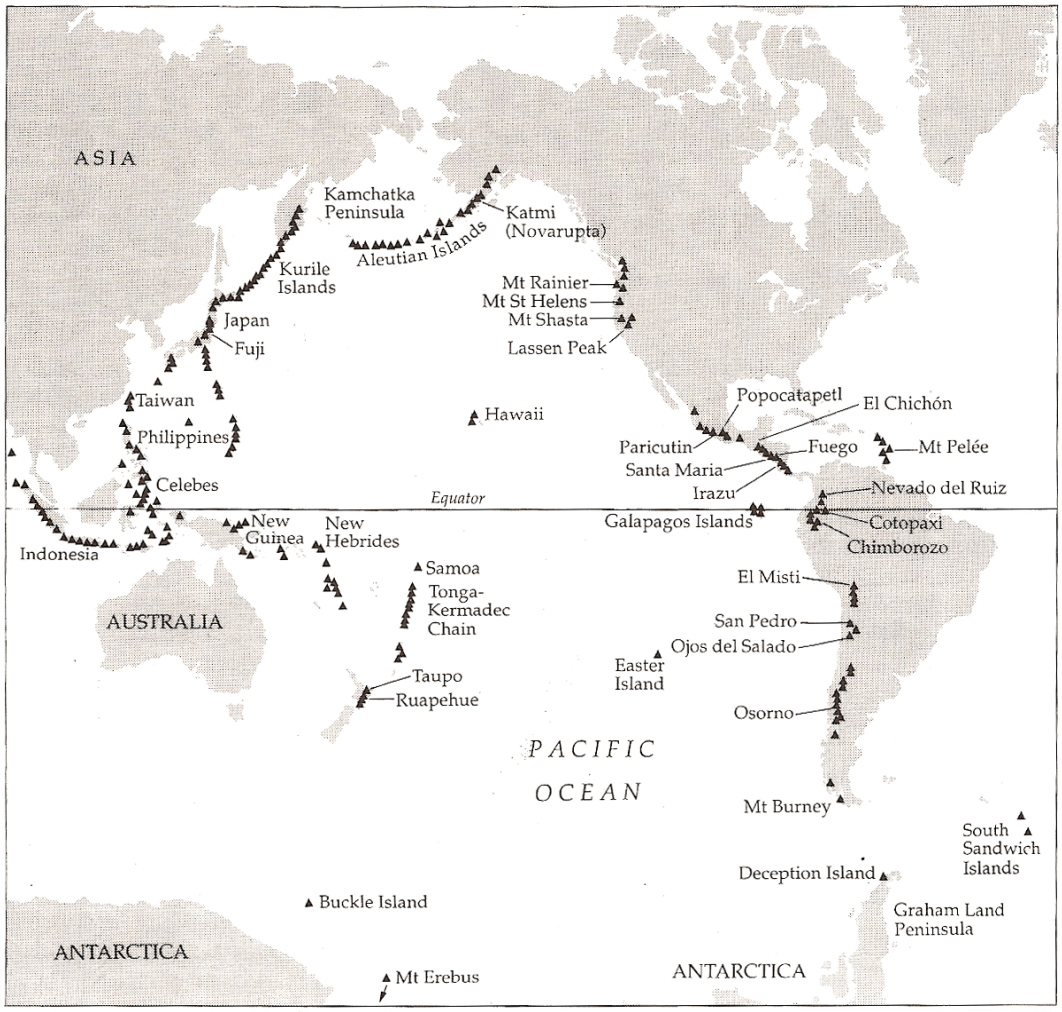

Figure 1.1. Ring of Fire demonstrating abundance of volcanoes (Francis and Oppenheimer 2004).

Specific lava types display different rheological properties based on both internal and external characteristics. External parameters include variables like topography and

effusion rates. Internal characteristics include variations in crystallinity, bubble content, water content, viscosity, and liquid composition to name a few. The most common lava types and the primary focus of this paper are basaltic, andesitic, and dacitic.

Basaltic lava flows typically erupt at temperatures between 1000-1300°C (Spera 2000) and are extremely fluid with flow rates measured as high as 60 kilometers per hour (Francis and Oppenheimer 2004). Basaltic type lava flows can be seen at Hawaii and Iceland. Basalt is composed primary of SiO_2 (40-50 wt %), Al_2O_3, CaO, FeO, and MgO. Compositionally, basalts can be divided into two main groups, alkaline and tholeiitic basalts. Alkaline basalts are enriched in sodium and potassium, are silica undersaturated, and commonly contain phenocrysts of olivine. Tholeiitic basalts are silica saturated to weakly undersaturated, dominated by clinopyroxene and plagioclase and typically have a fine glassy groundmass. Generally, basaltic lava flows have very low viscosities and yield strength and tend to travel large distances. As the lava flows, it begins to cool, causing the surface of the magma to solidify and form a casing around the lava flow. As cooling proceeds, lava blocks begin to accumulate on the solidified surface and solidified lava begins to build up as the lava flow slowly advances.

Andesitic lavas are very similar to basaltic lava flows but the viscosity and yield strength are higher and thus they do not travel as far. Andesitic lavas have a tendency to form block lava flows, which are very steep and results in piles of angular rock piled atop one another. While flow continues, the surface consists of brittle rock and the core is viscous, molten rock (Francis and Oppenheimer 2004).

Dacitic lava is the next step above andesite lavas in viscosity and yield strength. For example, Mt St. Helens in Washington, Santiaguito in Guatemala, and Unzen

Volcano, Japan all have characteristic dacitic lava domes. Dacites move very slowly, which leads to thick, steep extrusions. One cause of this decrease in flow rate is the higher crystal content. Dacitic lavas can exhibit as much as fifty percent crystal content. This high crystallinity causes the lava to move extremely sluggishly, particularly as the lava cools. In rare cases, as seen at Santiaguito, these lavas form steep sided, thick flows, with tall levees with a 30° angle of repose at 17-35 meters tall (Harris et al. 2002). Dacite lavas are so resistant to flow that they typically form lava domes rather than flows. Lava domes are near-symmetrical features with their 'peaks' similar to block lavas. They typically grow incrementally from inside the dome and slowly push the dome outwards. This is known as endogenous growth, as opposed to exogenous growth, where lava domes grow as separate lobes pile atop each other (Francis and Oppenheimer 2004).

Rheology data for natural magmas are scarce and hard to obtain but simple systems are easier to quantify and more commonly found in the literature. As a general rule, the more complicated a melt is, the greater the difficulty to pinpoint how a specific constituent alters the rheology. This study takes an experimental approach to determine the viscosity of crystallizing magma by analyzing CaO-MgO-Al_2O_3- SiO_2 (CMAS) analogs of some common volcanic rocks.

1.2 Viscosity

Viscosity is a description of a liquid's resistance to flow. Viscosity is affected by many factors and consequently can be a useful tool because it is an extremely visible characteristic of lavas. Generally, viscosity is defined as the ratio of an applied stress to the resulting strain rate, $\eta = \frac{\sigma}{\dot{\varepsilon}}$, and conventionally expressed in units of poise (g cm^{-1} s^{-1}) or in Pascal seconds (N m^{-2} s; 10 poise = 1.0 Pa s). Magma viscosity depends on a

multitude of factors; including but not exclusive to composition, melt structure, temperature, pressure, volatile and crystal content (e.g. Dingwell et al. 1993). The magma viscosity is dependent on these factors so it is important to be able to quantify them; however, many of them are interconnected in volcanic settings, so determining how each one individually effects the viscosity can be challenging.

In this study three terms magma, liquid, and glass will be frequently used and their correct definitions must be outlined to avoid confusion. 1) Magma describes the combination of liquid, volatiles, and solids. The main aim of this study is to describe the effect of crystals in a magma. In order to perform this task, measurements were conducted on specific silicate compositions while they were completely molten and glass cylinders were used to measure the viscosity of a supercooled liquid. 2) If a composition is completely molten it is considered to be a liquid where it is entirely fluid. If a liquid is cooled, the viscosity increases with decreasing temperature, and if crystallization does not occur it will form a glass. 3) A glass is an amorphous solid lacking an orderly atomic arrangement (Mysen and Richet 2005; Spera 2000). The shift from a liquid to a glass is described by the glass transition, which occurs over a narrow range in temperature. The glass transition temperature (T_g) is highly variable depending on composition and experimental conditions. For example, the T_g is higher for an experiment using a faster rate of heating or cooling. This variable temperature is due to the fact that T_g is not a thermodynamic phase transition, which can take place at equilibrium, but rather entirely kinetic in origin (Moynihan 1995). T_g is more specifically where the temperature of the tangents to the glass and liquid curves of a given property intersect (Figure 1.2). The

general definition of T_g is where the liquid's atomic configuration is frozen in place during cooling (Mysen and Richet 2005).

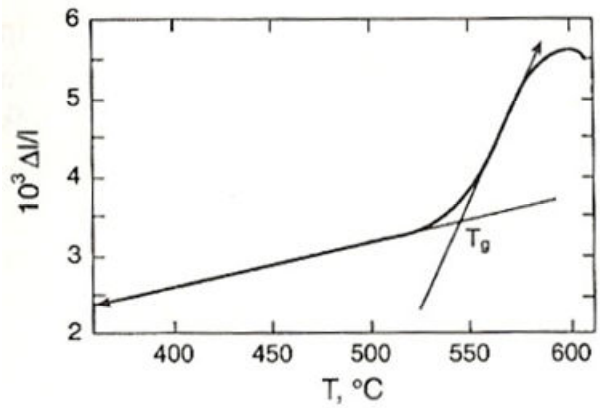

Figure 1.2. Glass transition temperature as determined by the break in the thermal expansion curve of an industrial glass, where *l* is the sample length (Mysen and Richet 2005).

Melt composition has a large effect on viscosity, especially at lower temperatures. As previously mentioned, it is generally known that basaltic magmas are more fluid than dacitic magmas. The basic explanation for this relationship is when there is more silica present in a melt the more viscous it will be; however, for a deeper understanding of the relationship between composition and viscosity the melt structure must be investigated. The primary way melt structure is described is based on the polymerization of the melt. Cations in the melt are divided into network-formers and network modifiers. Network-formers are cations that are in tetrahedral coordination including silicon and aluminum, when aluminum is in tetrahedral coordination it requires charge balancing by alkali metals or alkaline earths (Mysen 1987). A hypothetical melt containing all Si-O and Al-O bonds is considered fully polymerized. Network-modifiers include alkali and alkaline earth cations such as potassium, sodium, calcium, and magnesium. Network-modifiers cause more nonbridging oxygens which results in the melt being depolymerized. NBO/T

describes the ratio of the nonbridging oxygens (NBO) and tetrahedrally (T) coordinated cations. NBO/T can range from 0-4. If a melt has a high NBO/T then it is considered to be depolymerized and consequently has a low viscosity. If a melt has a low NBO/T the melt is polymerized and is viscous.

1.3 Rheological Behavior of Fluids

There are many components that alter magma viscosity and therefore it is prudent to begin with a basic understanding of how simple fluids behave and build up to a discussion of more complicated magmas.

Newtonian flow describes a fluid that has a linear relationship between shear stress and strain rate. Viscosity is defined as the ratio of shear stress divided by strain rate i.e. Newtonian viscosity is independent of stress or strain rate (Figure 1.3).

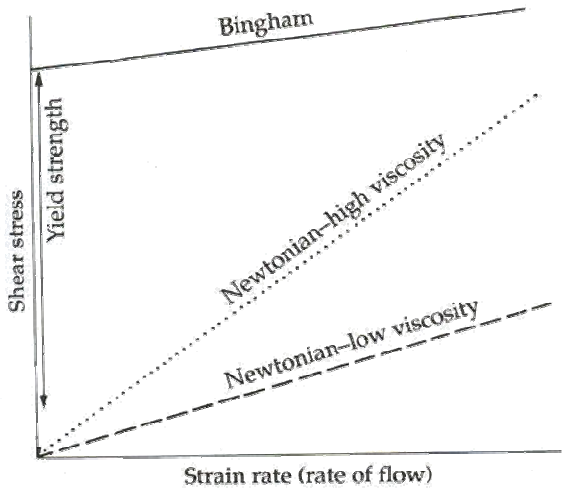

Figure 1.3. Description of different flow behavior (Francis and Oppenheimer 2004).

Most lavas, however, do not behave in a Newtonian fashion due to a number of factors, particularly crystallinity. Non-Newtonian flow occurs in fluids that do not have a linear relationship between stress and strain rate. This type of flow pertains to many lava flows

but not all. More complex fluids are more likely to behave like a Bingham body that possesses a yield strength that must be exceeded before it will flow. Silicate liquids exhibit Newtonian behavior under the stress-strain conditions of lava flows but for magmas with a significant crystal content this simple relationship is not accurate.

The temperature dependence of viscosity can be described in many ways. Basaltic lavas extrude at higher temperatures than other lava types which makes them very fluid in comparison. This temperature difference could possible be more important then the low silica content. One of the simplest and most commonly used viscosity-temperature relationships is the Arrhenius law (Equation 1.1).

$$\eta = A_\eta \exp E_\eta / RT \qquad (1.1)$$

The Arrhenius law is also commonly expressed as $\log\eta = A_\eta + E_\eta / T$, where A_η is a constant, E_η represents the activation energy of viscous flow, and R is the universal gas constant. The activation energy is related to the ratio of molar (Si+Al)/O for a melt (McBirney and Murase 1984; Spera 2000). Bottinga and Weill (1972) presented a model for viscosity based on the Arrhenian relationship between temperature and viscosity. This model works well at superliquidus temperatures but extrapolation of Arrhenian behavior is not applicable to lower temperatures or viscosities greater than 10^5 Pa s that are outside of their experimental range.

The Arrhenian equation depends heavily on an atom being capable of exceeding the energy barrier or E_η constant in order for the liquid to flow. The Adam and Gibbs (1965) theory states that flow occurs due to the availability of configurational sites. The basic premise behind this relationship between flow and configuration is that a rearrangement of the configuration of a liquid's structure is required in order to have

viscous flow. For example, when configurational entropy increases with increasing temperature the rearrangement can occur in a smaller and smaller volume and therefore the liquid becomes more fluid. Richet (1984) applied the Adam and Gibbs (1965) theory of configurational entropy to derive an expression for viscosity (Equation 1.2).

$$\log \eta = A_e + \frac{B_e}{TS^{conf}} \qquad (1.2)$$

A_e is a constant, B_e is a constant independent of temperature but dependent on composition and represents the Gibbs free energy preventing structural rearrangement in a melt (Neuville and Richet 1992). This theory is beneficial because it takes into account viscosity's dependence on temperature and composition. The S^{conf} is the configurational entropy of the melt which depends on the temperature, isobaric heat capacity, C_p, and the entropy of the glass at its glass transition temperature. Configurational entropy is dependent on temperature therefore it can be calculated based on the following equation (Equation 1.3).

$$S^{conf}(T) = S^{conf}(T_g) + \int_{T_g}^{T} \frac{C_p^{conf} dT}{T} \qquad (1.3)$$

where C_p^{conf} is the configurational heat capacity, which is the difference between the heat capacity of the liquid (C_{pl}) and the heat capacity of the glass at T_g (C_{pg}).

$$C_p^{conf} = C_{pl} - C_{pg}(T_g) \qquad (1.4)$$

The theory of configurational entropy has been demonstrated to reproduce viscosity data very well where independent means can be used to determine the configurational entropy of the glass at T_g (Richet 1984). The drawback to the Adam and Gibbs theory is that in order to calculate the configurational entropy, the heat capacity must be known; however, there is a limited amount of heat capacity data for silicate melts.

Since very little data are available to calculate the S^{conf} of silicate melts, another method for interpolation is required. A very common method of viscosity interpolation uses the Tammann-Vogel-Fulcher or TVF equation (Equation 1.5) (Tammann 1926, Vogel 1921, and Fulcher 1925). Although it has a very similar format to the Adam and Gibbs theory, the TVF equation is an empirical method of prediction:

$$\log \eta = A + \frac{B}{T - C} \qquad (1.5)$$

where A, B, and C (in some literature referred to as T_1) are constants. A has been found to be independent of composition and represents the value of log viscosity (Pa s) at infinite temperature. B is proportional to the activation energy, which corresponds to the potential energy barriers hindering the rearrangement of the melt to allow viscous flow, and C is a temperature (K) at which viscosity would be infinite (Russell and Giordano 2005). The parameterization of this non-Arrhenian method has been used in multiple studies including this one to predict viscosities of multicomponent silicate melts, to be discussed further in later chapters.

The above viscosity calculation models apply to homogeneous liquids (in simple systems). These models are not capable of predicting the viscosity for magmas with entrained crystals. Now it is necessary to investigate the effect of crystals on magma viscosity.

1.4 Effect of Crystals

Crystals can affect the evolution of igneous rocks in many ways. Crystal growth controls mineral textures and affects crystal size distribution and chemical zoning. One of the basic principles taught in any introductory geology is that crystals increase the overall viscosity of the magma. A major goal for this study is to dissect this generality in

order to quantify the precise effect entrained crystals will have on the viscosity of a lava. Ryerson et al. (1988) argues that the magma as a whole will behave as a non-Newtonian liquid but the liquid minus the crystals will still act as a Newtonian fluid. It is imperative to understand the effect of crystals on lavas because most are extruded at temperatures below their liquidii and therefore crystallization takes place. Marsh (1981) remarks that most lavas once cooled contain 25-55 volume percent crystals.

The Einstein-Roscoe equation calculates the viscosity as it varies with volume fraction of crystals:

$$\eta = \eta_0 (1 - R\phi)^{-2.5} \qquad (1.6)$$

where η_0 is the viscosity of the liquid, and R is a constant that represents the volumetric ratio of solids at maximum packing; 1.67 is found to be the most accurate for lavas (Marsh 1981) and is used in this study. The symbol φ represents the actual volume fraction of solids in suspension (McBirney and Murase 1984). The Einstein-Roscoe equation is the primary method used to determine viscosity of a melt with crystals present. Unfortunately, there are multiple drawbacks associated with using this method of viscosity prediction. One of the problems and a primary concern of this study is that the equation does not take into account the chemical change of the liquid composition due to the onset of crystal growth. Despite this inability, however, it still remains the best method to calculate the effect of crystals on magma viscosity.

Crystals can have a substantial effect on the overall magma viscosity. An experimental study performed by Lejeune and Richet (1995) found that at 40 volume percent crystals the viscosity was substantially greater than at smaller volume fractions. They applied an experimental approach by measuring the viscosity of melt-crystal mix as

a function of temperature at constant crystal fraction. Their composition consisted of partially crystallized aluminous enstatite in order to examine the effect of increasing crystal fraction. Aluminous enstatite crystals have a low rate of nucleation and crystal growth. Below is a graphical representation of their results (Figure 1.4).

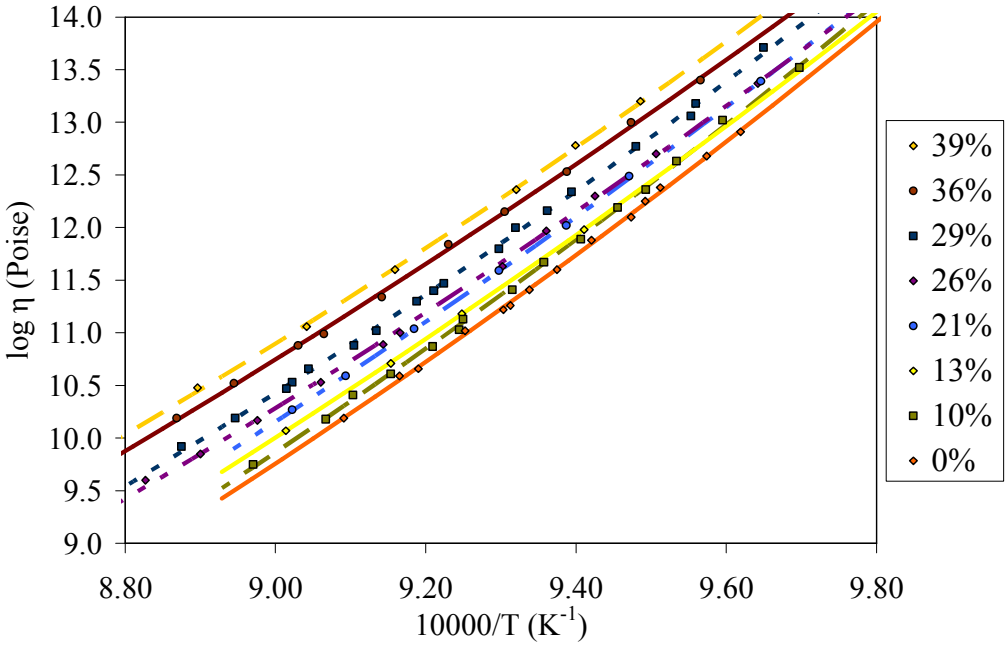

Figure 1.4. Viscosity of aluminous enstatite at varying crystal volume fraction as a function of temperature plotted with their TVF equations (Lejeune and Richet 1995).

From the data it is clear that as crystal fraction increases so does the viscosity of the "magma". Samples were also prepared to measure above 40 volume percent crystals; however, these samples demonstrated a drastic increase in viscosity that prevented good measurements from being collected. One important feature of this study, however, is that the crystals and the melt are of the same composition. The composition of the melt never changes and therefore is not an accurate description of what occurs in real lavas during partial crystallization.

Bouhifd et al. (2005) investigated the difference between the chemical effects, the change in liquid composition during crystallization, and the physical effects of a partially crystallized alkali basalt melt with different redox states. Synthetic glasses were produced analogous to the real alkali basalt and were comprised of eight components, SiO_2, Al_2O_3, Na_2O, K_2O, FeO, MgO, CaO, and TiO_2. The viscosities of both the natural and the synthetic liquids were determined at high and low temperatures. The results are best described in the following figure (Figure 1.5).

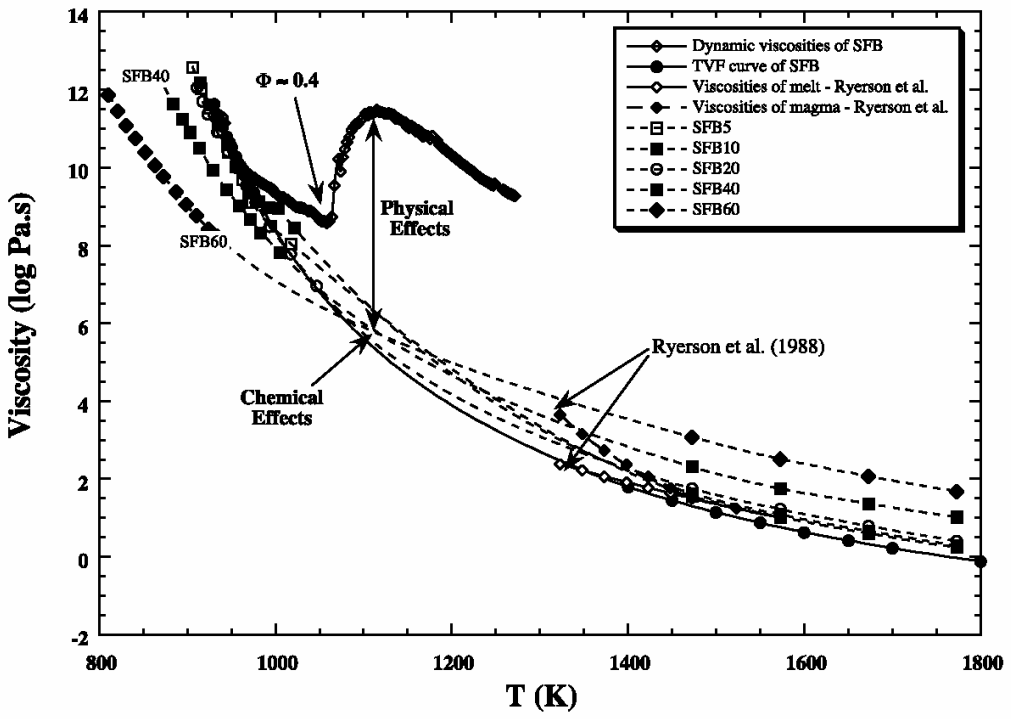

Figure 1.5. Physical and chemical effects of entrained crystals (Bouhifd et al. 2005)

The above diagram demonstrates the large change in viscosity of the basalt as the crystal volume fraction exceeds 40%, as found by Lejeune and Richet (1995), and also demonstrates how viscosity changes with composition of the synthetic glass produced to demonstrate the compositions after different stages of crystallization (samples SFB5-60).

These data show a remarkable difference in the viscosity of the melt versus the viscosity of the magma.

The purpose of this research is to study synthetic systems where phase equilibria are well understood but little viscosity data are available, examine the chemical effect of crystallization on liquid and magma viscosity, and demonstrate the importance of the results for physical models of igneous processes such as crystal settling, magma ascent and eruption dynamics. This study's principal objective is to examine the effect of crystals on magma viscosity during crystallization. In other words, the magma can be altered in two primary ways: chemically and physically. The physical change of a magma is caused by the presence of solids within a fluid. The chemical property examined is the changing liquid composition as a function of plagioclase crystallization.

1.5 The Importance of Plagioclase

This study investigates the change of melt viscosity as plagioclase progressively crystallizes by analyzing the liquid lines of descent for three separate series of melts when anorthite is the liquidus phase. Looking beyond the realm of experimentally produced glasses, many examples can be found to demonstrate the importance of plagioclase crystallization in real magmas.

The three series of synthetic glasses produced for this study are based on three common igneous rock types; tholeitiic basalts, basaltic andesites, and dacites. Tholeiitic basalts are the most common extrusive rock types on Earth, including at mid-ocean ridges and ocean islands. Sometimes they occur as lava lake, formed when lava erupts from a fissure or conduit and fills into an older crater creating a pond of lava. For example, in 1965 an eruption created a pond of lava 84 m deep and 800 m wide in the Makaopuhi

crater at Kilauea volcano on Hawaii (Wright and Okamura 1977). Below are pictures from two Kilauea lava lakes, Manuna Ulu and Aloi Pit crater, respectively (Figure 1.6).

Figure 1.6. Mauna Ulu lava lake with a 10 m high lava fountain (a). Aloi Pit Crater with walls that are 15 meters high (b) (Schmincke 2004).

As described by Kirkpatrick (1977), "The Hawaiian lava lakes offer an unparalleled opportunity to study the processes that occur during crystallization of basaltic magma."

Primarily the studies performed on the Kilauea lava lakes are concerned with the physical and chemical processes that occur during cooling. Wright and Okamura (1977) investigated the cooling and crystallization of the Makaopuhi lava lake. Kirkpatrick (1977) investigated the nucleation and growth of plagioclase in the Makaopuhi and Alae lava lakes by analyzing thin sections from drill-cores taken at different depths at one time. The major crystals found were plagioclase, olivine, and pyroxene. Below, is a thin section demonstrating the abundance of plagioclase within the basaltic magma (Figure 1.7).

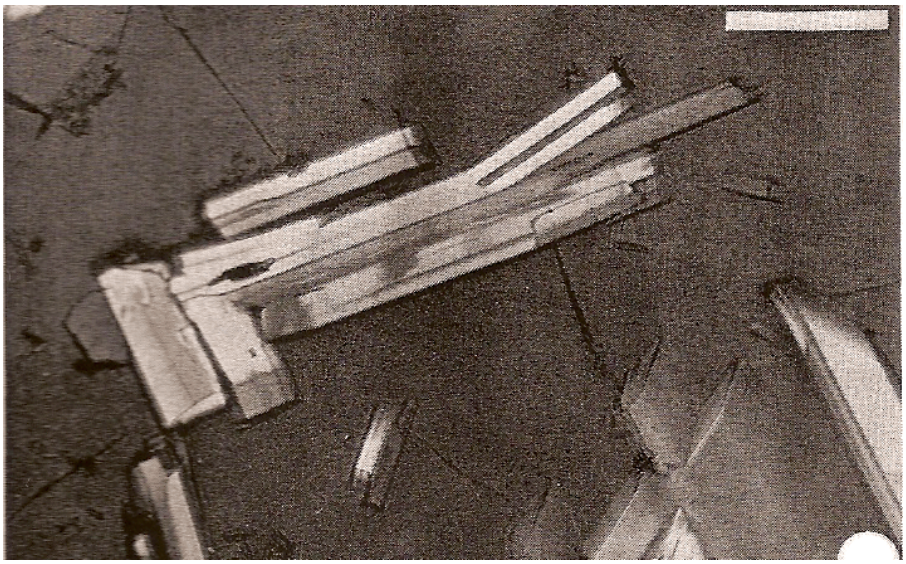

Figure 1.7. Plagioclase nucleating on plagioclase in partially crossed polarizers. (0.1 mm scale bar) (Kirkpatrick 1977).

An outstanding example of basaltic andesites and dacitic lava can be found in Guatemala at Santiaguito Lava Dome. Santiaguito and its neighboring volcanoes are the result of arc volcanism caused by the subduction of the Cocos plate under the Caribbean plate (Figure 1.8). The Santa Maria composite cone, a precursor to Santiaguito, began growing 20,000 years ago. Today, Santa Maria stands 12,375 feet in tropical Guatemala. Santiaguito lies in a crater resulting from the explosion of Santa Maria in 1902 (Harris et

al., 2002). This eruption caused the death of 6,000 people when the southwest side of Santa Maria released 8.5 km^3 of dacitic material and a small amount of basaltic andesite material, leaving a 20 km^3 crater, which would eventually become the site of Santiaguito (Harris et al., 2001).

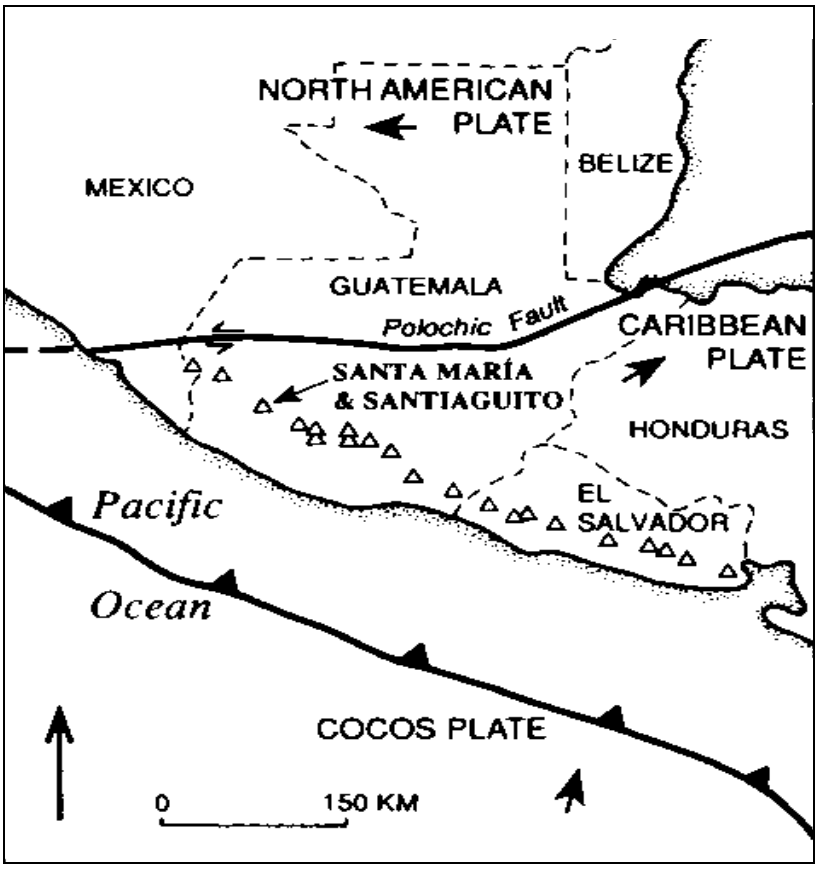

Figure 1.8. Tectonic setting of Santa Maria and Santiaguito (Conway et al. 1994)

In the aftermath of the explosion in 1902, two decades passed with little or weak activity, i.e. weak ash emission and geyser activity. Since 1922, activity increased with continuous slow moving dacitic lava pouring from the center of the crater, which over time built up to be the Santiaguito lava dome complex of today (Figure 1.9).

Figure 1.9. Santa Maria and Santiaguito Lava dome complex (March 2005).

Four vents contributed to the growth of Santiaguito, the Caliente Vent being the dominant provider in more recent years. In the years between 1922 and 1984, Santiaguito was observed to have a cyclic pattern of a three-five year period of high extrusion rate (0.6-2.1 m^3/s) coupled with a ten-twelve year period of lower extrusion rates (0.2 m^3/s) (Harris et al., 2001). In this sixty-two year period the average extrusion rate was 0.46 m^3/s (Harris et al., 2001). Santiaguito is theorized to be a plug volcano, which promotes continual build up and release at regular intervals, consistent with the regularity of the system. In the years following 1984, dacitic extrusions in the form of block lava flows have dominated the system as well as regular ash emissions and continual rock falls that average one fall per minute. The ash emissions are typically about one kilometer high or less, and average about two per hour. However, it is noted

that the length of the periods of low extrusion rates have been increasing, which could suggest that the present activity might cease in the coming decades possibly due to the depressurization and depletion of the source (Bluth and Rose 2004). The data might also suggest that the volcanic activity is changing and becoming less cyclic and instead having a steady extrusion of 0.2-0.4 m^3/s suggesting a more stable constant supply of magma (Harris et al., 2001). Conversely, there is also a steady slight decrease in SiO_2 content of erupted material, which could correlate with a depleted magma chamber (Harris and Rowland 2001; Harris et al. 2002).

Santiaguito is comprised of dacitic lava that contains about 35% phenocrysts (Bluth and Rose 2004). This study examines the path of liquid descent as plagioclase crystallizes. Samples from Santa Maria and Santiaguito were collected and thin sections were produced. From thin section analysis plagioclase is clearly abundant both as a phenocryst and in the groundmass. The figure below demonstrates the abundance of plagioclase in these lavas (Figure 1.10).

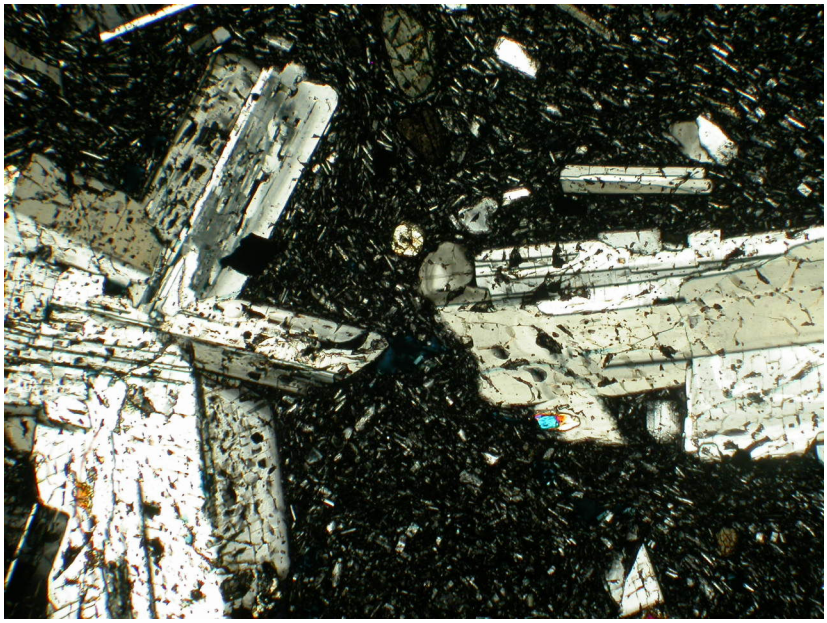

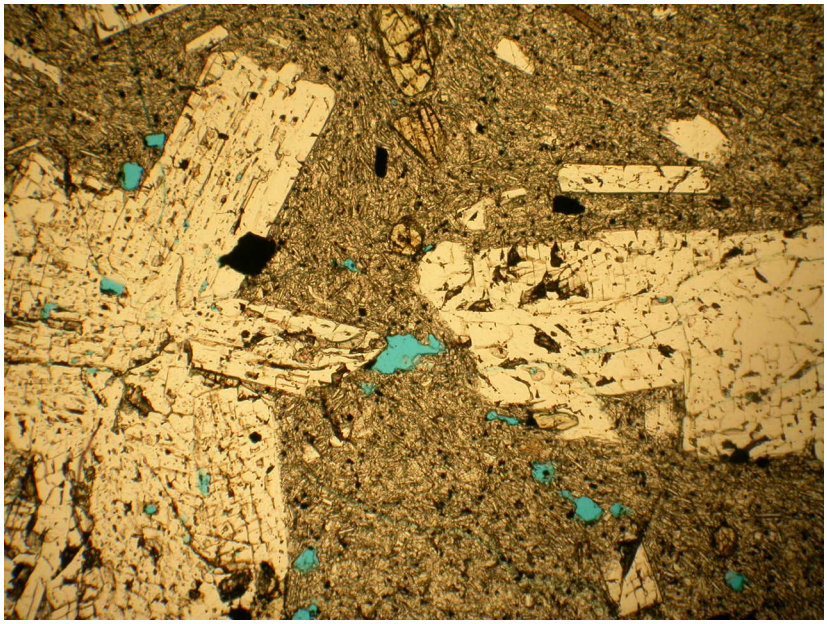

Figure 1.10. Thin section from Santiaguito in (a) cross polarized (b) and plane polarized (4x, field of view is 2 mm).

Overall, Santiaguito presents a site of active dacitic volcanism in a relatively safe collecting environment. The presence of the looming Santa Maria volcano allows access for observation from above the active volcanic activity, an uncommon occurrence. The predictability of the volcano permits and encourages active study. This study will result in improved understanding of the rheology of the block lava flows prevalent in the area, which are extremely hazardous to the local people. The results of this study can be applied to other dacitic volcanoes, including those in populated regions such as Mount St. Helens.

The following work utilizes an experimental approach in order to enhance the understanding of the difference between the physical effects of entrained crystals and the chemical effects of the changing melt composition by analyzing the liquid evolution of three series with the overall goal of applying the results to natural magmas.

In the subsequent chapters the methods, results, and applications to petrological processes are discussed. In Chapter 2 the methods to produce and measure the viscosities of synthetic glasses are described. Chapter 3 discusses the results from the viscosity measurements, TVF modeling of viscosity as a function of temperature and composition, and evolution of liquidus viscosity along liquid lines of descent. Chapter 4 compares the viscosity measurements to previous viscosity prediction models, and reports the calculated magma viscosity of the synthetic liquids, and finally the implications of these calculations on larger geological processes are discussed.

1.6 Summary

- An experimental approach is applied in order to study the difference between the physical effect of entrained crystals and the chemical effect of the changing melt composition with the overall goal of applying the results to real magmas.
- Viscosity is a measure of a fluid's resistance to flow and is defined as stress/strain rate.
- Viscosity decreases with increasing temperature. Several viscosity-temperature relations have been proposed; including the Arrhenian, Adam and Gibbs, and the TVF equation.
- The best method to calculate the effect of crystals on magma viscosity is the Einstein-Roscoe equation.
- The presence of entrained crystals increases magma viscosity, at 40 volume % crystals the viscosity increases drastically.

- This study analyzes the effect of changing the liquid lines of descent as plagioclase crystallizes and the residual liquid composition changes. Hawaiian lava lake basalts and Santiaguito dacites in Guatemala provide excellent examples where plagioclase crystallization is evident.

CHAPTER 2 – METHODS

"A thinker sees his own actions as experiments and questions--as attempts to find out something. Success and failure are for him answers above all."

–Friedrich Nietzsche

2.1 Overview

To better understand how entrained crystals and the corresponding change in melt composition alter the overall viscosity of magma, this study applies an experimental approach. A series of viscosity measurements were collected on seventeen simplified glasses in the CaO-MgO-Al_2O_3-SiO_2 (CMAS) system, with compositions analogous to dacitic and basaltic lavas. The measurements were carried out using two different methods: parallel plate viscometry and concentric cylinder viscometry. Parallel plate viscometry can analyze cylindrical glass cores in the range of 10^9-10^{13} Pa s. Concentric cylinder viscometry measures the sample at superliquidus temperatures in the range of 10-10^5 Pa s. Below, the basic methodology for creating these glasses and how their viscosities were measured are described in greater detail.

2.2 Composition selection

In volcanic research, there are gaps in the data collected in the ongoing task of creating a comprehensive model to describe the viscosity of lava. One tool used in understanding the viscosity of the complicated and often dangerous geology is the producing and measuring of synthetic glasses. The compositions for this study were selected for two primary reasons. First, the systems in which these compositions lie have very limited viscosity databases. Thus, this study serves a necessary function of increasing the understanding of these simple systems. Second, the systems are simplified analogs of more complicated lavas; therefore, allowing for comparison to real volcanic

rocks. The selected compositions are based on basaltic lavas typically found in association with Hawaiian-type volcanism, and lavas derived from the Santiaguito dome complex and Santa Maria stratovolcano in Guatemala, whose rocks are very similar to those found at Mount St. Helens.

In total, seventeen synthetic glasses were produced. Eight were synthesized analogous to tholeiitic basalts. Nine were synthesized based on the composition of the lavas found at Santiaguito lava dome. Silicic lava flows at Santiaguito contains that produces about 35 volume % phenocrysts, predominantly plagioclase. Cross-Iddings-Pirsson-Washington (CIPW) norms were performed on XRF whole-rock data provided by Bill Rose of Michigan Tech for samples from Santiaguito and Santa Maria (Cross et al. 1902). CIPW norm calculations generate normative mineralogy based on the typical minerals that would be expected to crystallize from an anhydrous melt composition. The normative mineralogy is dominated by the minerals quartz, plagioclase, orthoclase, hypersthene, and diopside. There were also a few samples from Santa Maria data that contained minor normative olivine. For glass synthesis, the iron content in hypersthene has been assimilated into the magnesium, calcium and aluminum content to also avoid problems of Fe^{2+}/Fe^{3+} ratio. The network modifier Fe^{2+} is transferred to calcium and magnesium in such a way as to preserve the bulk structure of the liquid and the overall Ca/Mg ratio. This allows for a relatively easy simplification of the lava compositions into the CMAS system.

The normative values for the Santiaguito and Santa Maria complexes were then plotted in the anorthite-forsterite-quartz ternary system (Figure 2.1). The diagrams demonstrate a basic difference between the two complexes, in that the Santiaguito dome

is slightly more silicic in composition than Santa Maria. Both sets of samples are within the anorthite stability field, consistent with the observation of abundant plagioclase feldspar phenocrysts in both suites.

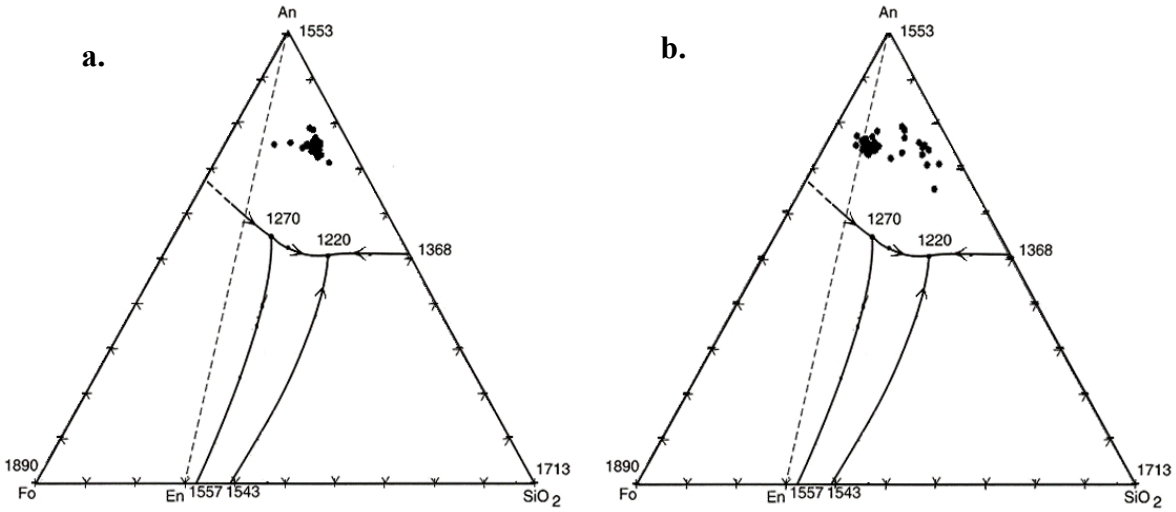

Figure 2.1. Normative compositions of (a) Santiaguito dome complex (n=43), (b) Santa Maria Volcano (n=49). (wt %)

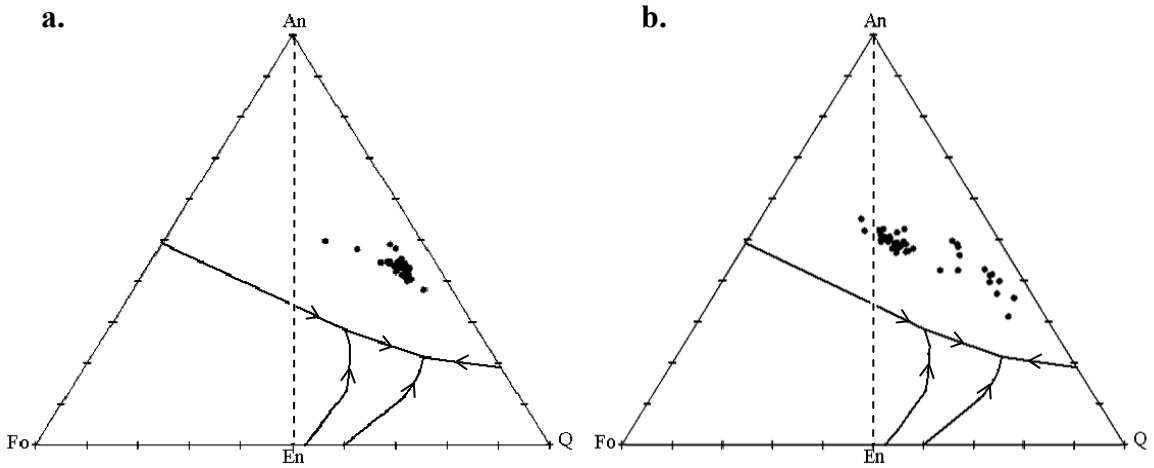

Figure 2.2 a. Santiaguito dome complex. b. Santa Maria Volcano. (mole %)

2.3 Glass preparation

Synthetic glasses were produced by mixing a combination of oxides and carbonate powders. Only four powders are used in the synthesis of these seventeen glasses: SiO_2, Al_2O_3, MgO, $CaCO_3$. The weight percent of the constituent oxides was calculated from the normative mineralogy, and then the weight of added $CaCO_3$ was

adjusted in order to account for the amount of carbonate being included. Two batches of about 70 grams each were weighed with precision of better than 0.2 wt % for each oxide. Once the powders were weighed they were mixed with acetone using an alumina tray, to prevent any contamination, in a shatter box for three minutes. The powder was then placed in a platinum crucible and was decarbonated by slowly step-heating to 1030°C (Table 2.1) in a Thermolyne high temperature furnace (model number 46200).

Table 2.1. Decarbonation program.

Segment #	Type	Starting T (°C)	Final T (°C)	Duration (min)	Rate (°C/min)
1	ramp	0	300	30	10.0
2	dwell	300	300	10	0.0
3	ramp	300	700	20	20.0
4	dwell	700	700	15	0.0
5	ramp	700	950	500	0.5
6	dwell	950	950	180	0.0
7	ramp	950	1050	50	2.0
8	hold	1050	1050		
			Total time:	805	

The sample was removed and weighed to check that all of the CO_2 has been removed from the sample. The sample was then replaced back in the furnace at 1600°C to melt the powder. The sample remained in the furnace for at least an hour before being removed and air-quenched to produce a glass. This glass was then crushed, reground in the shatterbox, and placed back in the furnace at 1600°C. This melting, pouring, crushing, and mixing procedure was repeated 3 times to ensure a homogeneous glass. After the final melting the sample was poured into a graphite crucible to cool slowly and prevent shattering, forming a solid ~60-70 g plug of glass approximately 6.5 cm long that tapers from 3 cm to 2.5 cm wide. The compositions were verified using electron microprobe analysis using a JEOL 733 Superprobe at Washington University, St. Louis, Missouri. The density of each glass was measured, using Archimedes' principle in conjunction with the Mettler Toledo density determination kit and using distilled water as the immersion

liquid. Archimedes' Principle states that every solid mass immersed in a fluid will lose weight by an amount equal to the weight of displaced fluid.

$$\rho = \frac{A}{A-B}(\rho_{H_2O} - \rho_a) + \rho_a \qquad (2.1)$$

where A represents the weight of the sample in the air, B is the weight of the sample in distilled water, ρ_{H_2O} is the density of distilled water (corrected for measurement temperature), and ρ_a is the density of the air. The density of each glass was measured twice on three glass chips per sample. The average precision for these measurements was 0.02 g for all glasses. Following density measurements, the glass was then either annealed to drill cores for the parallel plate viscometer or prepared for the concentric cylinder viscometer.

2.4 Parallel Plate Viscometry

The sample preparation is more intensive for parallel plate viscosity analysis than for concentric cylinder viscometery. Whereas the concentric cylinder requires about 60 grams of glass placed in an alumina crucible the parallel plate requires a cylinder with polished parallel faces. In order to produce these cylinders the glass is first annealed by heating slowly at 3°C per minute to 700°C (close to the glass transition), then slowly cooled at 2°C per minute to room temperature, to prevent breakage while drilling. The glass is drilled using a Starlite diamond core drill bit. This produces cylinders approximately 66 mm diameter, which are cut using a diamond saw to approximately 1 cm in length. These cores are then polished using 240, 600, and finally 800 diamond grit paper to produce a parallel surface. The cylinders are measured using a micrometer to be sure they are parallel, to within 50μm. The length and diameter of the sample are then carefully measured before being placed in the parallel plate viscometer.

The parallel plate viscometer used for this study is the Rheotronic III 1000C Parallel Plate Viscometer, which was purchased from Theta Industries, New York (Figure 2.3). The viscometer can measure over the range 10^9-10^{13} Pa s. The viscometer was reassembled and the instrument calibration was checked using the National Institute of Standards and Technology (NIST) glass standard 717a, a borosilicate. The basic principle of the parallel plate is based on $\eta = \tau / \dot{\gamma}$, where τ is defined as the shear stress and $\dot{\gamma}$ is the strain rate. In this case, the glass is being sheared at a rate determined by the viscosity of the glass between two silica plates (Figure 2.4).

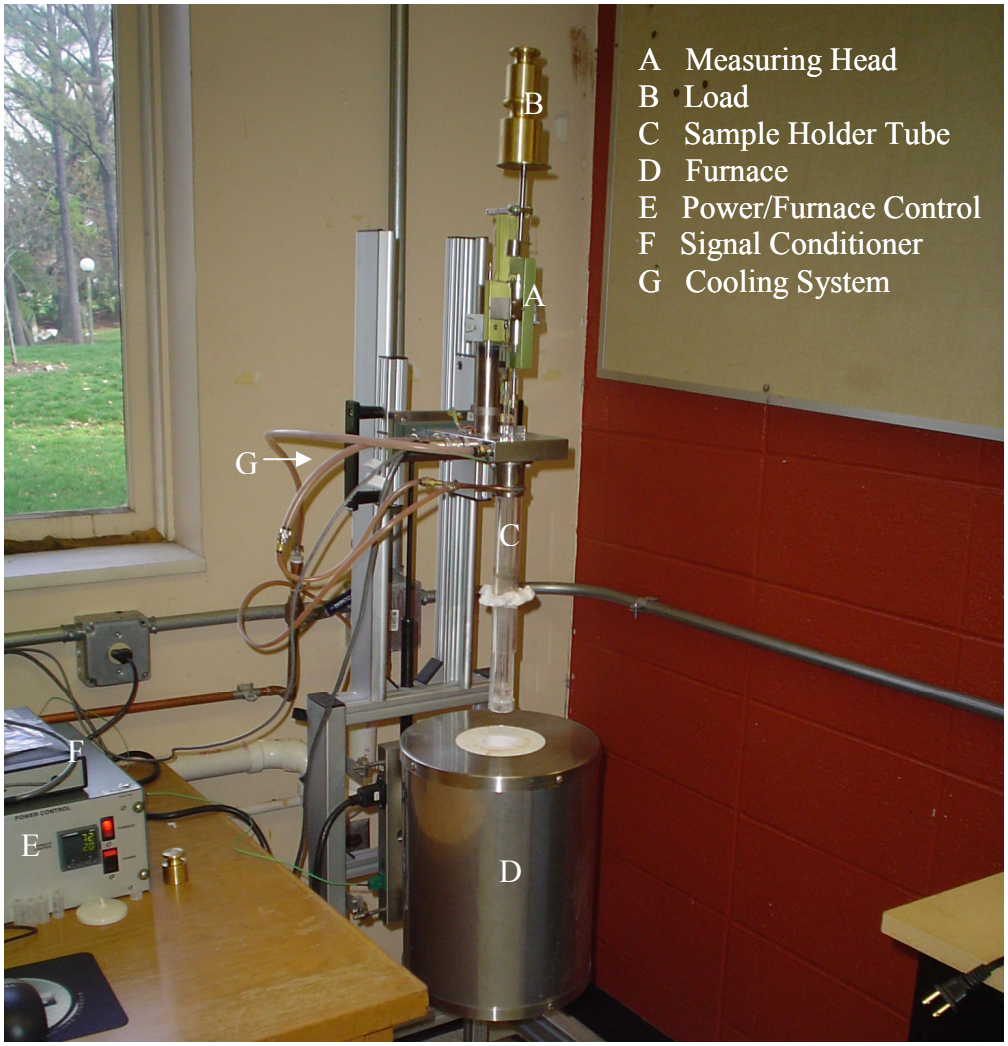

Figure 2.3. Parallel Plate Viscometer.

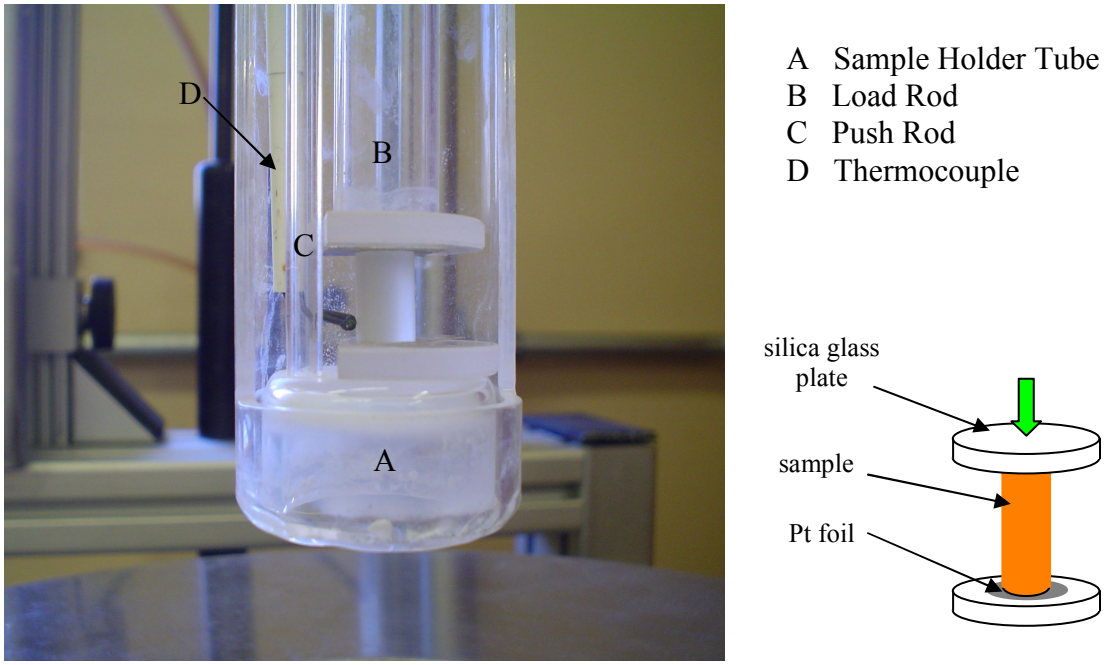

Figure 2.4. Specimen holder geometry.

As seen in the Figure 2.4, the sample sits in a silica sample holder tube and is placed between two pieces of platinum foil and then between two silica plates. To the left of the plates is the push rod that measures the amount of deformation. In the back of the holder tube is a K-type thermocouple. During measurements, the thermocouple is always in contact with the sample to measure as precisely as possible the sample temperature. The load rod exerts a stress upon the sample via the upper plate. The weight of the load rod itself is counterbalanced by weights atop the measuring head (Figure 2.5). Two sets of coils are connected to a linear variable displacement transducer (LVDT). Deformation of the sample results in movement of the top of the load rod relative to the stationary push rod. This relative movement is measured by means of the LVDT. The LVDT then sends the data to the signal conditioner. The signal conditioner transfers the data to the computer which can later be retrieved for analysis.

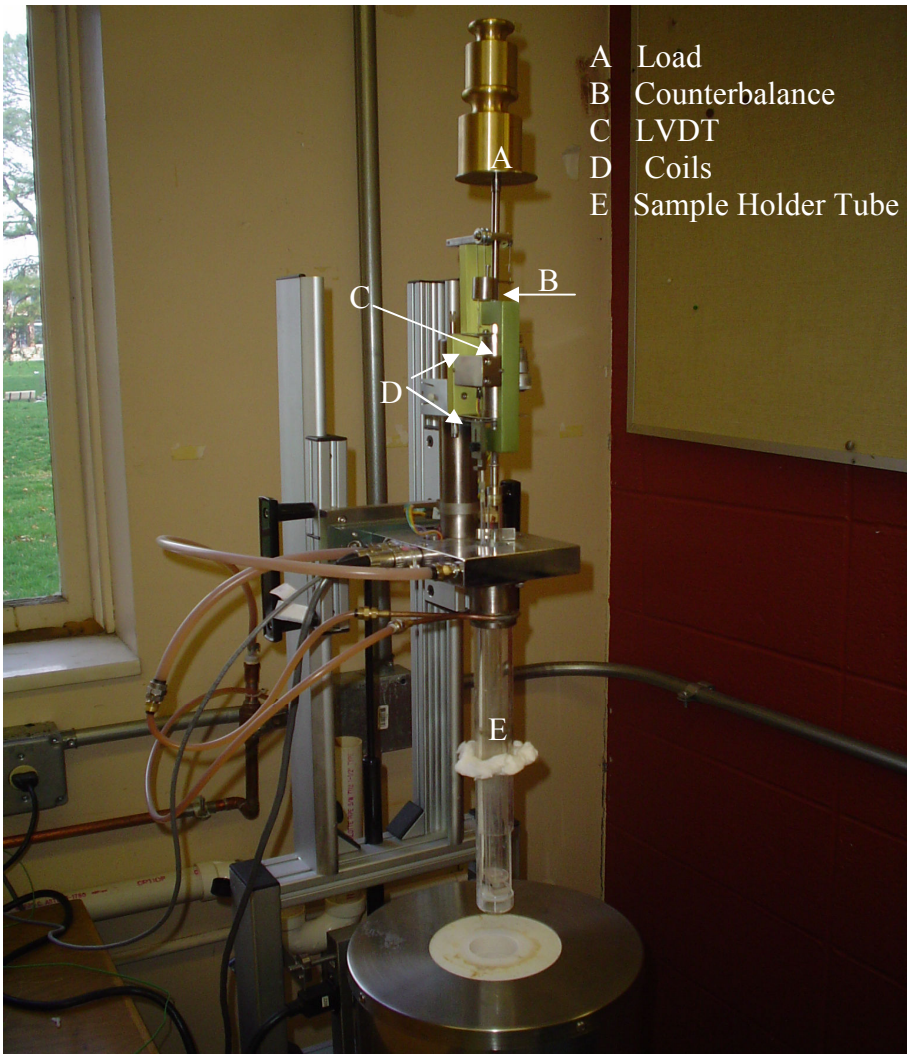

Figure 2.5. Parallel Plate measuring head.

For a typical experimental run, the software requires the starting height and diameter of the sample as well as the load as initial input from the operator. Based on the composition of the sample a temperature program is created to measure the sample viscosity from 10^{9}-10^{13} Pa s. The deformation, temperature, and time of measurement are recorded and the viscosity is calculated by the software typically at 30 second intervals. An independent calculation based on the same sample height data is performed to achieve a more precise viscosity by averaging the deformation over longer time intervals. The independent calculation is always very similar to the computer value but the independent

calculation is performed only on total deformation greater than 5 μm, therefore the calculated viscosity is more precise. However, before any programs were run on unknown viscosity samples the instrument setup was checked for accuracy using the standard glass 717a, borosilicate (Figure 2.6). The viscosity measurements were then compared to the TVF equation from the NIST certificate.

$$\log_{10}(Pa\ s) = -2.5602 + \frac{4852.2}{(T(°C) - 192.462)} \qquad (2.2)$$

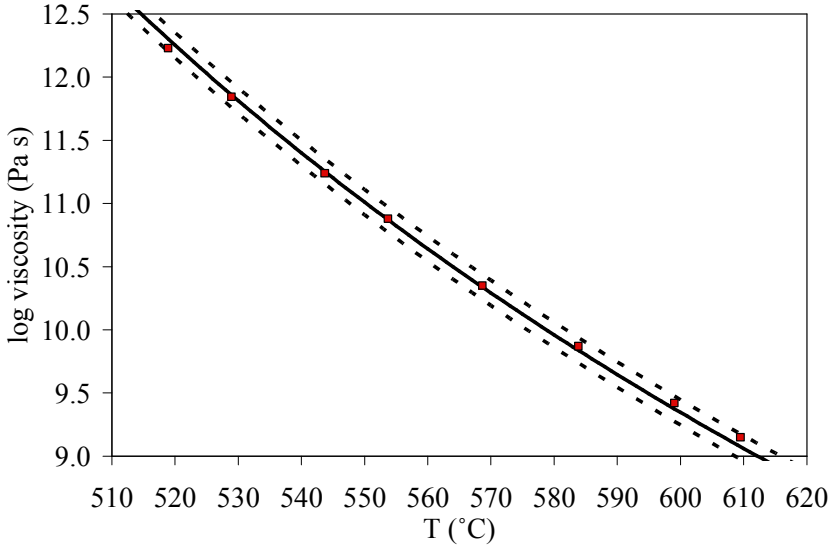

Figure 2.6. Standard 717a Calibration Check. The dotted lines represent ±0.1 log units from the TVF equation. The red squares represent the average of the three runs.

The borosilicate standard was run multiple times in the viscometer as an unknown and compared to the TVF equation developed by NIST. The precision and accuracy were determined by calculating the absolute average deviation between the NIST equation and the three samples analyzed. The precision and accuracy were found to be 0.04 and 0.05 log units, respectively.

On completion of the sample run, the data were analyzed via Excel. To independently calculate the viscosity only three variables were required, time,

temperature, and height. Temperature versus time was plotted to find the specific time interval over which the temperature was stable. Height versus time was plotted to find the precise height change within that time interval. With this information the viscosity can be calculated using the following equation (Equation 2.3).

$$\eta(Pa\ s) = \frac{mgh^2}{3V\,\partial h / \partial t} \qquad (2.3)$$

Where m represents the mass of the load (kg), for all experiments in this study 1500 grams is used for the load, g is gravity (m/s^2), h is is the height of the cylinder (m), and t is time (s) (Dingwell 1995).

2.5 Concentric Cylinder Viscometry

In contrast to the parallel plate, the concentric cylinder measures viscosity at superliquidus conditions, between $10\text{-}10^5$ Pa s for this instrument. In this geometry, the viscosity is measured as the fluid is being sheared between two cylinders. The viscosity is defined by the relationship between the torque and the angular velocity, $\eta \approx \tau/\Omega$.

The viscometer is a Theta Industries Rheotronic II 1600C Rotating Viscometer, using a Brookfield HBDV-III Ultra measuring head (Figure 2.7). The instrument is based on a Searle design where the outside cylinder remains stationary and the inner cylinder rotates. This type of rotating viscometer relies on an inner cylinder, known as a spindle or a rotor, being immersed into a fluid. The spindle is driven by a motor through a calibrated spring within the measuring head. The melted glass exerts viscous drag on the spindle, which is read by the measuring head. The spindle is capable of rotating at different speeds allowing for a range of measurements at different shear rates, up to 250 revolutions per minute.

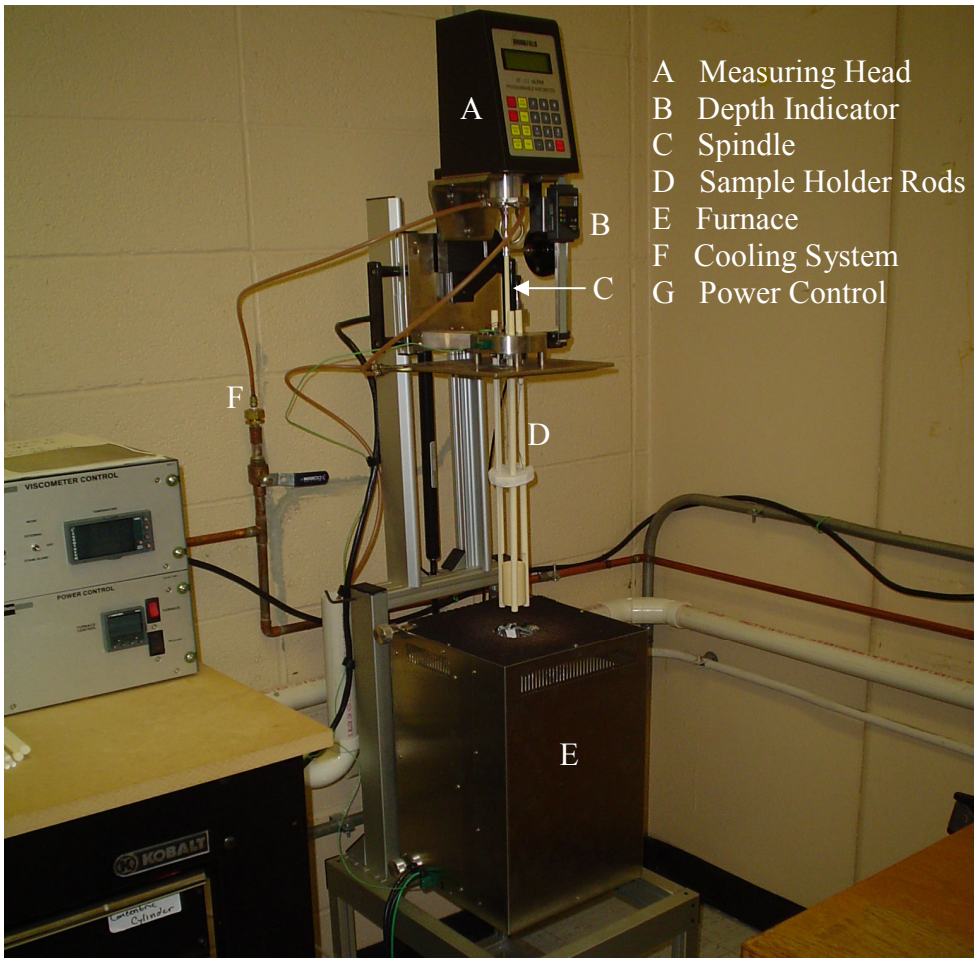

Figure 2.7. Concentric Cylinder Schematic.

A typical experimental run uses approximately 60 grams of sample placed within a 33 mm inside diameter by ~6.5 cm tall alumina crucible. The alumina crucible is centered on three alumina sample holder rods and lowered to a set position within the furnace. The spindle is centered in the middle of the sample crucible just above the sample. The computer controls the furnace, which heats at an operator specified rate to a point above the liquidus, normally in the range of 1550-1600°C. At these temperatures the melt is typically very fluid and the spindle can be lowered into the specimen for measurements to be gathered.

Once the sample has reached its peak temperature the spindle spins at about 10 rpm and is slowly lowered until a torque reading is acquired to ensure the spindle is

always lowered to the same depth within the melt. This initial torque reading is the spindle hitting the top of the melt. The spindle is then lowered into the melt 18 mm as indicated by the depth indicator micrometer situated on the measuring head, that moves in conjunction with the spindle. At this point, the instrument is ready to measure the viscosity of the liquid. Acquiring the same depth for every experiment is important because an empirical means is used to calibrate the viscometer (described below).

The basic theory for concentric cylinder viscometry is $\eta = \tau / \dot{\gamma}$; where is τ stress and $\dot{\gamma}$ is the strain rate. Stress is defined by the amount of torque and the spindle geometry (Equation 2.4). Strain rate is also affected by the geometry of the cylinders as well as the angular velocity (Equation 2.5).

$$\tau = \frac{M}{2\pi R_b^2 L} \qquad (2.4)$$

$$\dot{\gamma} = \left(\frac{2R_c^2}{R_c^2 - R_b^2} \right) \omega \qquad (2.5)$$

M represents the amount of torque, R_b is the radius of the spindle in centimeters, R_c is the radius of the cylinder, and L represents the effective length that accounts for the end effects created by the fact the outside cylinder is not infinite in its dimensions (Figure 2.8). To reduce the effect of the outside crucible's dimensions, during the experiment the bottom of the rotor is kept at least 10 mm from the bottom of the crucible to take measurements. The ω represents the angular velocity of the spindle. The angular velocity can be described by $\omega = \frac{2\pi}{60} N$, where N is the revolutions per minute of the spindle.

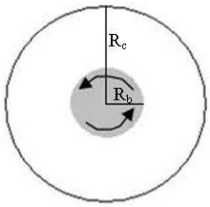

Figure 2.8. Concentric Cylinder spindle crucible geometry, Searle design.

Recall that silicate glasses behave as a Newtonian liquid. A Newtonian liquid is defined as the stress/strain rate ratio having a linear relationship. Each sample run in this study was determined to be Newtonian. This was determined by plotting the stress versus strain rate as the rpm changed and the temperature remained constant (Figure 2.9).

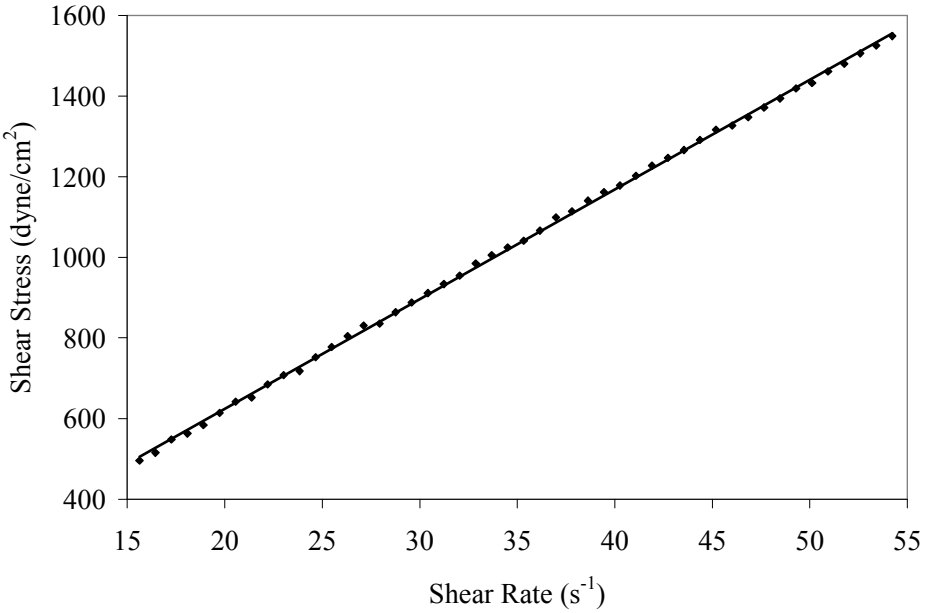

Figure 2.9. Sample SA55 example of Newtonian behavior.

The measuring head is capable of running under two different settings. It can be run manually via the measuring head or it can be run through a computer connection into the measuring head. The system has to be calibrated manually using internal settings of the measuring head. Due to experimental constraints, there were two spindle arrangements that were calibrated to function using the same measuring head. The original Theta design required both a spindle and a rotor (Figure 2.10).

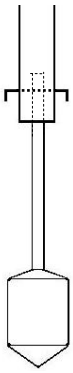

Figure 2.10. Original Theta Inc. setup with coaxial cylinder.

The spindle is a long hollow alumina tube with a small hole approximately 1 cm from the end. The rotor is inserted in the bottom of the spindle and is connected by threading a platinum wire through the aforementioned hole. This design was originally calibrated by Theta using certified standard oil. The machine was shipped, reassembled and the original calibration was tested using standard glasses generated by the National Institute of Standards and Technology (NIST), specifically 717a, borosilicate, and 710a, soda lime silicate. These were compared to their certified TVF equations (Equations 2.6, 2.7).

$$\log_{717_a}(Pa\ s) = -2.5602 + \frac{4852.2}{(T(°C) - 192.462)} \quad \pm 0.1 \qquad (2.6)$$

$$\log_{710_a}(Pa\ s) = -1.729 + \frac{4560}{(T(°C) - 240.8)} \quad \pm 0.1 \qquad (2.7)$$

The certified equations are the result of comparison from many different experiments in several laboratories. The samples were tested at the temperature range of about 1000-1500°C. Through the multiple experiments it was found that viscosity measurements are only accurate after the torque reading stabilizes; the instrument requires ten minutes at a given temperature and speed before the torque stabilizes. Once stabilized, the viscosity reading remains very steady, and approximately five minutes of measurements at thirty second intervals at the stabilized temperature and speed, which are recorded and

averaged for an accurate viscosity. In the following graph, the average data from multiple test runs (Figures 2.11, 2.12) are compared to the TVF equation from the NIST standard reference material certificate.

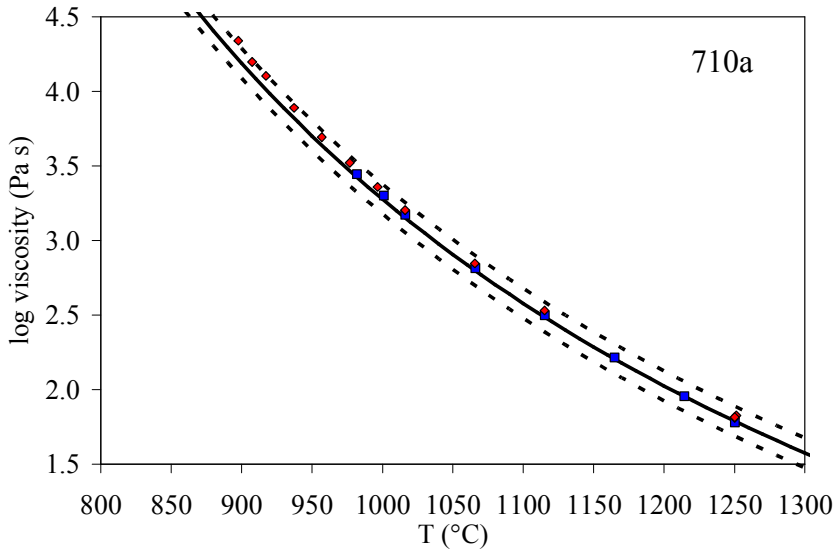

Figure 2.11. Standard 710a Calibration Check. The dotted lines represent ±0.1 log units from the TVF equation. The data points represent data from the two runs.

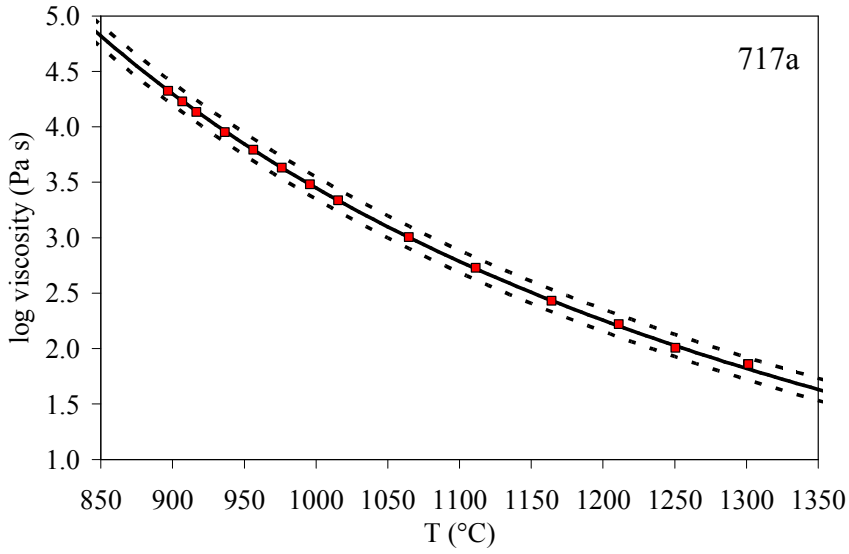

Figure 2.12. NIST standard 717a compared with TVF. The dotted lines represent ±0.1 log units from the TVF equation. The red squares represent the data.

The accuracy and precision was calculated for NIST 710a from two runs (Figure 2.11) and was found to be log 0.05 and 0.02 log units, respectively. Accuracy was calculated

based on how well the viscometer reproduces the NIST certified values; precision was calculated by comparing the data from multiple runs. NIST 717a (Figure 2.12) standard was run only one time and the accuracy was less than 0.005 log units from the TVF equation.

Unfortunately, the original Theta construct had a design weakness that required a modification of the spindle geometry. Due to the high temperatures required for the samples tested in this study, the platinum wire required to hold the rotor in place would become malleable and the viscous drag created by the melt would shear the wire, causing the rotor to be pulled from the spindle and into the sample crucible. In order to reach the desired viscosities, a new spindle design had to be calibrated.

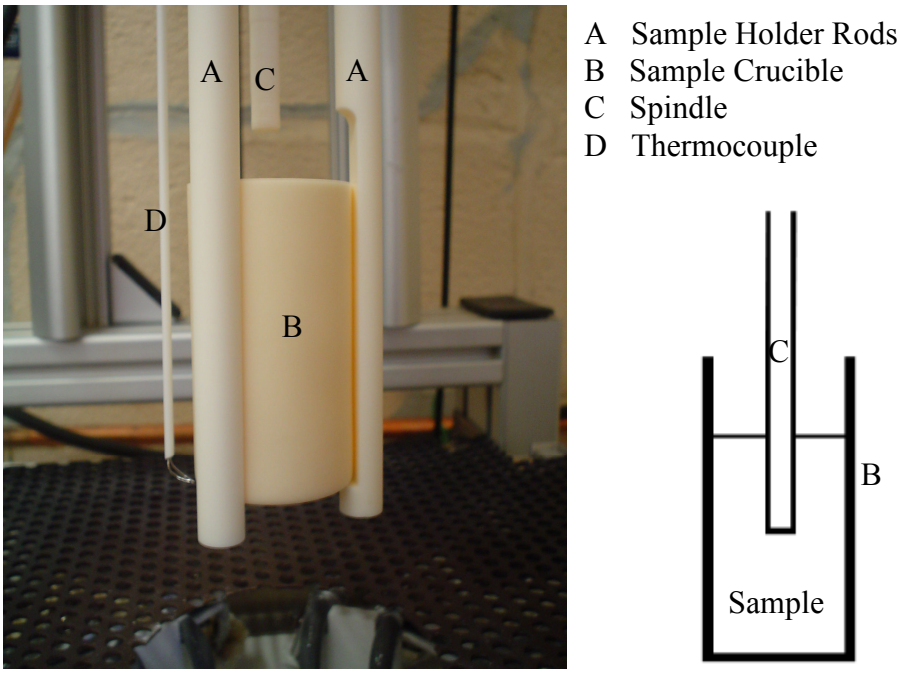

Figure 2.13. Modified spindle geometry.

Using the same methodology as Theta for the original rotor design, the same reference oil was used to calibrate a new spindle geometry. This spindle geometry is a more basic design then the original coaxial rotor assembly. The modified spindle is a solid cylindrical alumina rod of approximately 46 cm in length and 6.25 mm in diameter.

A disadvantage for this modified setup is the small diameter, which makes it more difficult to get adequate torque readings at high T for low viscosity melts (Figure 2.13).

This new spindle geometry required a new calibration for the internal setting of the Brookfield measuring head. This calibration required an adjustment of two internal constants within the measuring head. These constants are the spindle multiplier constant (SMC) and the shear rate constant (SRC). The spindle multiplier constant is used to calculate the viscosity in Poise and is found by testing different SMC numbers while taking viscosity measurements in the calibration oil. The SRC is used to calculate the shear rate and the shear stress based on the spindle dimensions, effectively accounting for end effects. The shear rate is calculated by multiplying the SRC by the RPM. From this knowledge and the following equation the SRC can be calculated.

$$Shear\ Rate = \frac{2\omega R_c^2 R_b^2}{x^2\left(R_c^2 - R_b^2\right)} \qquad (2.8)$$

The shear rate is defined by the dimensions of the spindle and of the alumina crucible, where R_c represents the radius of the crucible, R_b is the radius of the spindle, x is the radius at which the shear rate is being calculated (in this case is the same as R_b), and ω is the angular velocity, where $\omega = \frac{2\pi}{60} N$ and N is the rpm. Once the SRC is calculated, it is entered into the measuring head as a constant and the SMC is found by trial and error on the standard oil (Brookfield Inc.). These new calibration constants were then tested on NIST 710a and 717a, which were run as unknowns (Figures 2.14 and 2.15). The accuracy of the measurements were calculated by comparing the measured data with the certified equations (Equations 2.6 and 2.7). The average absolute deviation (AAD)

between measured and certified values was 0.05 log units for 710a and 0.01 log units for 717a (Figures 2.14 and 2.15)

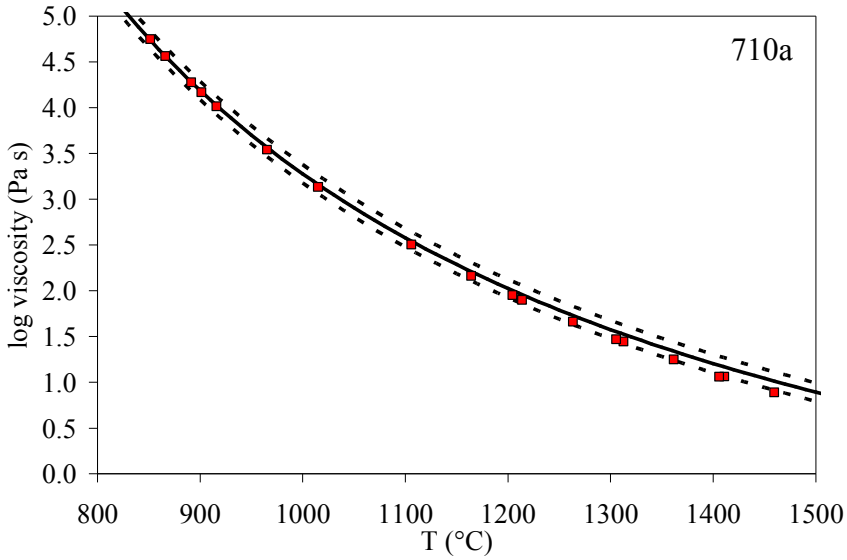

Figure 2.14. Data for NIST standard glass 710a borosilicate, using modified spindle geometry. Dotted lines represent ±0.1 log units from the certified TVF equation.

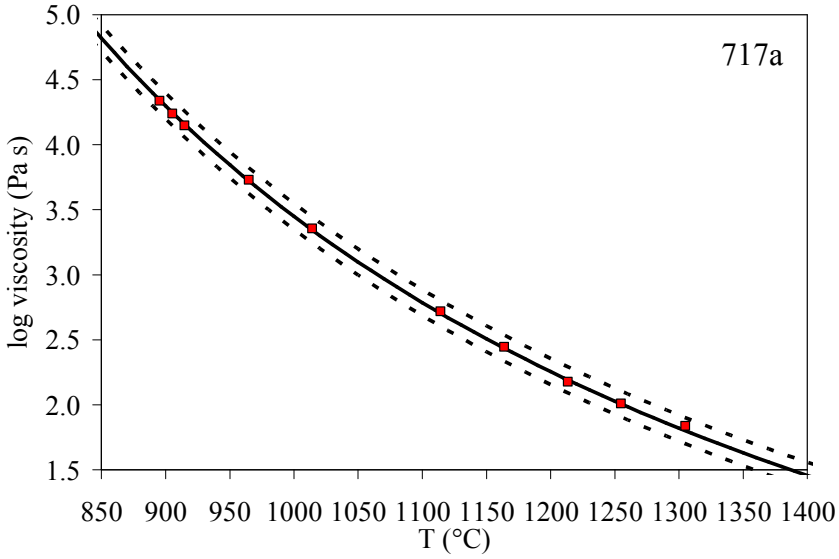

Figure 2.15. Data for NIST standard glass 717a soda-lime silicate, using modified spindle geometry. The dotted lines represent ±0.1 log units from the certified TVF equation.

Depending on the constraints of the experiment (temperature and sample composition) the specific spindle geometry would be selected. For all samples in this

study, the second spindle geometry was selected based on the high temperatures required for viscosity measurements under superliquidus temperatures.

2.6 Summary

- Nine glasses in the An-Fo-Q ternary system were synthesized based on dacitic lavas from Santiaguito lava dome and basaltic andesites from Santa Maria stratovolcano in Guatemala
- Eight glasses were synthesized in the An-Di-Fo ternary system based on tholeiitic basalts
- Density measurements and microprobe analyses were performed to verify the compositions and homogeneity of synthesized glasses
- Parallel Plate viscosity measurements were collected in the range of 10^{9}-10^{13} Pa s. The precision and accuracy were found to be 0.04 and 0.05 log units, respectively.
- Concentric Cylinder viscometry was utilized to measure viscosities at 10-10^{5} Pa s at superliquidus temperatures the accuracy was calculated and was found to be 0.05 log units for NBS 710a and 0.01 log units for NBS 717a. Precision was 0.02 log units based on duplicate runs of NBS 710a.

CHAPTER 3 –RESULTS AND DISCUSSION

"Learning without thought is labor lost; thought without learning is perilous."
–Confucius

3.1 Overview

This chapter is divided into four main sections: (1) glass composition, (2) liquid viscosity, (3) TVF modeling of viscosity as a function of temperature and composition, and (4) evolution of liquidus viscosity along liquid lines of descent. First, synthesized compositions are described using ternary diagrams, and electron microprobe analyses are reported. Next, the viscosity measurements of all samples are reported and discussed, including TVF equations with fitted *A*, *B*, and *C* parameters for each sample. Next, TVF modeling was also performed using a constant *A* parameter as determined for the diopside-anorthite-albite system by Russell and Giordano (2005). Two prediction models based on adapting the TVF equation, which calculates the viscosity along each series trajectory from anorthite based on composition, are described. Finally, this chapter concludes with a discussion of the viscosity of liquidus compositions for each series in order to determine the chemical effect of progressive crystallization on the residual liquid viscosity.

3.2 Composition of Glasses

Three series of CaO-MgO-Al_2O_3-SiO_2 (CMAS) glasses were synthesized in the anorthite-forsterite-quartz and the anorthite-diopside-forsterite ternary systems. In total, seventeen different glasses were made and their compositions were verified by electron microprobe analysis (Table 3.1 a, b.). Nine glasses in the An-Fo-Q ternary system correlate to dacitic lavas from Santiaguito and basaltic andesites from Santa Maria

Volcanoes in Guatemala. Eight glasses with compositions in the An-Di-Fo ternary system were synthesized to represent tholeiitic basalts. Each sample name consists of two letters in uppercase which describes the series they belong to, as well as a number which represents the mole % anorthite for that composition. For example, BA52 represents the synthesis in the BA (basalt) series in the anorthite-diopside-forsterite system with 52 mole percent normative anorthite.

Eight compositions were synthesized in the first series along the An-$Di_{90}Fo_{10}$ (wt. %) pseudobinary in the anorthite-forsterite-diopside system. This series is identified by "BA" (Figure 3.1). Two series are located in the anorthite-forsterite-quartz system (Figure 3.2). The first series, consisting of four glasses labeled "SM" (Santa Maria), lies approximately on the anorthite-enstatite binary between anorthite and the An-En cotectic; the second series, denoted by "SA" (Santiaguito), contains five glasses and lies between the anorthite and the An-En-Q ternary eutectic. Electron microprobe analyses are reported in Table 3.1 along with the normative mineralogy, glass density, molar mass, NBO/T, alumina index, and SM (structure modifier parameter, to be discussed later) for all compositions. If a melt has a high NBO/T value it is considered to be depolymerized, and will typically have a lower viscosity than a highly polymerized melt with a low NBO/T. For CMAS glasses NBO/T is calculated, based on mole percent oxide, using the following equation: $NBO/T=(2(CaO+MgO-Al_2O_3))/(SiO_2+2Al_2O_3)$ (Mysen and Richet 2005). All tables and graphs will list the synthesized melts in ascending order of NBO/T with increasing depolymerization as the melt composition moves away from anorthite. In all cases, the most anorthite-rich melts have the lowest NBO/T and highest viscosities.

Table 3.1 a.
Compositions of synthetic glasses in the Anorthite-Diopside-Forsterite system.

	BA81	BA58	BA52	BA42	BA36	BA24	BA11	BA0
wt % oxides								
SiO_2	43.35 (0.21)[c]	46.00 (0.18)	46.21 (0.18)	47.67 (0.13)	48.50 (0.15)	49.39 (0.21)	51.52 (0.25)	53.32 (0.14)
Al_2O_3	32.42 (0.19)	25.11 (0.10)	22.74 (0.24)	19.16 (0.13)	16.71 (0.08)	11.68 (0.06)	6.06 (0.07)	0.44[d] (0.02)
MgO	3.39 (0.03)	7.97 (0.07)	9.06 (0.09)	11.46 (0.09)	13.00 (0.05)	15.93 (0.11)	19.66 (0.09)	22.86 (0.08)
CaO	20.61 (0.07)	21.31 (0.12)	21.41 (0.05)	21.82 (0.03)	21.98 (0.09)	22.24 (0.11)	22.68 (0.06)	23.25 (0.17)
Total	99.78 (0.50)	100.39 (0.47)	99.43 (0.56)	100.11 (0.38)	100.19 (0.37)	99.23 (0.49)	99.93 (0.47)	99.87 (0.41)
mol % oxides								
SiO_2	48.39	48.17	48.11	47.95	47.89	47.56	47.40	47.47
Al_2O_3	21.32	15.49	13.95	11.35	9.72	6.63	3.29	0.00
MgO	5.65	12.44	14.07	17.19	19.14	22.87	26.96	30.35
CaO	24.64	23.90	23.88	23.51	23.25	22.94	22.35	22.18
norm. min. (mol%)								
An	80.53	57.55	52.27	42.20	35.51	23.83	11.41	0.00
Fo	3.45	7.53	8.46	10.25	11.43	13.50	15.71	15.56
Di	16.02	34.92	39.27	47.56	53.05	62.67	72.88	84.44
density (g/cm^3)	2.693	2.741	2.770	2.783	2.735	2.804	2.800	2.823
molar mass (g)	66.91	63.15	62.19	60.49	59.44	57.41	55.23	53.19
NBO/T[a]	0.20	0.53	0.63	0.83	0.97	1.29	1.71	2.21
Al/(Al+Si)	0.47	0.39	0.37	0.32	0.29	0.22	0.12	0.00
SM[b]	30.29	36.34	37.94	40.70	42.39	45.81	49.31	52.53

[a]NBO/T = $(2(CaO+MgO-Al_2O_3))/(SiO_2+Al_2O_3+Al_2O_3)$ Calculation based on Mysen and Richet (2005)

[b]SM parameter = (CaO+MgO) Calculation based on Giordano and Dingwell (2003)

[c]Values are the standard deviations of 6 spots measured by the JEOL 733 Superprobe at Washington University-St.Louis.

[d]Alumina was not added to this sample, all calculations were performed assuming 0 wt% Al_2O_3.

Table 3.1 b.
Compositions of synthetic glasses in the Anorthite-Forsterite-Quartz system.

	SM66	SM52	SM44	SM36	SA55	SA47	SA42	SA31	SA23
wt % oxides									
SiO_2	44.29 (0.18)[c]	46.25 (0.18)	47.08 (0.15)	48.95 (0.20)	48.93 (0.32)	50.98 (0.23)	52.33 (0.20)	55.72 (0.11)	59.08 (0.15)
Al_2O_3	30.83 (0.09)	28.68 (0.12)	25.16 (0.11)	23.26 (0.11)	31.26 (0.11)	29.02 (0.04)	27.40 (0.08)	23.48 (0.15)	19.78 (0.10)
MgO	7.74 (0.09)	10.45 (0.06)	13.57 (0.08)	16.30 (0.04)	3.74 (0.05)	4.76 (0.02)	5.59 (0.04)	7.34 (0.08)	9.20 (0.07)
CaO	16.45 (0.12)	14.84 (0.03)	13.35 (0.05)	12.09 (0.08)	16.22 (0.06)	15.23 (0.07)	14.42 (0.04)	12.43 (0.04)	10.40 (0.06)
Total	99.31 (0.48)	100.22 (0.39)	99.16 (0.39)	100.60 (0.43)	100.14 (0.54)	99.98 (0.36)	99.74 (0.36)	98.97 (0.38)	98.46 (0.38)
mol % oxides									
SiO_2	48.34	48.88	48.82	48.99	54.19	55.73	56.72	59.39	61.81
Al_2O_3	19.83	17.86	15.37	13.72	20.40	18.69	17.50	14.75	12.19
MgO	12.60	16.47	20.98	24.32	6.17	7.75	9.04	11.67	14.35
CaO	19.24	16.80	14.83	12.97	19.25	17.83	16.74	14.19	11.65
norm. min.(mol%)									
An	66.10	52.36	43.64	35.99	55.10	47.06	41.89	31.40	23.24
Fo	21.65	25.67	30.87	33.75	8.83	10.23	11.30	12.91	14.31
Q	12.26	21.97	25.50	30.26	36.08	42.71	46.80	55.69	62.46
density (g/cm^3)	2.691	2.702	2.704	2.726	2.647	2.647	2.619	2.598	2.565
molar mass (g)	65.12	63.63	61.77	60.50	66.63	65.66	64.95	63.38	61.88
NBO/T[a]	0.27	0.36	0.51	0.62	0.11	0.15	0.18	0.25	0.32
Al/(Al+Si)	0.45	0.42	0.39	0.36	0.43	0.40	0.38	0.33	0.28
SM[b]	31.84	33.27	35.81	37.29	25.42	25.58	25.78	25.86	26.00

[a]NBO/T = $(2(CaO+MgO-Al_2O_3))/(SiO_2+Al_2O_3+Al_2O_3)$ Calculation based on Mysen and Richet (2005)

[b]SM parameter = (CaO+MgO) Calculation based on Giordano and Dingwell (2003)

[c]Values in parentheses are the standard deviations of 6 spots measured by the JEOL 733 Superprobe at Washington University-St.Louis.

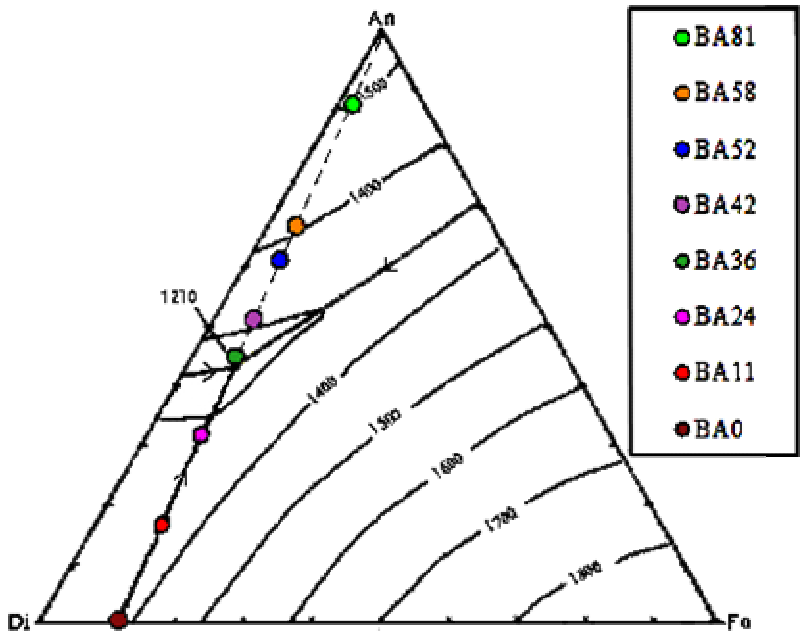

Figure 3.1. An-Di-Fo with BA series (wt. %, 1 atm) (Bowen 1915 and Morse 1980).

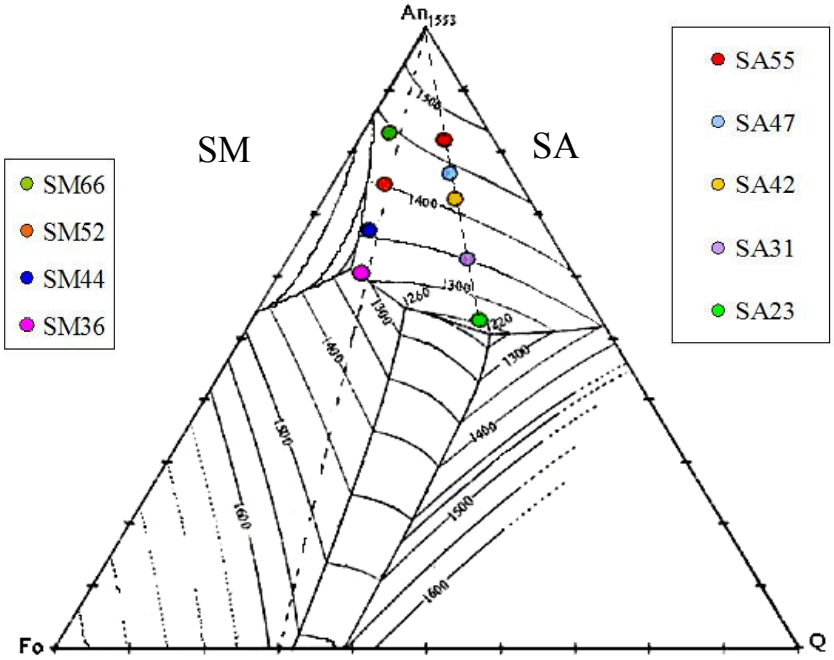

Figure 3.2. An-Fo-Q with SM and SA series (wt. %, 1 atm) (Anderson 1915).

3.3 Melt Viscosities

The viscosity data are presented in four separate tables divided by viscometer (parallel plate and concentric cylinder, respectively) and the ternary system they are

located in (Table 3.2 a, b, c, d). By measuring over a viscosity range of thirteen orders of magnitude, the non-Arrhenian behavior of the melts can be observed; if only a small temperature range was examined the relationship might be construed as Arrhenian. This also allows for interpolation within the subliquidus, supersolidus temperature range that is experimentally inaccessible to the techniques used here.

The viscosity data from the previous tables were then graphed against inverse temperature in Kelvin for each series. All points on the following graphs represent the viscometer data; the lines represent a TVF equation (Equation 1.5) for each composition (Figure 3.3 a, b, c). In order to interpolate viscosity at temperatures between the measured ranges, the empirical TVF equation was applied (Equation 3.1).

$$\log \eta = A + \frac{B}{T - C} \qquad (3.1)$$

The TVF equation has three adjustable parameters denoted by *A*, *B*, and *C* whose values are determined using the raw viscosity data using Kaleidagraph graphing software. These parameters for all series are presented in Table 3.3. Along with the parameters in Table 3.3, the glass transition temperature and the fragility for each composition is reported. Fragility is calculated by F_D=C/B, which represents the two extreme types of liquids and their sensitivity of the liquid to temperature changes. A high fragility value corresponds to fragile liquids (non-Arrhenian) and low F values correspond to strong liquids (Arrhenian-like). Also present in the figures and Table 3.3 is the TVF equation for anorthite. This value was not obtained in this study but represents the compilation of previous experimental data and an empirical TVF fit performed by Russell and Giordano (2005). The anorthite TVF parameters determined by Russell and Giordano (2005) are used in all following tables and figures unless otherwise denoted.

Table 3.2 a.
Low temperature data for Anorthite-Diopside-Forsterite samples. Viscosities are reported in Pa s.

BA81		BA58		BA52		BA42		BA36		BA24		BA11		BA0	
T (K)	log η	T (K)	log η	T (K)	log η	T (K)	log η	T (K)	log η	T (K)	log η	T (K)	log η	T (K)	log η
1072.7	12.30[c]	1032.3	12.13[c]	1022.4	12.36[b]	1006.7	12.57[b]	992.8	12.83[b]	1007.3	11.80[c]	992.5	12.68[d]	992.6	12.43[b]
1097.5	11.25[c]	1042.5	11.68[d]	1032.6	11.89[a]	1018.0	12.05[b]	1002.6	12.44[a]	1007.4	11.84[b]	1007.2	11.68[c]	996.7	12.07[c]
1097.7	11.34[d]	1052.3	11.25[d]	1042.7	11.40[a]	1022.5	11.72[c]	1012.4	11.95[a]	1017.3	11.38[b]	1012.3	11.53[d]	1002.9	11.81[b]
1107.4	10.93[d]	1057.2	11.08[c]	1047.1	11.27[b]	1027.4	11.52[b]	1017.6	11.64[b]	1017.3	11.33[c]	1017.4	11.20[c]	1006.3	11.64[c]
1107.6	10.84[c]	1062.6	10.82[d]	1052.3	10.98[a]	1032.4	11.26[c]	1022.6	11.48[a]	1027.3	10.89[b]	1022.1	11.02[d]	1011.6	11.26[b]
1117.3	10.46[c]	1067.2	10.67[c]	1057.2	10.87[b]	1037.1	11.10[b]	1027.5	11.20[b]	1027.4	10.84[c]	1027.0	10.71[c]	1017.4	10.92[c]
1117.6	10.51[d]	1072.5	10.43[d]	1062.1	10.57[a]	1042.3	10.82[c]	1032.4	11.06[a]	1037.2	10.40[c]	1032.4	10.53[d]	1022.4	10.64[b]
1125.2	10.22[d]	1077.6	10.25[c]	1067.5	10.44[b]	1047.3	10.69[b]	1036.8	10.81[b]	1037.3	10.43[b]	1037.4	10.23[c]	1027.4	10.37[c]
1125.3	10.15[c]	1082.4	10.05[d]	1072.3	10.16[a]	1052.5	10.40[c]	1042.4	10.62[a]	1047.3	9.97[c]	1042.4	10.02[d]	1032.3	10.08[b]
1135.5	9.83[d]	1087.5	9.86[c]	1077.4	10.06[b]	1062.3	10.00[c]	1047.4	10.37[b]	1047.5	9.97[b]	1047.3	9.80[c]	1036.3	9.90[c]
1135.6	9.76[c]	1089.8	9.77[d]	1082.7	9.79[a]	1072.5	9.60[c]	1052.5	10.15[a]	1054.6	9.67[c]	1049.9	9.70[d]	1041.1	9.66[b]
1145.5	9.41[c]	1095.7	9.56[c]	1087.6	9.66[b]	1082.7	9.21[c]	1057.5	9.95[b]	1055.0	9.63[b]	1054.9	9.49[c]	1044.3	9.47[c]
1145.7	9.46[d]	1100.6	9.38[d]	1090.4	9.50[a]			1060.0	9.82[a]	1064.8	9.26[c]			1049.9	9.17[b]
1152.8	9.20[d]	1103.4	9.27[c]	1094.3	9.36[b]			1065.1	9.67[b]	1065.4	9.19[b]				
1152.9	9.13[c]	1107.5	9.11[d]	1098.0	9.21[a]			1070.3	9.40[a]	1073.7	8.86[b]				
								1074.4	9.29[b]	1075.3	8.87[c]				
								1078.0	9.09[a]						

[a,b,c,d]Denotes different cylinders.

Table 3.2 b.
High temperature data for Anorthite-Diopside-Forsterite series. Viscosities are reported in Pa s.

BA58		BA52		BA42		BA36		BA24		BA11		BA0	
T (K)	log η	T (K)	log η	T (K)	log η	T (K)	log η	T (K)	log η	T (K)	log η	T (K)	log η
1697.8	0.45	1678.7	0.54	1591.0	1.00	1600.6	0.75	1605.3	0.44	1679.2	-0.13	1678.7	-0.26
1698.3	0.43	1688.5	0.50	1600.6	0.90	1620.3	0.65	1619.6	0.37	1694.4	-0.21	1685.2	-0.30
1707.6	0.42	1698.0	0.46	1620.4	0.76	1639.5	0.54	1659.2	0.18	1698.6	-0.20	1695.7	-0.34
1717.4	0.39	1707.9	0.43	1638.4	0.67	1639.7	0.55	1678.6	0.10	1708.5	-0.22	1698.3	-0.33
1723.7	0.30	1717.6	0.40	1639.9	0.65	1659.3	0.45	1695.3	0.02	1718.0	-0.23	1707.7	-0.36
1736.9	0.32	1723.3	0.32	1659.4	0.55	1677.2	0.39	1698.3	0.04	1737.4	-0.28	1717.5	-0.40
1746.8	0.29	1737.2	0.32	1675.8	0.45	1678.8	0.36	1717.6	-0.03	1756.7	-0.31		
1756.4	0.27	1746.8	0.30	1679.0	0.46	1698.3	0.27	1746.7	-0.13	1775.9	-0.35		
1775.6	0.21	1756.5	0.26	1698.5	0.39	1717.7	0.19	1756.3	-0.15	1790.2	-0.39		
1790.2	0.16	1775.8	0.18	1718.0	0.31	1737.2	0.12	1789.9	-0.28				
1804.6	0.09	1805.0	0.06	1737.5	0.24	1756.7	0.02						
1823.7	0.01	1824.7	0.01	1756.8	0.20	1774.3	-0.03						
				1776.4	0.13	1774.4	-0.03						
				1786.0	0.09								
				1824.7	-0.03								

Table 3.2 c.
Low temperature data for Anorthite-Forsterite-Quartz samples. Viscosities are reported in Pa s.

SM66		SM52		SM44		SM36		SA55		SA47		SA42		SA31		SA23	
T (K)	log η	T (K)	log η	T (K)	log η	T (K)	log η	T (K)	log η	T (K)	log η	T (K)	log η	T (K)	log η	T (K)	log η
1062.4	12.17[a]	1041.8	12.26[d]	1032.3	12.51[a]	1012.8	12.54[b]	1072.5	12.56[c]	1052.3	12.96[c]	1052.4	12.62[c]	1042.1	12.74[a]	1032.6	12.58[c]
1082.6	11.32[a]	1051.9	11.84[d]	1042.2	12.07[b]	1021.8	12.08[b]	1072.7	12.49[b]	1062.4	12.67[c]	1072.4	11.99[c]	1042.9	12.82[c]	1057.3	11.74[c]
1092.1	10.98[b]	1052.2	11.94[c]	1052.4	11.54[a]	1027.1	12.04[c]	1082.5	12.08[c]	1072.2	12.33[b]	1072.5	11.88[a]	1047.8	12.68[b]	1062.5	11.61[b]
1092.4	10.90[a]	1062.1	11.44[d]	1062.6	11.19[b]	1032.6	11.60[b]	1082.7	12.04[b]	1072.7	12.29[c]	1072.7	11.86[b]	1051.9	12.47[c]	1067.4	11.40[c]
1102.5	10.47[b]	1062.3	11.47[b]	1072.3	10.86[b]	1037.2	11.48[c]	1092.6	11.67[c]	1082.5	11.88[c]	1082.3	11.56[c]	1052.6	12.30[a]	1072.9	11.20[b]
1102.6	10.55[a]	1062.4	11.52[c]	1072.5	10.78[a]	1042.6	11.17[b]	1092.6	11.65[b]	1089.1	11.71[b]	1082.5	11.47[b]	1057.2	12.31[b]	1077.7	11.03[c]
1112.4	10.06[b]	1072.2	11.06[c]	1082.2	10.46[b]	1047.3	11.05[c]	1102.6	11.26[c]	1092.4	11.57[b]	1082.5	11.47[a]	1062.2	12.06[c]	1082.5	10.81[b]
1112.4	10.14[a]	1072.6	11.03[d]	1082.7	10.44[a]	1052.2	10.77[b]	1102.6	11.23[b]	1092.6	11.51[c]	1092.4	11.11[b]	1062.6	11.93[a]	1092.5	10.45[b]
1122.2	9.75[b]	1082.1	10.65[c]	1092.4	10.11[b]	1057.2	10.66[c]	1112.6	10.87[b]	1102.4	11.11[c]	1092.5	11.07[a]	1067.8	11.90[b]	1097.5	10.33[c]
1132.7	9.33[b]	1082.3	10.64[d]	1092.5	10.02[a]	1062.3	10.39[b]	1112.7	10.85[c]	1102.6	11.14[b]	1092.5	11.19[c]	1072.2	11.62[a]	1102.3	10.12[b]
		1082.4	10.66[b]	1102.4	9.79[b]	1067.3	10.27[c]	1122.2	10.49[b]	1112.4	10.75[c]	1102.4	10.71[a]	1072.7	11.65[c]	1107.4	9.99[c]
		1092.4	10.26[c]	1102.7	9.68[a]	1072.6	9.99[b]	1122.6	10.49[c]	1112.4	10.80[b]	1102.7	10.79[c]	1077.8	11.49[b]	1112.5	9.81[b]
		1092.5	10.26[b]	1112.3	9.49[b]	1077.6	9.87[c]	1132.5	10.12[c]	1122.5	10.40[c]	1102.8	10.68[b]	1082.2	11.18[a]	1117.1	9.68[c]
		1092.9	10.24[d]	1112.5	9.55[a]	1077.7	9.78[b]	1132.7	10.13[b]	1122.6	10.45[b]	1112.4	10.40[b]	1082.5	11.26[c]	1122.3	9.51[b]
		1102.4	9.85[d]	1123.1	9.11[b]	1082.9	9.66[c]	1142.5	9.79[b]	1132.5	10.08[b]	1112.5	10.44[c]	1087.7	11.10[b]	1127.6	9.35[c]
		1102.5	9.90[b]			1092.1	9.26[a]	1142.7	9.71[c]	1132.6	10.06[c]	1112.6	10.38[a]	1092.3	10.82[a]	1136.1	9.08[b]
		1102.6	9.89[c]			1106.4	8.80[a]	1151.5	9.53[b]	1142.7	9.71[b]	1121.9	9.98[a]	1092.6	10.90[c]	1136.1	9.09[b]
		1112.5	9.54[b]			1106.5	8.80[a]	1151.8	9.45[c]	1142.7	9.72[c]	1122.5	10.10[c]	1097.5	10.73[b]	1137.8	9.06[c]
		1112.5	9.54[c]					1156.2	9.24[c]	1151.6	9.43[c]	1122.6	10.02[b]	1102.1	10.48[a]	1140.9	8.99[c]
		1118.2	9.29[d]					1158.0	9.24[b]	1152.0	9.28[b]	1132.5	9.77[c]	1102.6	10.56[c]		
		1118.2	9.30[d]									1132.6	9.70[b]	1107.7	10.38[b]		
		1121.0	9.26[b]									1139.4	9.49[b]	1112.3	10.23[c]		
		1122.1	9.25[c]									1142.7	9.44[c]	1112.5	10.15[a]		
												1152.1	9.17[c]	1117.4	10.07[b]		
														1122.2	9.83[a]		
														1122.5	9.89[c]		
														1127.2	9.75[b]		
														1132.4	9.51[a]		
														1132.6	9.62[c]		
														1137.7	9.44[b]		
														1142.0	9.31[b]		
														1142.4	9.21[a]		
														1142.6	9.35[c]		
														1148.9	9.03[a]		

[a,b,c,d]Denotes different cylinders.

Table 3.2 d.
High temperature data in the Anorthite-Forsterite-Quartz system. Viscosities are reported in Pa s.

SM66		SM52		SM44		SM36		SA55		SA47		SA42		SA31		SA23	
T (K)	log η	T (K)	log η	T (K)	log η	T (K)	log η	T (K)	log η	T (K)	log η	T (K)	log η	T (K)	log η	T (K)	log η
1789.7	0.41	1773.3	0.43	1773.5	0.28	1594.2	1.12	1777.7	0.80	1777.7	0.65	1776.7	0.84	1620.4	1.84	1594.8	2.07
1799.4	0.37	1782.4	0.38	1783.6	0.25	1613.6	1.00	1787.3	0.76	1787.4	0.62	1783.6	0.74	1639.6	1.71	1614.1	1.93
1808.9	0.33	1783.6	0.39	1784.0	0.24	1638.1	0.86	1796.8	0.71	1797.3	0.59	1784.7	0.79	1640.0	1.71	1638.5	1.77
1818.5	0.29	1793.5	0.35	1793.6	0.21	1662.6	0.73	1806.5	0.67	1806.7	0.56	1793.8	0.74	1659.4	1.59	1638.6	1.77
1828.2	0.26	1803.6	0.31	1803.9	0.18	1673.9	0.68	1816.2	0.63	1816.7	0.52	1804.0	0.69	1674.4	1.49	1663.0	1.61
1837.9	0.22	1814.1	0.27	1814.2	0.15	1682.1	0.63	1825.9	0.58	1826.2	0.50	1814.2	0.63	1679.0	1.47	1673.5	1.56
1847.6	0.18	1824.4	0.22	1817.6	0.13	1701.6	0.53	1835.5	0.54	1836.0	0.46	1824.3	0.58	1698.4	1.35	1682.7	1.49
1857.4	0.15	1834.4	0.18	1824.5	0.10	1721.2	0.44	1845.1	0.50	1845.4	0.44	1833.3	0.54	1718.0	1.23	1702.3	1.37
1864.6	0.09	1843.5	0.14	1833.7	0.06	1740.7	0.35	1854.8	0.46	1855.3	0.40	1843.6	0.49	1737.4	1.12	1721.6	1.26
1867.2	0.10	1854.7	0.09	1843.6	0.02	1760.4	0.26	1866.8	0.39	1864.8	0.37	1853.6	0.43	1756.6	1.02	1740.9	1.16
1870.2	0.09	1863.9	0.04	1853.8	-0.02	1775.1	0.23					1863.9	0.38	1761.3	1.05	1747.7	1.18
				1864.4	-0.06	1776.6	0.18							1775.2	0.94	1760.5	1.06
														1776.2	0.93	1780.0	0.97
														1785.7	0.89	1789.6	0.93
														1824.3	0.72	1824.2	0.78

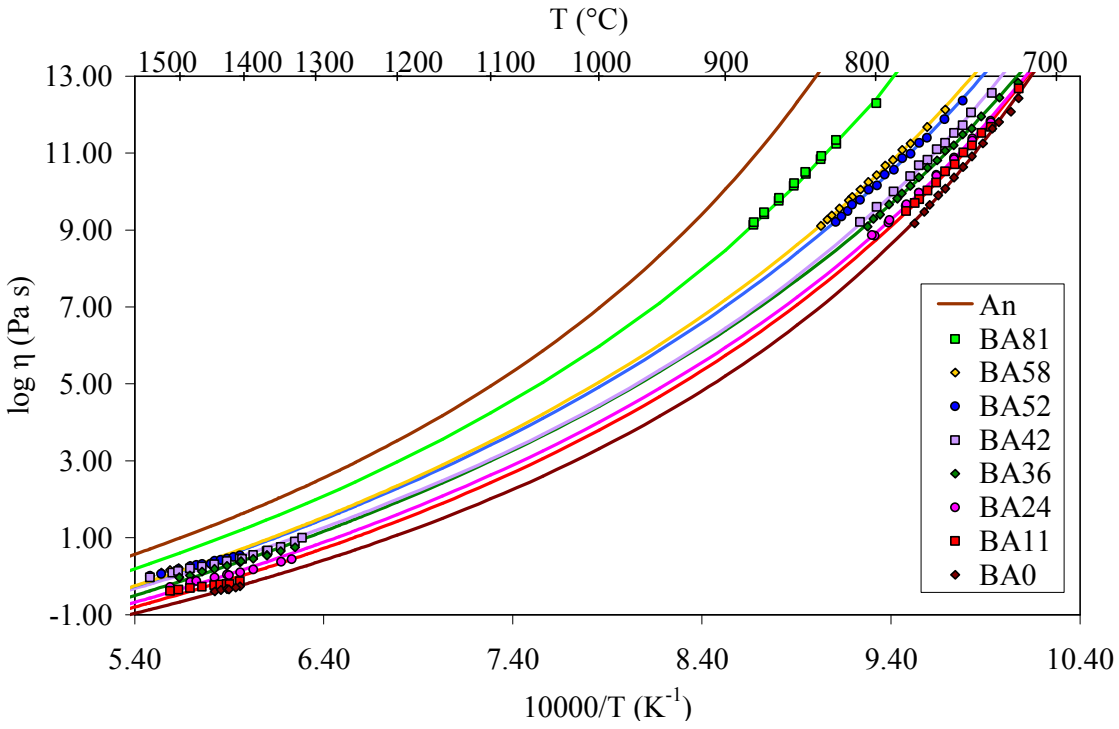

Figure 3.3 a. BA series (An-Di-Fo) viscosity data reported in log Pa s against the reciprocal of temperature plotted with TVF curves.

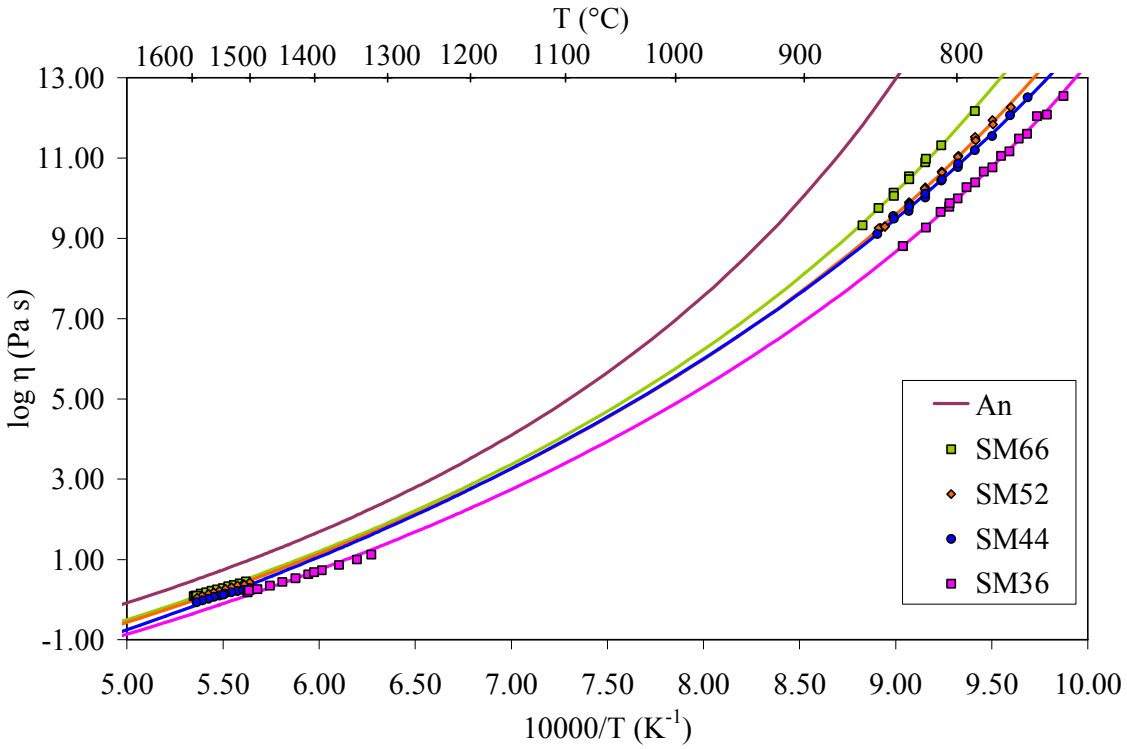

Figure 3.3 b. SM series, (An-Fo-Q) viscosity data reported in log Pa s against the reciprocal of temperature plotted with TVF curves.

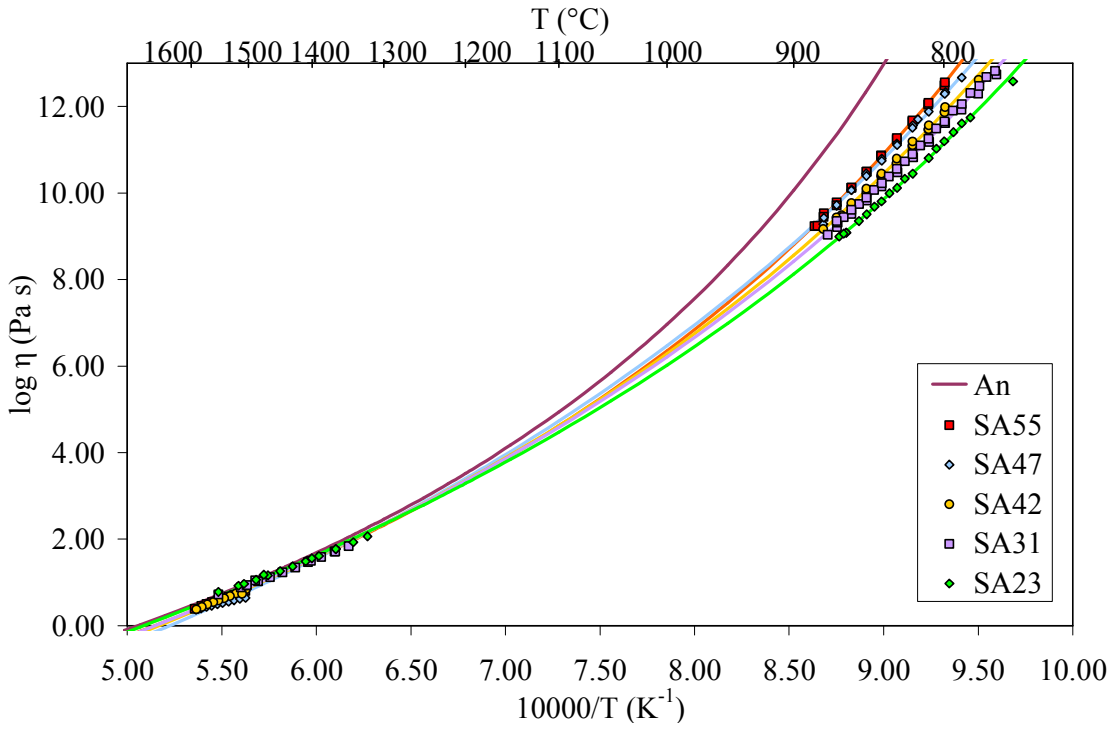

Figure 3.3 c. SA (An-Fo-Q) viscosity data and TVF curves.

As seen in the above graphs, anorthite has the highest viscosity in all series. The BA series (basalt) lies approximately along the An-$Di_{90}Fo_{10}$ (wt. %) from anorthite and runs through the eutectic and along the Fo-Di cotectic. This series has a large range in NBO/T values, from 0.20 (BA81) to 2.21 (BA0) (Table 3.1. a). BA81 has the fewest number of nonbridging oxygens resulting in the highest viscosity, disregarding anorthite. BA0 is a binary mixture of forsterite and diopside, which results in a very depolymerized melt and consequently very low viscosities. BA0 appears to exhibit slightly more non-Arrhenian behavior than the other compositions measured in this series. This could be due to the total absence of alumina in the melt, which greatly affects the melt structure and results in a very depolymerized melt. There is a greater spread of viscosity values at the lower temperatures and smaller differences in viscosity at higher temperatures.

Table 3.3.
Parameters for TVF equation for each series, $\log_{10} \eta = A + B/(T-C)$

Sample	A(Pa s)[a]	B(Pa s K^{-1})	C (K)	T_{12}(K)[b]	F_D[c]	AAD[d]
An[e]	-4.71	5572	796	1129	0.14	
BA81[f]	-5.33	6243	720.8	1081	0.12	0.07
BA58	-5.80 (0.20)	6567 (290)	667.7 (12.9)	1037	0.10	0.05
BA52	-5.67 (0.18)	6396 (249)	669.0 (11.1)	1031	0.10	0.05
BA42	-5.06 (0.19)	5470 (253)	698.1 (11.6)	1019	0.13	0.04
BA36	-5.71 (0.14)	6193 (193)	661.4 (8.4)	1011	0.11	0.07
BA24	-5.41 (0.15)	5489 (192)	689.8 (8.9)	1005	0.13	0.05
BA11	-5.33 (0.19)	5194 (242)	703.7 (11.3)	1003	0.14	0.06
BA0	-4.90 (0.08)	4372 (95)	740.7 (4.6)	999	0.17	0.03
SM66	-5.44 (0.15)	6428 (221)	698.9 (10.1)	1067	0.11	0.04
SM52	-5.78 (0.09)	6909 (131)	660.0 (5.8)	1049	0.10	0.03
SM44	-6.47 (0.15)	7923 (248)	614.2 (10.4)	1043	0.08	0.03
SM36	-5.75 (0.15)	6566 (209)	655.5 (9.1)	1025	0.10	0.05
SA55	-5.55 (0.07)	6975 (103)	687.0 (4.5)	1084	0.10	0.03
SA47	-6.56 (0.20)	8479 (324)	622.4 (12.9)	1079	0.07	0.06
SA42	-6.12 (0.13)	8013 (202)	627.3 (8.4)	1070	0.08	0.02
SA31	-6.10 (0.13)	8092 (199)	615.7 (8.0)	1063	0.08	0.05
SA23	-5.73 (0.16)	7745 (239)	614.0 (10.2)	1051	0.08	0.04

[a] Numbers in parentheses are absolute uncertainties.

[b] T_{12} indicates the temperature at which the viscosity is 10^{12} Pa s, which is used as the effective glass transition temperature.

[c] The fragility is calculated where $F_D = C/B$ (Russell and Giordano 2005).

[d] AAD is the absolute average deviation between measured values and those calculated using the TVF equation.

[e] Anorthite data from Russell and Giordano 2005 p.5334 table 1 with root mean square error of 0.15.

[f] High temperature data could not be obtained for BA81. TVF parameters used are described in the S_{mix} section.

The SM series also demonstrates the compositional dependence of viscosity. The SM series exhibits a smaller range in NBO/T than the BA series (0.27-0.62) (Table 3.1). Again the viscosities gradually decrease as NBO/T increases, and the greater compositional dependence of viscosity at lower temperatures can be seen, but in this series the data merges toward a common viscosity value at higher temperatures.

In the SA series, similar to the other series, the most anorthite-rich, highly polymerized samples have the greatest viscosities and at lower temperatures larger

differences in viscosities are again apparent. The NBO/T values for the SA series demonstrate the smallest range from 0.11-0.32 and overall are the most polymerized of all series. At higher temperature, the viscosities of all samples again converge; however, in this series there is some crossover at about 1460°C suggesting that polymerization is not always a reliable indicator of relative viscosity over all temperature ranges.

Comparing the three series, the most viscous for a given anorthite content is SA (dacites), followed by SM (basaltic andesites), and finally the most fluid is the BA series (tholeiitic basalts). This stands to reason when the NBO/T values are examined and the most polymerized samples are found in SA, SM, and then BA (Figure 3.4a). The figure below demonstrates the different ranges for each series. The NBO/T ratio also dictates the order of viscosity within each series as well, illustrated by a plot of T_g against NBO/T (Figure 3.4a). For all series, except a couple of SA compositions at high temperatures, the more polymerized the melt, the greater the viscosity.

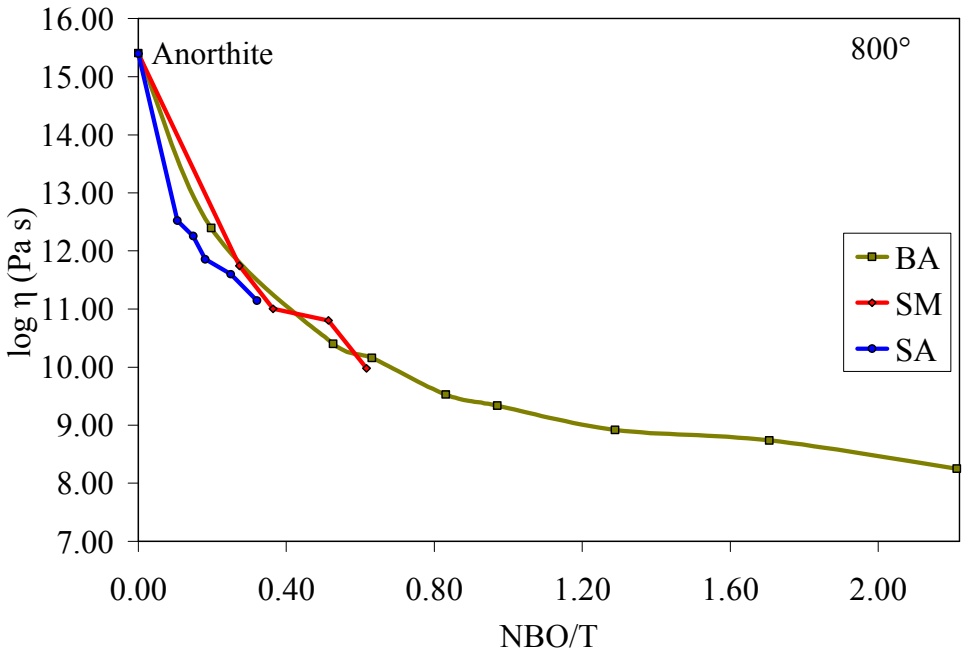

Figure 3.4 a. Viscosity as a function of NBO/T at 800°C. Symbols represent points calculated using the TVF equations given in Table 3.3.

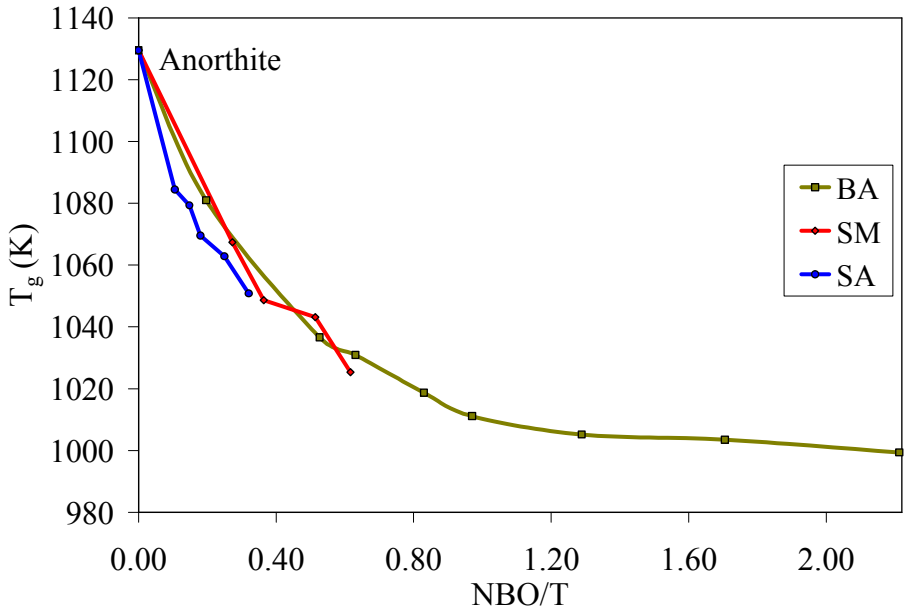

Figure 3.4 b. T_g as a function of NBO/T. Symbols represent points calculated using the TVF equations given in Table 3.3.

3.4 TVF equations

3.4.1 Constant A Parameter

This investigation allows for a different interpolation technique to verify the accuracy of the unconstrained TVF parameters utilized in Table 3.3 and Figure 3.3 as well as an opportunity to investigate the compositional dependence of the *A* parameter. As stated above the TVF equation has three internally adjustable variables; however, if it is assumed that all melts eventually converge to a single viscosity at very high temperatures the *A* parameter should be a constant. The Maxwell relationship states $\eta = G_\infty \tau$, where G_∞ is the shear modulus and τ is the structural relaxation time (Richet and Bottinga 1995). Knowing that *A* is equivalent to the viscosity at infinite temperature $A = G_\infty \tau$, where τ is approximately equivalent to the vibrational frequency of the silica network at 10^{-12} to 10^{-14} s (Dingwell and Webb 1989). G_∞ is approximately a constant

for silicate melts at 10^{10} Pascals because it was found that varies by less than a factor of ten (Dingwell and Webb 1989). Thus, A is also approximately constant. Russell and Giordano (2005) found *A* to be -5.06 in the diopside-albite-anorthite system. This results in the following TVF equation, which still contains two composition dependent parameters *B* and *C* (Equation 3.2).

$$\log \eta = -5.06 + \frac{B}{T - C} \qquad (3.2)$$

The experimental data was again plotted in the Kaleidagraph software in order to quantify the *B* and *C* parameters for each composition (Table 3.4).

Table 3.4.
Parameters for constant *A* TVF equation for each series, $\log_{10}$ η=A+B/(T-C)

Sample	A(Pa s)	B(Pa s K^{-1})[a]	C (K)	T_{12}(K)[b]	F_D[c]	AAD[d]
An[e]	-5.06	5092	696	994	0.14	
BA81	-5.06	6279 (97)	713.0 (6.3)	1081	0.11	0.04
BA58	-5.06	5544 (41)	714.1 (2.7)	1039	0.13	0.08
BA52	-5.06	5564 (37)	706.5 (2.4)	1033	0.13	0.07
BA42	-5.06	5465 (31)	698.0 (2.0)	1018	0.13	0.07
BA36	-5.06	5364 (36)	698.0 (2.4)	1012	0.13	0.07
BA24	-5.06	5056 (33)	709.9 (2.2)	1006	0.14	0.06
BA11	-5.06	4859 (38)	719.3 (2.5)	1004	0.15	0.07
BA0	-5.06	4548 (23)	732.4 (1.5)	999	0.16	0.03
SM66	-5.06	5871 (23)	724.6 (1.6)	1069	0.12	0.03
SM52	-5.06	5952 (33)	703.0 (2.2)	1052	0.12	0.05
SM44	-5.06	5823 (60)	705.9 (3.9)	1047	0.12	0.10
SM36	-5.06	5663 (38)	695.1 (2.5)	1027	0.12	0.07
SA55	-5.06	6282 (27)	717.3 (1.7)	1086	0.11	0.04
SA47	-5.06	6275 (76)	713.4 (4.8)	1081	0.11	0.12
SA42	-5.06	6421 (46)	695.6 (2.9)	1072	0.11	0.07
SA31	-5.06	6641 (42)	675.0 (2.7)	1064	0.10	0.08
SA23	-5.06	6772 (34)	655.8 (2.3)	1053	0.10	0.05

[a] Numbers in parentheses are absolute uncertainties.

[b] T_{12} indicates the temperature at which the viscosity is 10^{12} Pa s, which is used as the effective glass transition temperature.

[c] The fragility is calculated where F_D=C/B.

[d] AAD is the absolute average deviation between measured values and those calculated using the TVF equation.

[e] Anorthite data from Russell et al. 2005 p.5340 table 4 with root mean square error of 0.17.

The object of this modeling is to determine if a constant *A* parameter results in the most accurate fit to the viscosity data. These new TVF curves were then compared to the raw viscosity data. Using a constant *A* value in the new TVF curves does not generate a better fit than the unrestricted A parameter of the first TVF calculation; however, using constant *A* values still result in a very good fit. From Table 3.4 the overall AAD values from the viscosity data of all series is 0.07 log units and the maximum deviation for a single sample is 0.12 log units (SA47). The AAD is the summation of the absolute value of each deviation from the measured viscosity $\left(AAD = \frac{1}{n} \sum \left| x_i - x \right| \right)$. These are very good values, however, examining the parameters from a variable *A* value reported in Table 3.3 the overall average deviation is 0.04 log units with a maximum deviation of log 0.07 (for BA81 and BA36). In this case using a varying *A* value results in a slightly better fit to the viscosity data and will be used in all subsequent graphs and tables unless otherwise denoted.

3.4.2 Constructing a Predictive Viscosity Model Based on the TVF Equation

The next logical step is to attempt to predict viscosities for any composition and temperature along each series' trajectory from anorthite using the experimental data obtained. Two different methods were employed for this task. The first is an empirical approach, which applies a 3rd order polynomial to the data set; the second method applies the theory of the entropy of mixing, which results in a 2nd order polynomial.

3.4.2.1 3rd Order Polynomial Empirical Method

This empirical approach involves taking the *A*, *B*, and *C* parameters from the experimentally derived TVF curves, plotting them in Kaleidagraph, and finding the best fit curve in the form of a 3rd order polynomial for each of the parameters. A 3rd order

polynomial was not a good fit to the TVF parameters of the SM or the SA series; therefore, this technique was only attempted with the BA series (Figure 3.5).

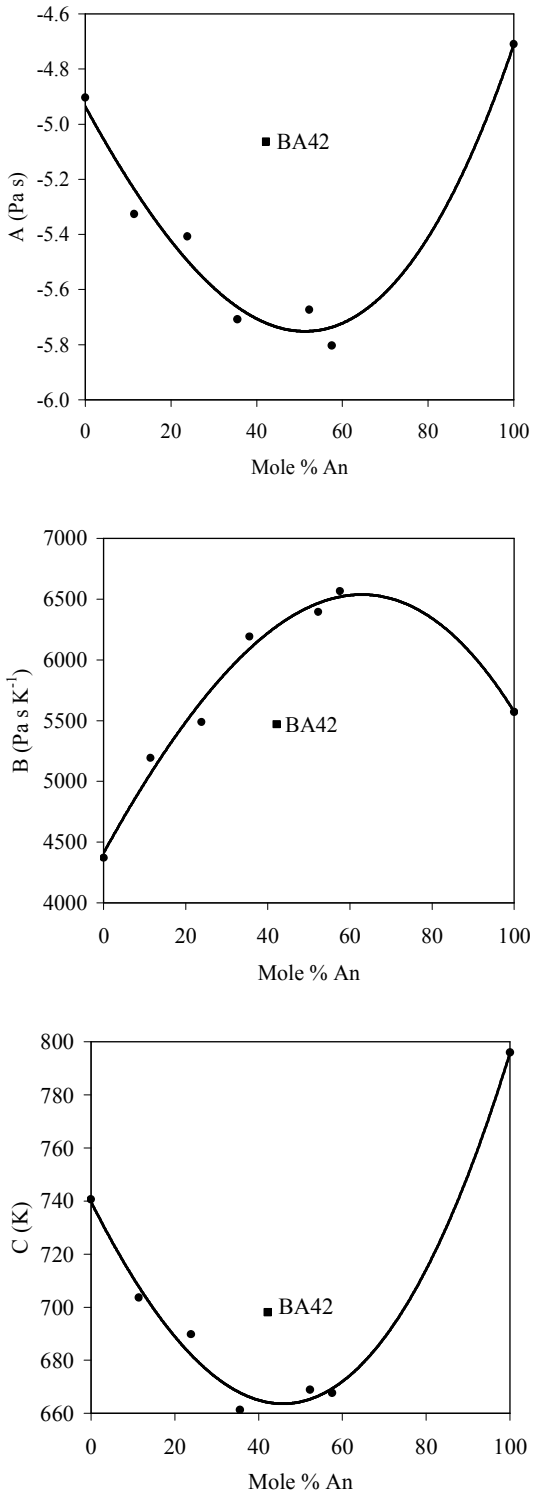

Figure 3.5. Third order polynomial fits to A, B, and C parameters for the BA series.

To generate this equation the parameters of two compositions were not used. The first was BA42 whose parameters did not correspond well with the other data (Figure 3.5); the second was BA81 because high temperature data could not be obtained and an experimental TVF curve could not be accurately generated using just low temperature data. Omitting these samples when generating the model presents the opportunity to test it. The results of the curve fit are the three following equations representing the value for a specific parameter as a function of mole % anorthite content, X:

$$A = -4.9357 + (-0.02848)\ X + 0.00017988\ X^2 + 0.0000012724\ X^3 \qquad (3.3)$$

$$B = 4411.4 + 61.072\ X + (-0.33043\ X^2) + (-0.0016408\ X^3) \qquad (3.4)$$

$$C = 739.8 + (-3.1429)\ X + 0.028279\ X^2 + 0.000087712\ X^3 \qquad (3.5)$$

The equations can be used to calculate a viscosity anywhere along the BA series for any temperature. This allows for a direct comparison of the exact temperature at which the viscosity measurements were gathered. Viscosity values were calculated and compared to the raw viscosity measurements as well as to their original TVF equations (from Table 3.3). The absolute average deviations are reported in Table 3.5. The calculated and measured viscosities agree very well even for BA42 and BA81, which were not used to generate this model. Unfortunately, this type of modeling was entirely empirical and only applicable to the BA series; therefore, a new method to predict the viscosity along each series was sought out.

Table 3.5.
Third order polynomial TVF model AAD.

Sample	n[a]	AAD_{data}[b]	AAD_{TVF}[c]
An		–	0.04
BA81	15	0.10	–
BA58	27	0.05	0.02
BA52	27	0.06	0.04
BA42	27	0.07	0.05
BA36	30	0.06	0.04
BA24	26	0.06	0.04
BA11	21	0.11	0.07
BA0	19	0.05	0.04
Overall Weighted Average		*0.07*	*0.04*

[a]n= number of viscosity measurements for each sample.
[b]AAD_{data}= absolute average deviation between 3rd order polynomial model with viscosity measurements.
[c]AAD_{TVF}= absolute average deviation between 3rd order polynomial model with experimental TVF equation.

3.4.2.2 Entropy of Mixing Model

As seen in the above figure (Figure 3.4), the TVF parameters display a distinct curvature. This parabolic shape is characteristic of thermodynamic mixing curves. From chapter 1, recall that $\log\eta = A_e + \frac{B_e}{TS^{conf}}$ (Equation 1.2). Configurational entropy includes a contribution from entropy of mixing: $S^{conf} = \Sigma x_i S_i^{conf} + S_{mix}$ *(3.6)* (Neuville and Richet 1991). Entropy of mixing is described by a 2nd order polynomial using a Margules parameter for entropy, here denoted W_S (Equation 3.7).

$$S_{mix} = W_s X_2 - W_s X_2^2 = W_S X_1 X_2 \qquad (3.7)$$

The value of each TVF parameter as a function of composition is given by Equation 3.8:

$$A,B,C = A_0 B_0 C_0 (1-X) + A_1 B_1 C_1 X + W_{A,B,C}[(1-X)X] \qquad (3.8)$$

Where X is the mole fraction of anorthite, A_0, B_0, or C_0 and A_1, B_1, or C_1 describes the parameter value for each series end-members, and $W_{A,\,B,\,C}$ is the Margules parameter for

each of the TVF parameters. For example, the equation below describes parameter *A* for the BA series.

$$A = -4.90(1 - X) + -4.71\,X + W_A\left[(1 - X)X\right] \qquad (3.9)$$

In this case, -4.90 is the A value for BA0 and -4.71 is the *A* value for anorthite. This results in the only unknown being the Margules parameter. Continuing with the BA series, all three parameters were plotted in Kaleidagraph, which resulted in the following graphs (Figure 3.6). The best fit Margules parameters derived by Kaleidagraph are shown in Table 3.6.

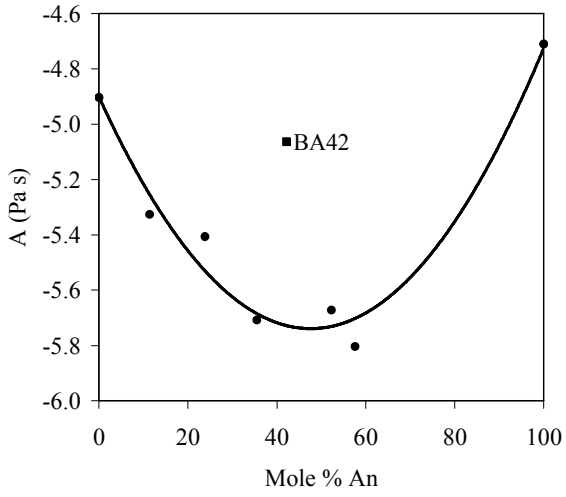

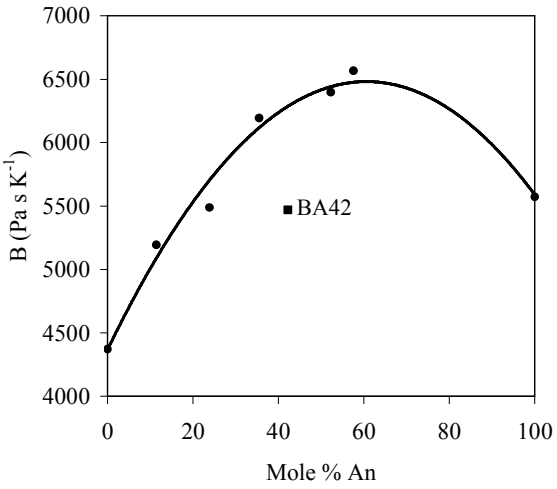

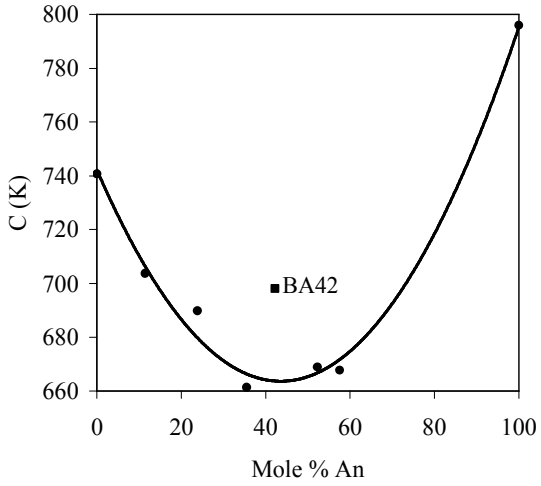

Figure 3.6. *A*, *B*, and *C* parameters for S_{mix} curve fit for BA series.

Table 3.6.
TVF end-members and mixing parameters for the BA series.

	End-Members		
	BA0	An	W[a]
A (Pa s)	-4.90	-4.71	-3.72 (0.16)
B (Pa s K^{-1})	4372	5572	5769 (237)
C (K)	740.7	796	-420.2 (11.1)

[a]Values in parentheses are absolute uncertainties.

The new prediction model was compared to the raw viscosity data and then against the TVF equations by calculating the absolute average deviation for each composition. The model was able to predict the values very well for the BA series (Table 3.7). This model can predict the viscosity of samples BA42 and BA81 very well, with an AAD of 0.07 for both samples, comparable to the AAD of TVF equations fitted directly to the measured data (0.04 and 0.07 respectively, Table 3.3). For this reason the TVF equation used for all graphs for composition BA81, which lacks high temperature data, was computed using this method.

Table 3.7.
Entropy of mixing TVF model AAD.

Sample	n[a]	AAD_{data}[b]	AAD_{TVF}[c]
An		—	0.04
BA81	15	0.07	—
BA58	27	0.06	0.04
BA52	27	0.05	0.03
BA42	27	0.07	0.05
BA36	30	0.05	0.03
BA24	26	0.05	0.03
BA11	21	0.13	0.10
BA0	19	0.03	0.00
Overall Weighted Average		*0.06*	*0.04*

[a]n= number of viscosity measurements for each sample.
[b]AAD_{data}= absolute average deviation between S_{mix} model with viscosity measurements.
[c]AAD_{TVF}= absolute average deviation between S_{mix} model with experimental TVF equation.

The SA and SM series models were generated using the same technique as described above for the BA series; their AAD values were not as good as for the BA series, but still better than 0.35 log units for all compositions. For the SM series, sample SM44 was not used in generating the model and can therefore be used to check the predictive power of the model. Below is a list of the calculated Margules parameters (Table 3.8) and AAD values (Table 3.9) for both An-Fo-Q series.

Table 3.8.
An-Fo-Q system end-member and mixing TVF parameters.

	End-Members		
	SM	An	W[a]
A (Pa s)	-5.75	-4.71	-1.90 (0.18)
B (Pa s K^{-1})	6565	5572	2504 (464)
C (K)	655.5	796	-241.5 (15.9)
	SA	An	
A (Pa s)	-5.73	-4.71	-3.12 (0.65)
B (Pa s K^{-1})	7745	5572	4380 (863)
C (K)	614.0	796	-233.0 (11.1)

[a]Values in parentheses are absolute uncertainties.

Table 3.9.
Entropy of mixing TVF model AAD.

Sample	n[a]	AAD_{data}	AAD_{TVF}
An		–	0.00
SM66	22	0.08	0.08
SM52	34	0.16	0.16
SM44	27	0.21	0.21
SM36	30	0.34	0.34
Overall Weighted Average		*0.21*	*0.20*
SA55	30	0.05	0.04
SA47	30	0.15	0.14
SA42	36	0.04	0.03
SA31	49	0.05	0.02
SA23	34	0.28	0.28
Overall Weighted Average		*0.11*	*0.09*

[a]n= number of viscosity measurements for each sample.
[b]AAD_{data}= absolute average deviation between S_{mix} model with viscosity measurements.
[c]AAD_{TVF}= absolute average deviation between S_{mix} model with experimental TVF equation.

Below, Figure 3.7 presents the mixing curves for the A, B, and C parameters for SM and SA series. The points are values of the TVF parameters from Table 3.3, and the solid lines represent the mixing curves. The AAD values for the SA series is much better than for the SM series (Table 3.9) but neither of these models are as accurate as the model determined for the BA series (Table 3.7). It is likely that a better model could be generated for these series if the SM and the SA series spanned the entire length of their phase diagram, from end-member to end-member, as the BA series does. More glasses would need to be synthesized to test this.

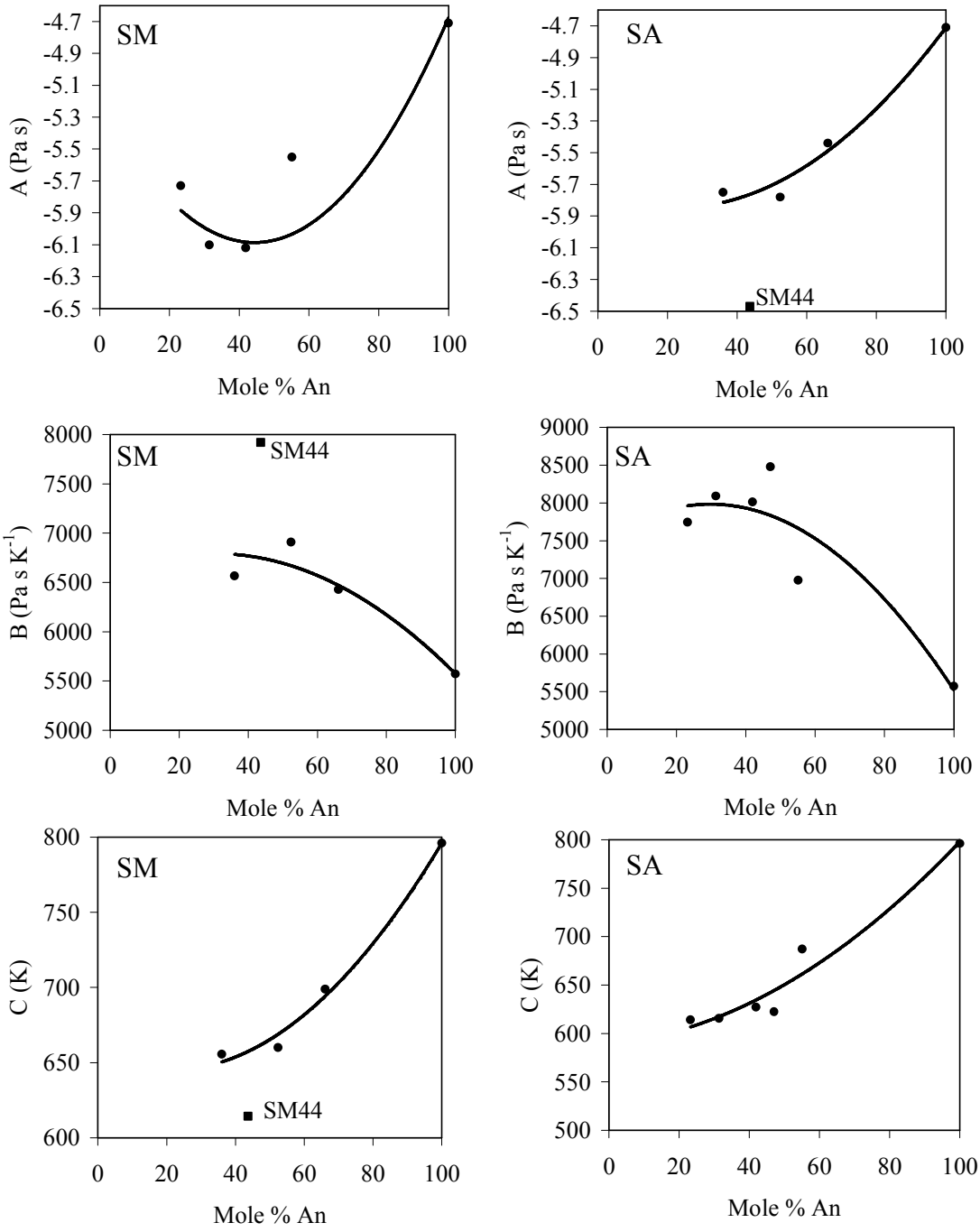

Figure 3.7. TVF parameters for SM and SA series plotted with their mixing curves.

3.5 Liquid Line of Descent

The liquid line of descent describes the compositional evolution of the liquid with decreasing temperature and progressive crystallization. Figure 3.8 shows the liquid lines

of descent for all three series. The viscosity of the liquid line of descent was determined using the ternary diagram and the viscosity data. The points on the graphs below represent the temperature at which the compositions are at their liquidus temperature. By connecting the points the viscosity of the liquid line of descent was defined.

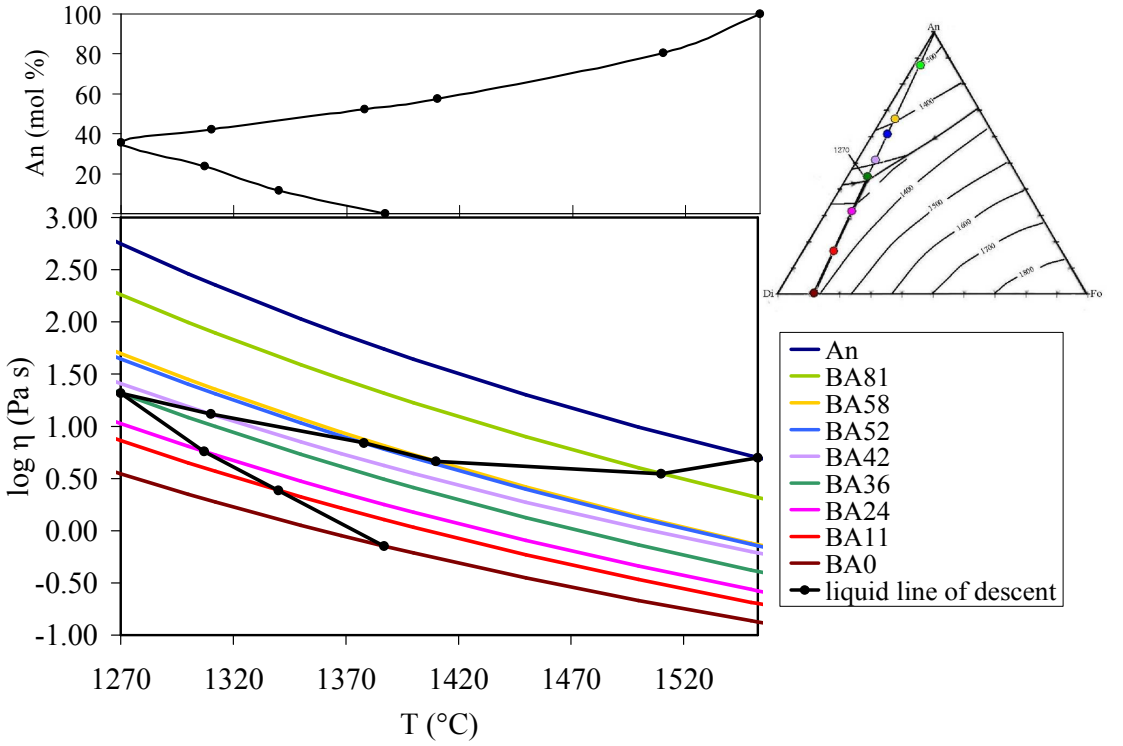

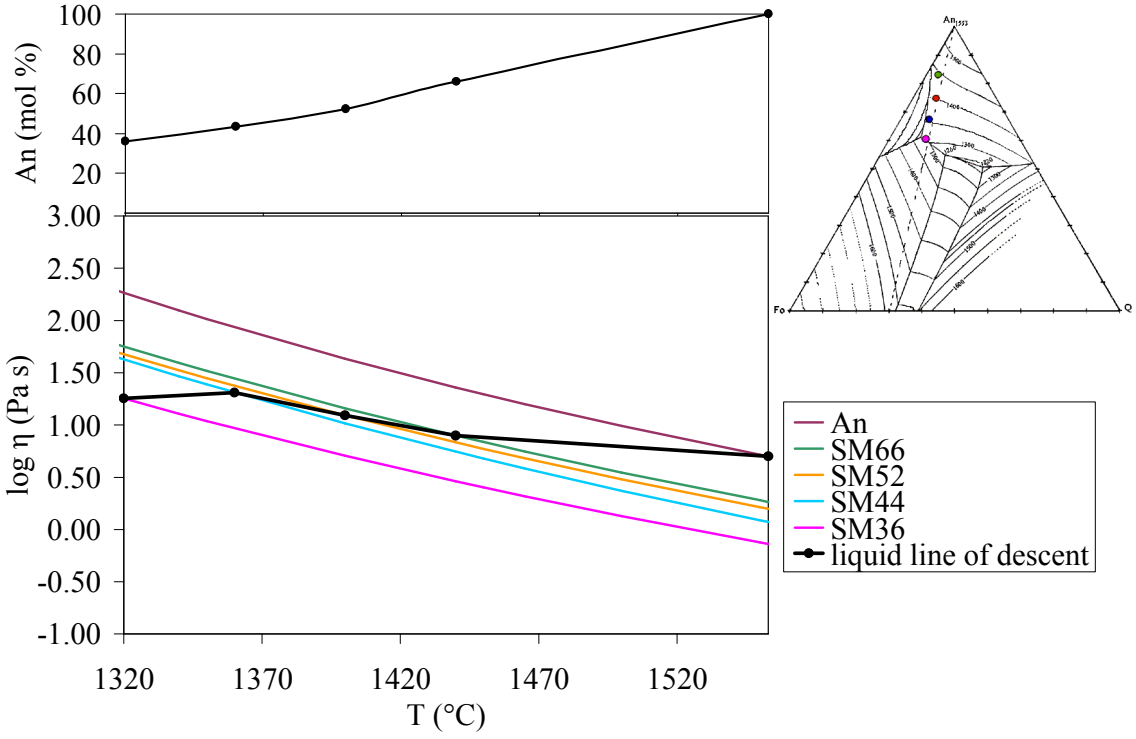

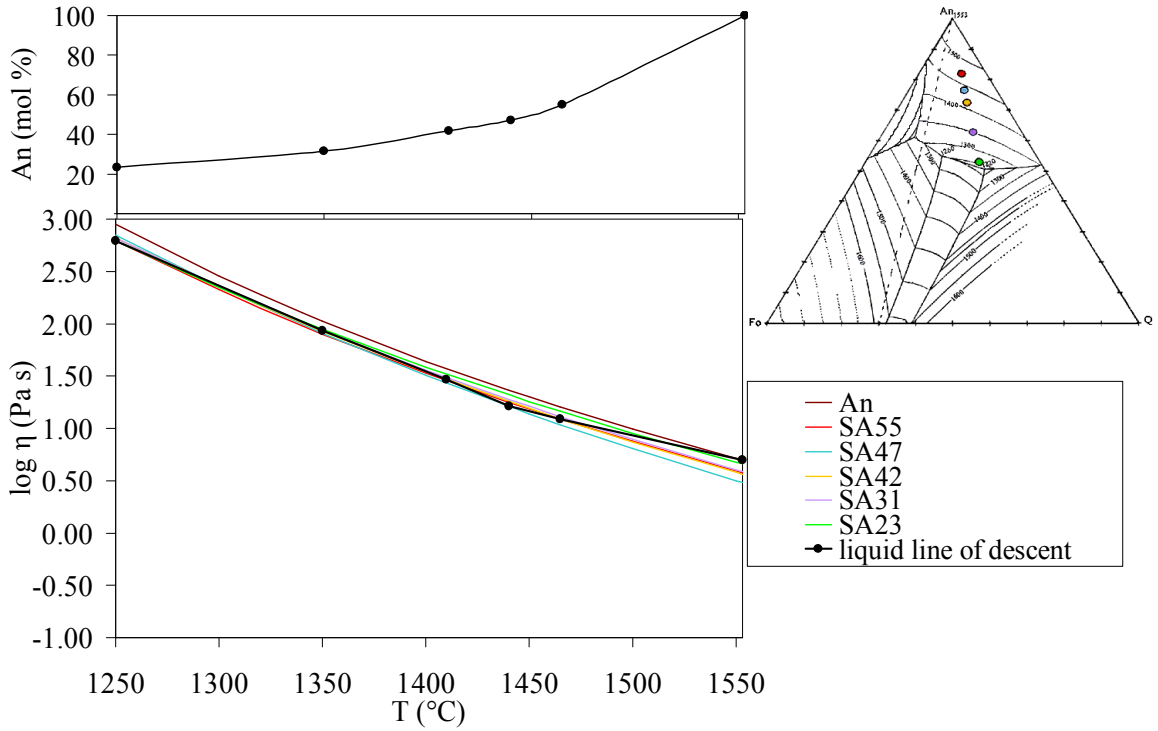

Figure 3.8. Viscosity along the liquid lines of descent of all series as a function of temperature. Also shown are the ternary diagrams (wt %) and the amount of anorthite component at each point in the liquid along the descent path (mol %).

All graphs are plotted using the derived TVF equations. The bold black line in each graph represents the viscosity along the liquid line of descent. The liquid line of descent demonstrates both the increase in viscosity with decreasing temperature and the chemical effect of crystallization as the anorthite content decreases. What is particularly interesting is the different liquid evolution patterns for each series. In all cases, as anorthite crystallizes, the melt becomes more depolymerized; however, the effect of depolymerization (tending to decrease viscosity) is competing with the effect of decreasing temperature (tending to increase viscosity) in order to determine the viscosity path along the liquid line descent. This tug-of-war between temperature and depolymerization is best demonstrated by the BA (tholeiitic basalt) series which has the

largest range in NBO/T values (Figure 3.8 a). Within the BA series there are two liquid lines of descent. One path is from anorthite and the other is along the diopside-forsterite cotectic. From BA0 the viscosity increases steeply to the eutectic as it becomes more polymerized with the crystallization of diopside and forsterite. However, from anorthite, the liquid line of descent first demonstrates a decrease in viscosity then gradually increases and finally when the melt composition approaches the eutectic composition (BA36) the viscosity again decreases. This suggests that as the first crystals form the liquid will become less viscous.

The SM series (basaltic andesites) demonstrates a small increase from anorthite to SM66 of about 0.20 log units, but again when the melt composition converges toward the eutectic composition (SM36) there is a slight drop in viscosity. In contrast, the SA series (dacites), which demonstrates the smallest variation in the degree of polymerization, increases by more than half an order of magnitude from anorthite at the same temperature and consistently increases along the path of liquid evolution.

In summary, if plagioclase is the liquidus phase, anorthite crystallization always results in depolymerization of the residual liquid. However, liquid viscosity can increase or decrease during cooling in basaltic systems (BA and SM series). Liquidus viscosity in the dacitic series (SA) always increases during cooling.

3.6 Summary

- Seventeen glasses were synthesized in three series, analogous to tholeiitic basalts, basaltic andesites, and dacites. Their compositions were checked using the electron microprobe at Washington University St. Louis.

- The viscosity of all compositions were measured using parallel plate and concentric cylinder viscometry. Liquid viscosities increase with increasing bulk polymerization (NBO/T values).
- TVF equations were generated for all compositions and compared with the measured viscosity. Using a constant *A* parameter in the TVF equation also generated good results but it was found that using variable TVF parameters gave a slightly better match to measured viscosity data.
- Two models were generated by parameterizing the TVF equation in order to predict the viscosity anywhere along a particular series. A 3rd order polynomial model functioned for only the BA series. Another model based on entropy of mixing was generated for all series, and was an excellent match to the data for the BA series. Similar models for the SA and SM series also reproduced measured data under 0.35 log units for all samples
- Finally, liquid lines of descent were analyzed for each series, demonstrating a different evolution path for each series. Because anorthite crystallization depolymerizes the residual liquid, liquid viscosity can increase or decrease during cooling in basaltic systems (BA and SM series) if plagioclase is the liquidus phase. Liquidus viscosity in the dacitic series always increases during cooling.

CHAPTER 4 – APPLICATIONS

"Learning is to a man as the leaves and branches are to a tree, and it can be said that he should simply not be without it."

–Takeda Shingen

4.1 Overview

In the previous chapter, viscosity data were presented and simple equations were determined to calculate the viscosity of liquids in the three systems as a function of anorthite content and temperature. It was found that liquid viscosity changes little for the early stages of differentiation of anorthite-rich basaltic liquids. For dacitic liquids, viscosity always increases during cooling and differentiation.

Here, predictive models are tested against the measured data from Chapter 3, in order to determine whether further research on viscosity in simple systems requires further experimental measurements. It is shown that available models do not reproduce the measured viscosity of the simple systems of this study very well, especially at the lower temperatures.

Finally, for modeling petrological processes, the viscosity of magma (liquid-crystal mixture) is usually the parameter of interest. The magma viscosity of all series is calculated assuming a closed-system behavior, where crystallization occurs in equilibrium and all crystals that formed are retained in the melt. In reality, some degree of crystal fractionation is likely to occur, so that actual magma viscosity will be between the two extremes, of total retention of crystals (equilibrium crystallization), and total removal of crystals (perfect fractional crystallization), where the magma follows the liquid line of descent. Then the chemical effect of crystallization on liquid viscosity, which controls the rate of crystal differentiation on the bulk magma, is also discussed.

4.2 Comparison with Previous Viscosity Models

The viscosity data were compared with published models of melt viscosity as a function of temperature and composition in order to 1) determine if there was a need to measure the viscosity of these liquids or whether existing models would have been accurate enough, and 2) determine which predictive model was most accurate. The four models applied to the measured liquids of this study span decades of research and include Bottinga and Weill (1972), Shaw (1972), Giordano and Dingwell (2003), and Giordano et al. (2006).

The first model tested was the earliest of the four models. Bottinga and Weill (1972) compiled 2440 viscosity data points from anhydrous multicomponent silicate liquids in order to develop a predictive model to accurately calculate the viscosity of natural magmatic liquids. From their data set they generated a list of partial molar viscosity values for the seventeen oxide components at fifty degree intervals from 1200 to 1800°C. They used a linear additive equation: $\ln\eta = \sum X_i D_i(T)$, where η is the Newtonian viscosity, X_i is the mole fraction of oxide *i*, and D_i is the experimentally derived effective partial molar viscosity for oxide *i* for a specific range of SiO_2 concentration at a specific temperature. Figure 4.1 compares the calculated viscosity derived from the Bottinga and Weill (1972) model with the measured data from this study at 1200 and 1500°C. While the Bottinga and Weill (1972) model reproduces the pattern of decreasing viscosity with increasing NBO/T for the BA and SM series, the calculated values do not match the measured viscosity very well. This model is limited because the temperature range used, fifty degree intervals from 1200-1800°C, cannot be applied to

the parallel plate data or even reliably extrapolated to that range because of the non-Arrhenian behavior of silicate liquid viscosity.

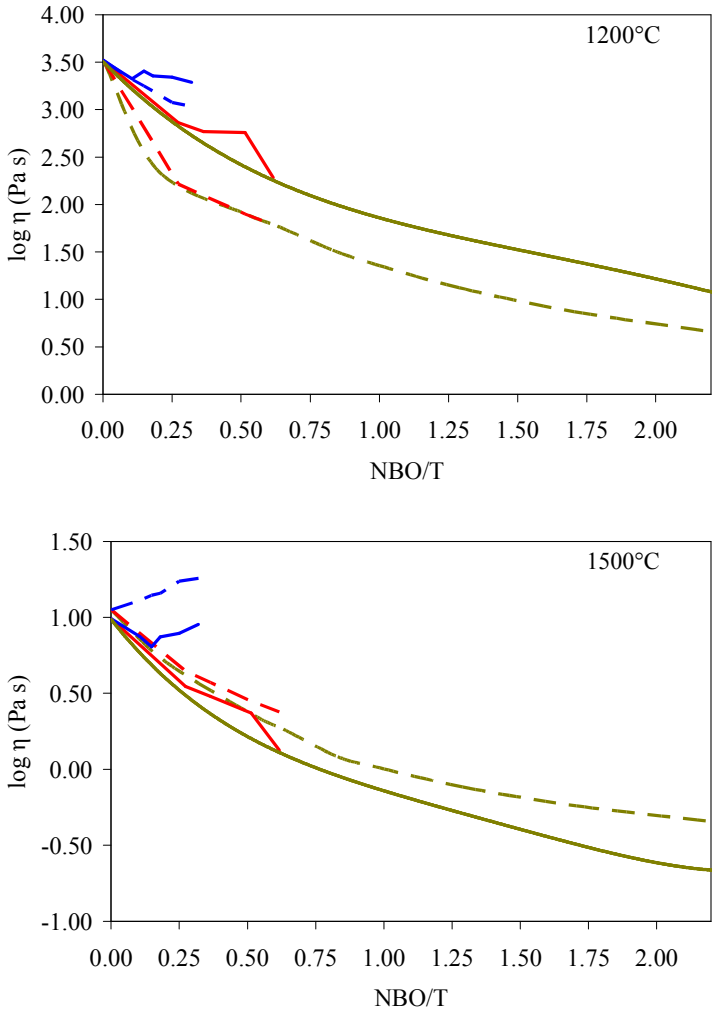

Figure 4.1. Bottinga and Weill (1972) viscosity calculation (dashed lines) compared to the TVF equations (solid lines) at 1200-1500°C for all three series. The BA series is represented by the green lines; SM is red; SA is blue.

The other commonly used model in petrological studies is that of Shaw (1972). The Shaw (1972) model is very similar to the Bottinga and Weill (1972) model, again relying on the Arrhenius relationship, but is simpler. Instead of using partial molar viscosity values of seventeen oxides, Shaw (1972) used only four partial molar coefficients of SiO_2, derived from the activation energies of SiO_2 in binary systems and the coefficients of Bottinga and Weill (1972). The Shaw (1972) model is based on the

postulate that the viscosity curves of multicomponent silicate liquids will intersect the reference curve of pure SiO_2 liquid at a specific temperature and viscosity. The points of intersections are averaged and applied to the following equation

$$\ln \eta(P) = s(10^4 / T(K)) - c_T s + c_\eta \qquad (4.1)$$

Where s is the calculated slope for a specific composition using the four partial molar coefficients and the mole fraction of SiO_2 and c_T, -6.40, and c_η, 1.50, are the average points of the intersections an the inverse temperature and ln η axes, respectively. Shaw (1972) calculated the constants c_T and c_η by examining the Arrhenius plot of viscosity data for liquid SiO_2 against a series of oxides from the Bottinga and Weill (1972) study. When compared to the data from this study, the Shaw (1972) model did not agree well. When the model is compared to our viscosity measurements at 800, 1200, and 1500°C, it is apparent that the model is particularly unreliable at lower temperatures (Figure 4.2). Shaw (1972) warns that the model should not be applied to viscosity values greater than 10^5 Pa s. At 1200 and 1500°C both measured and predicted viscosities are below this value but the disagreement frequently exceeds 0.5 log units at 1200°C and 0.3 log units at 1500°C.

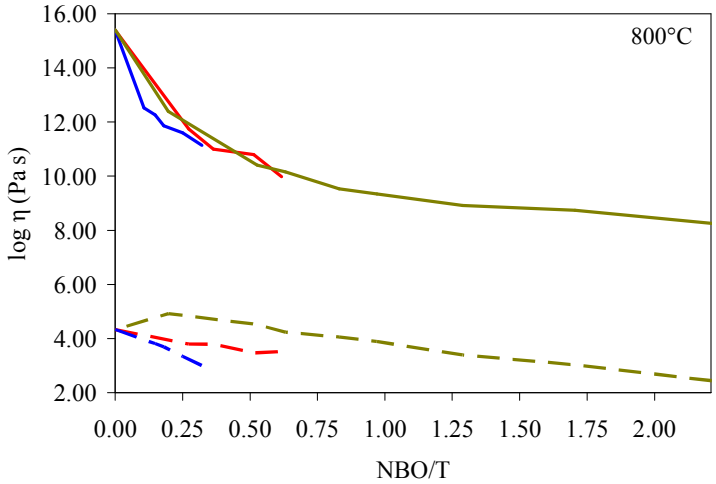

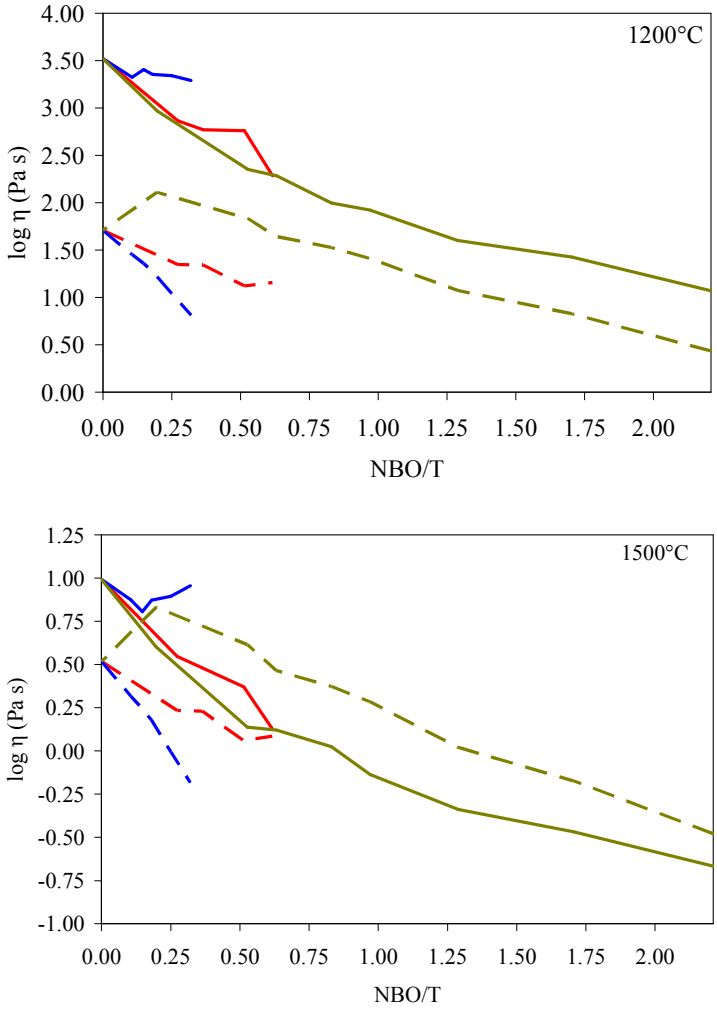

Figure 4.2. Shaw (1972) viscosity calculation (dashed curve) compared to the TVF equations (solid lines) at 800, 1200, and 1500°C for all three series. The BA series is represented by the green lines; SM is red; SA is blue.

The next model tested was the Giordano and Dingwell (2003) model. This model expands the TVF equation to develop a non-Arrhenian model for silicate melt viscosities. From 19 natural multicomponent melts analyzed via concentric cylinder, parallel plate, and micropenetration methods, spanning a viscosity range of 10^0-10^{12} Pa s, Giordano and Dingwell developed two sets of equations to determine the viscosity at a given temperature. The first is based on the NBO/T of the melt and the second uses its own empirical parameter referred to as the structure modifier content (SM), which is the mole

% sum of the oxides of CaO, MgO, MnO, $FeO_{tot}/2$, Na_2O, and K_2O. The NBO/T method uses a series of equations listed below (Equations 4.2-5), where temperature is in Celsius. One useful aspect of this model is that viscosity can be calculated for any temperature and is not limited to specific intervals like the Bottinga and Weill (1972) calculation.

$$\log \eta = a_1 \ln(NBO/T - a_2) + a_3 \qquad (4.2)$$

$$a_1 = -0.15139 - \frac{1129.19}{T} - \frac{1381914}{T^2} + \frac{1290000000}{T^3} \qquad (4.3)$$

$$a_2 = -0.00071 - \frac{3.47074}{T} + \frac{5720.781}{T^2} - \frac{2061030}{T^3} \qquad (4.4)$$

$$a_3 = -5.44516 + \frac{9309.88}{T} - \frac{3390935}{T^2} + \frac{3144300695}{T^3} \qquad (4.5)$$

The graphs below (Figure 4.3) compare the predicted viscosity with that obtained from the experimentally determined TVF equations at 800 and 1500°C. Again the model demonstrates the relationship between NBO/T and viscosity but the calculated viscosities do not agree well with the measured data. This is true in all cases but the most depolymerized samples of the BA series at the higher temperatures; in this case there is very good agreement.

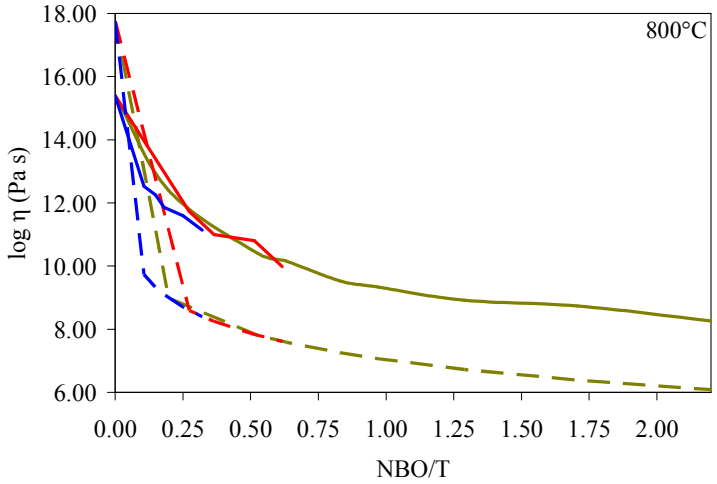

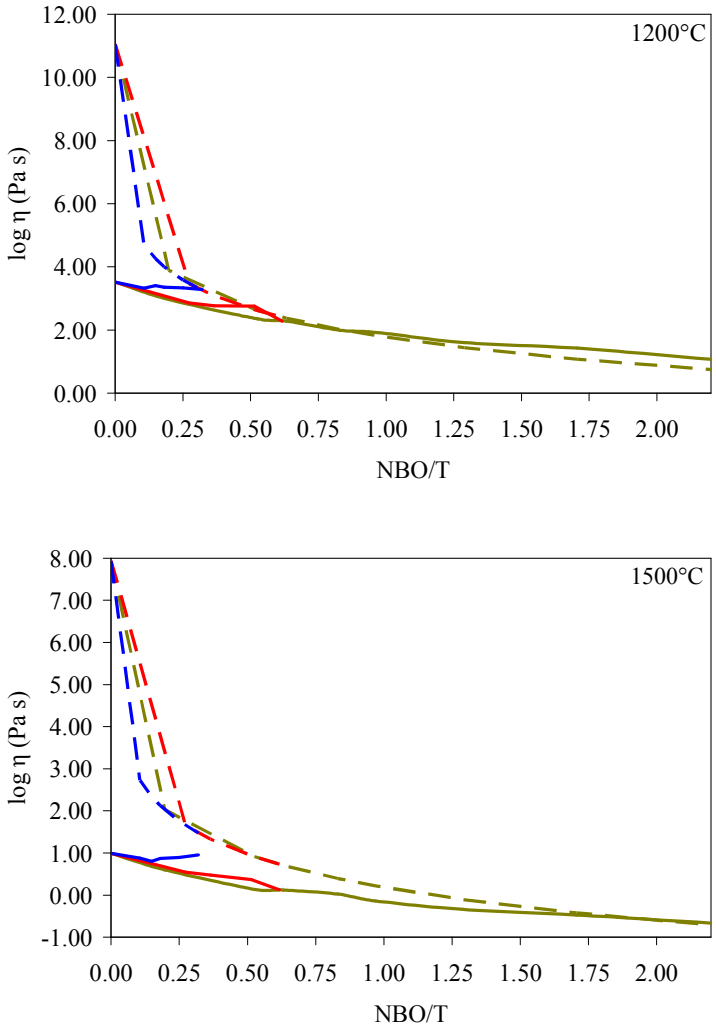

Figure 4.3. Giordano and Dingwell (2003) NBO/T calculation (dashed lines) at 800, 1200, and 1500°C. The BA series is represent by the green lines; SM is red; SA is blue.

For Giordano and Dingwell's (2003) second model, the structure modifier content constant for the measured CMAS compositions is simply the mole percent sum of CaO and MgO. The structure modifier was then applied to the following equation (Equation 4.6).

$$\log_{10} \eta\,(Pa\,s) = c_1 + \frac{c_2 c_3}{c_3 + SM} \qquad (4.6)$$

The temperature-dependent parameters c_1, c_2, and c_3 variables were determined by Giordano and Dingwell (2003) from an extensive data set (Equations 4.7-4.9).

$$c_1 = \frac{-17.80106 + 0.01808103T}{1 - .0022869T} \tag{4.7}$$

$$c_2 = [0.02532 + 2.5124\exp(-.0063679T) + .0000404562T]^{-1} \tag{4.8}$$

$$c_3 = \frac{1 - .0016569T}{0.017954 - .00006390597T} \tag{4.9}$$

where T is in °C. The graphs below compare the structure modifier model with the measured viscosities of CMAS glasses at 800, 1200, and 1500°C. Since this model is dependent on the amount of structure modifier at a given temperature there is only one calculated model for each temperature. The agreement is good (within approximately 0.2 log units) at 1500°C, not as good at 1200°C (± 0.5 log units), and quite poor at 800°C.

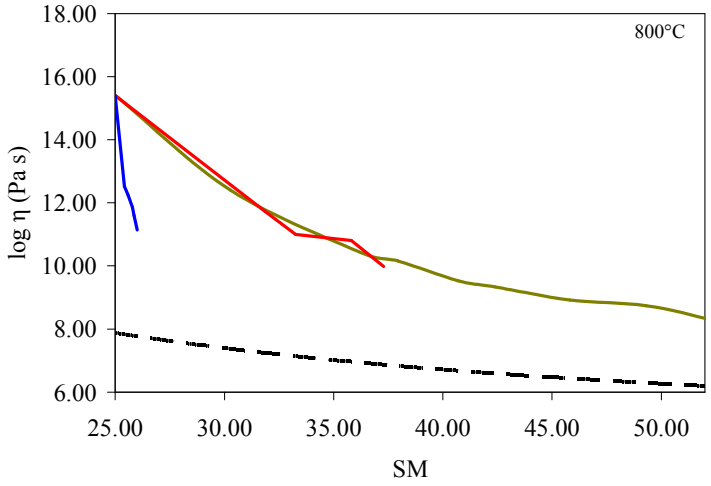

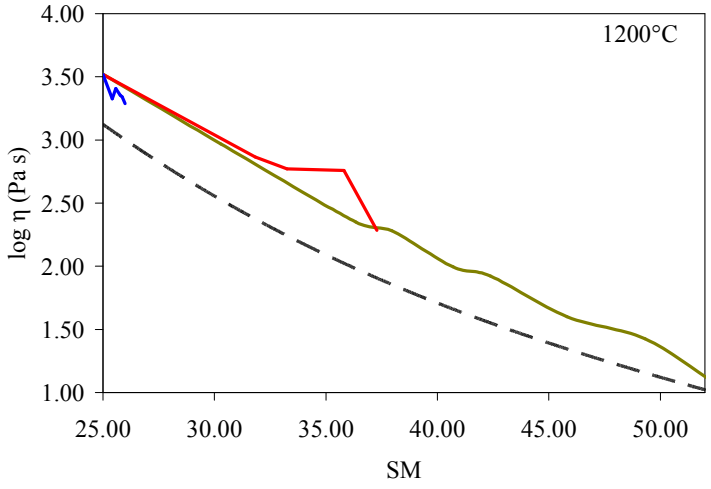

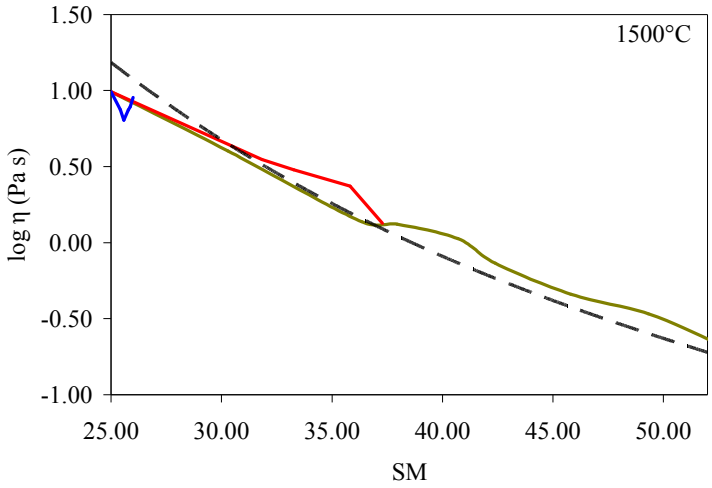

Figure 4.4. Giordano and Dingwell (2003) structure modifier content model (dashed lines) at 800, 1200, and 1500°C. The BA series is represented by the green lines; SM is red; SA is blue.

The final model tested in this study was by Giordano et al. (2006), which expands the Giordano and Dingwell (2003) model. The new model uses an expanded dataset to recalibrate the previous Giordano and Dingwell (2003) structure modifier model, which resulted in the following equations, where T is °C:

$$\log \eta = b_1 + \frac{b_2 b_3}{b_3 + SM} + b_4 \qquad (4.10)$$

$$b_1 = \frac{-33.5556 + 0.0351623T}{1 - 0.0022362T - 0.00000166697T^2} \qquad (4.11)$$

$$b_2 = \frac{-93.6494 + 0.2317411T}{1 - 0.0054597T + 0.00001361072T^2} \qquad (4.12)$$

$$b_3 = \frac{45.5755 + 0.0780935T}{1 - 0.0036108T - 0.00000002170T^2} \qquad (4.13)$$

$$b_4 = -0.00001292391\left(\frac{AE}{SM}\right)T^2 + 0.03577545\left(\frac{AE}{SM}\right)T - 24.3366274\left(\frac{AE}{SM}\right) \qquad (4.14)$$

This new model is very similar to the 2003 Giordano and Dingwell model except for the addition of b_4, which accounts for the alkali excess over the alumina content

(AE=$Na_2O+K_2O-Al_2O_3$). They found that the 2003 model overestimated the viscosity of peralkaline melts and underestimated the viscosity of peraluminous melts. To account for this, the new model then calculates the viscosity based on different amounts of excess alkali (AE) and the amount of structural modifiers (SM). This model was applied to the compositions of this study; however, since these are only CMAS glasses the b_4 variable is always zero because the syntheses do not contain alkalis. Although the Giordano et al. (2006) model uses a larger dataset, the calculated values were similar (Figure 4.5).

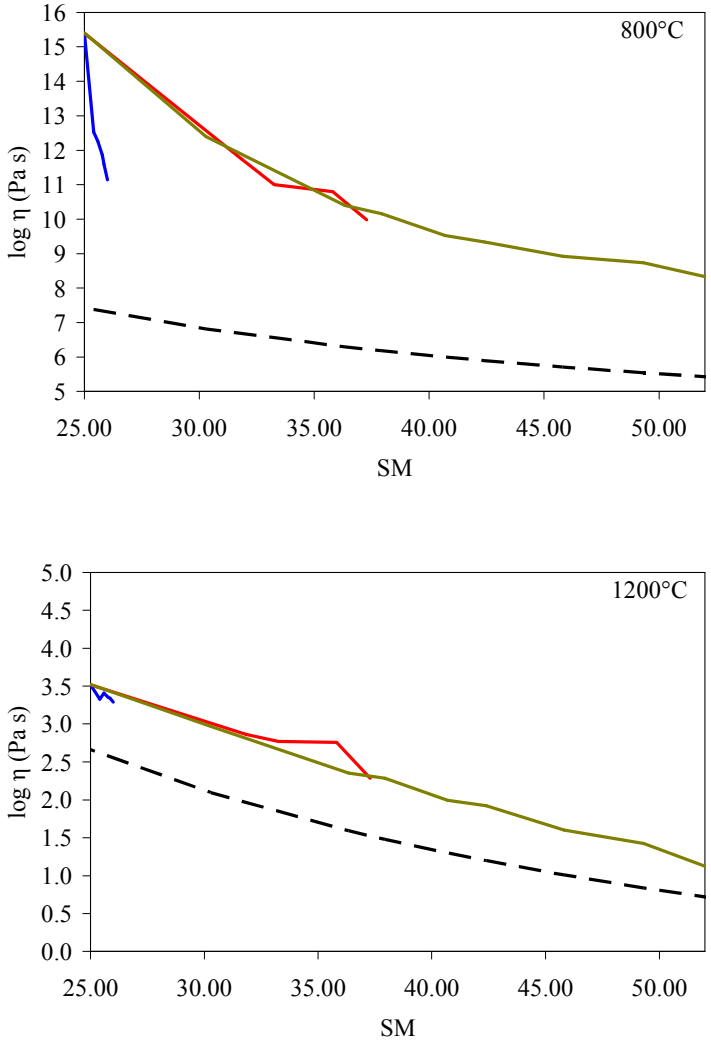

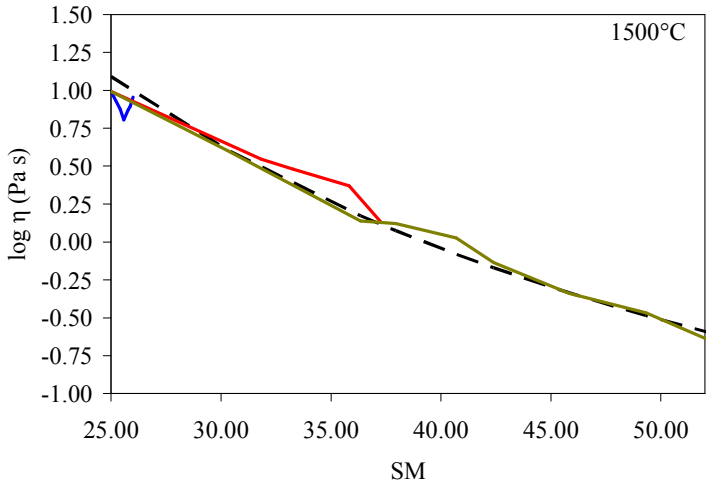

Figure 4.5. Giordano et al. (2006) SM calculation (dashed line) at 800, 1200, and 1500°C. The BA series is represented by the green lines; SM is red; SA is blue.

Overall, comparing the model predictions to data for the synthetic glasses indicates that currently available models do not adequately reproduce the viscosity of simple systems. For example, none of the models tested were able to predict the crossover found at high temperatures for the SA series. The inaccuracy of the models, particularly at the lower temperatures, suggests that more viscosity measurements are needed to develop better viscosity models. For this type of simple system analysis, experimentally obtained measurements are imperative for an accurate description of liquid viscosity.

4.3 Magma Viscosity

As described in Chapter 1 the physical effect of crystals on the viscosity of a melt and crystal mix can be calculated using the Einstein-Roscoe equation (Equation 4.15).

$$\eta = \eta_0 (1 - R\phi)^{-2.5} \qquad (4.15)$$

where η_0 is the viscosity of the liquid, ϕ represents the volume fraction of solids in suspension, and R is a constant that represents the volumetric ratio of solids at maximum

packing (McBirney and Murase 1984). The most commonly used value for R is 1.67, which was found to be the most accurate for lavas by Marsh (1981) and is used for the following calculations.

In order to calculate the volume fraction of crystals in each of the melts as the temperature decreases and the sample drops below its liquidus temperature, the lever rule was used to determine the amount of each phase at a given temperature. The volume and density for each liquid composition was calculated at each temperature using the following equations (Lange and Carmichael 1987):

$$V_{liq}(T) = \sum X_i \left[V_{i,T_{ref}} + \frac{dV_i}{dT}\left(T - T_{ref}\right) \right] \qquad (4.16)$$

$$\rho_{liq}(T) = \frac{\sum X_i (M.W.)}{V_{liq}(T)} \qquad (4.17)$$

where V_{liq}(T) is the molar volume of the melt at temperature T (K), X_i is mole fraction of each oxide component, V_i is the partial molar volume of each oxide component, dV_i/dT is the temperature derivative of V_i, and T_{ref} (K) is the reference temperature. The liquid density is the sum of the mole fraction of each oxide multiplied by its molecular weight, divided by the calculated volume at a given temperature. The volume and density for anorthite crystals at a given temperature, as well as forsterite and diopside crystals for part of the BA series, were calculated using data from Fei (1995) and Smyth and McCormick (1995). From this information the volume fraction of crystals can be calculated (Equation 4.18).

$$\phi = \frac{\dfrac{M_{An}(wt\%)}{\rho_{An}}}{\left(\dfrac{M_{An}(wt\%)}{\rho_{An}} + \dfrac{M_{liq}(wt\%)}{\rho_{liq}} \right)} \qquad (4.18)$$

The viscosity of the magma can now be calculated at any temperature using the TVF curves of the liquids and the volume fraction of crystals determined from the phase diagram.

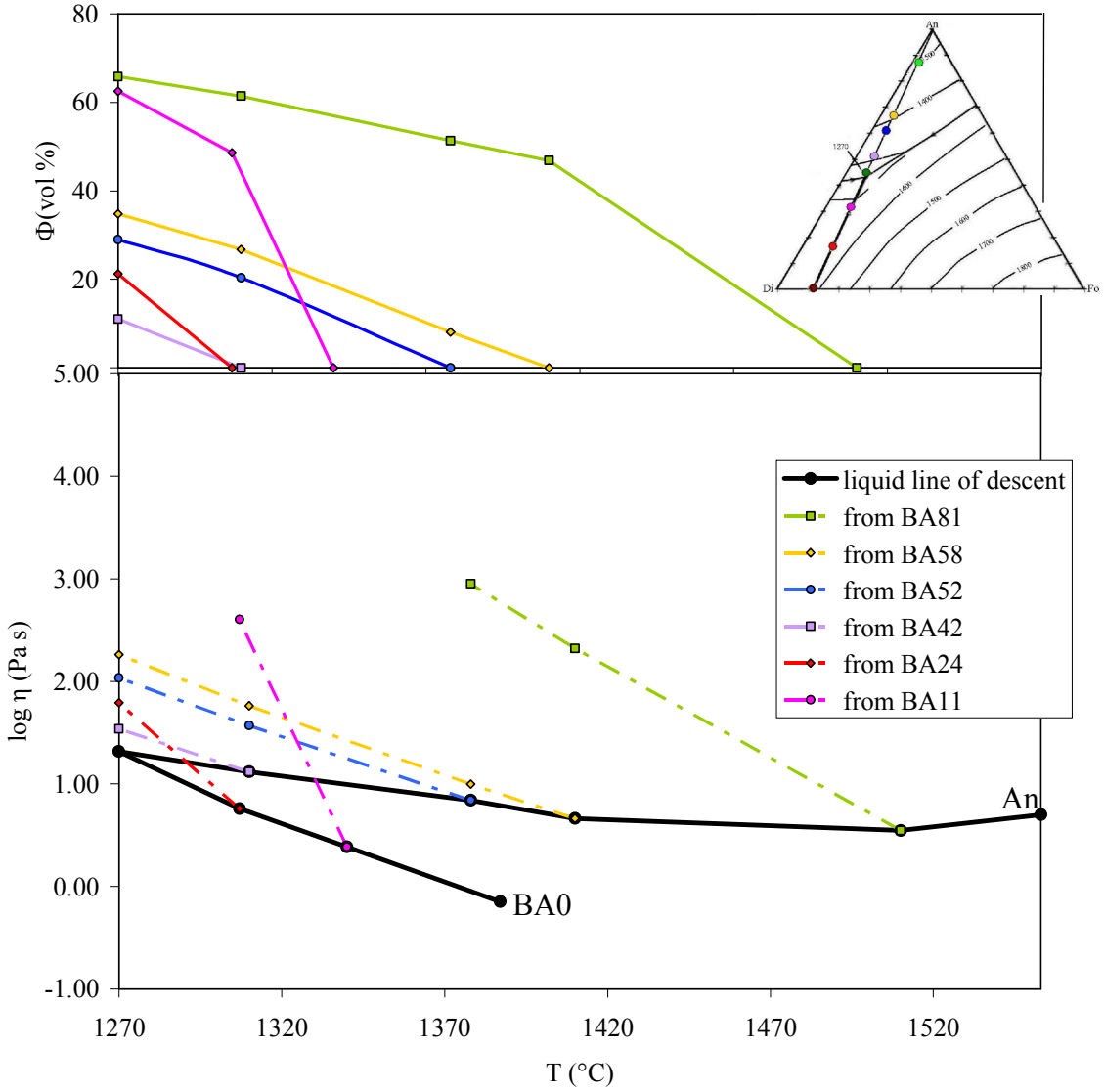

Figure 4.6. Magma viscosity for BA calculated using the Einstein-Roscoe equation.

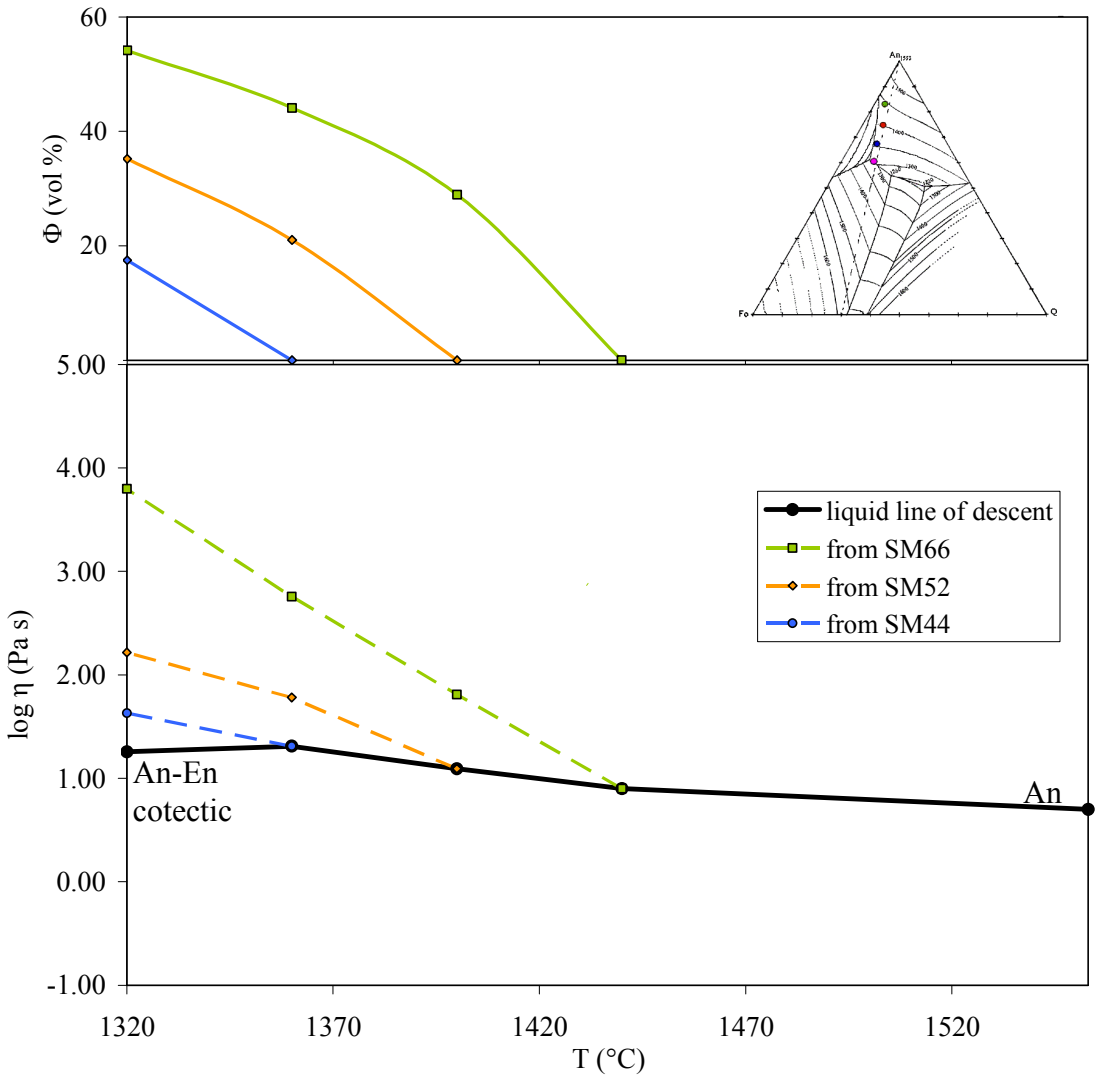

Figure 4.7. Magma viscosity for SM series calculated using the Einstein-Roscoe Equation.

Figures 4.6-8 present an opportunity to examine both the physical and chemical effects of crystallization. The chemical effect of crystallization on the melt viscosity can be seen in the liquid line of descent, shown as the bold black line on all graphs below; the physical effect is represented by dashed lines of the calculated values of magma viscosity. The magma viscosity is calculated for the bulk composition sample, in order to observe the corresponding viscosity change for each composition accompanying cooling and progressive crystallization.

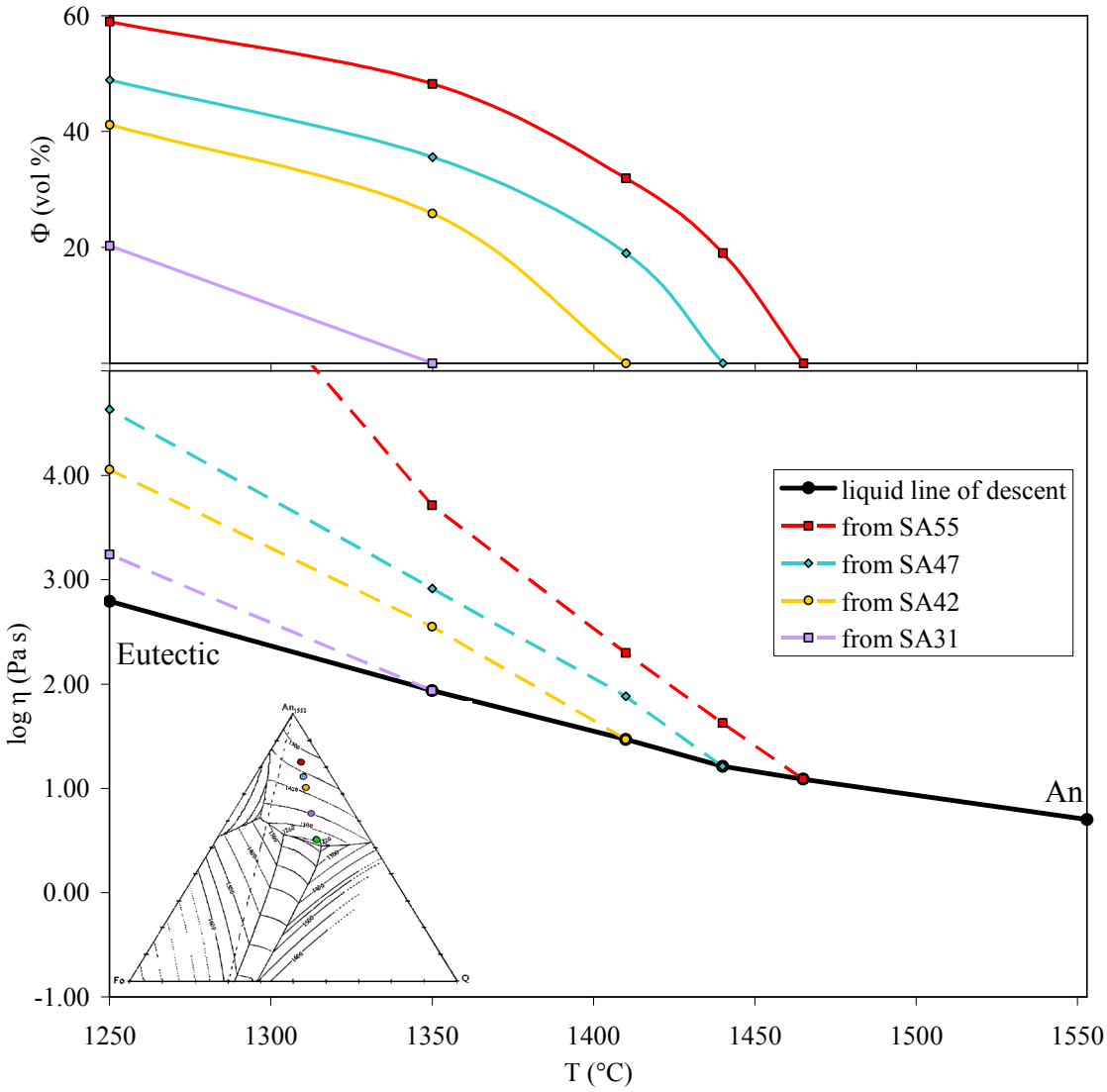

Figure 4.8. Magma viscosity for SA series calculated with the Einstein-Roscoe equation.

These figures demonstrate the drastic physical impact crystals can have on magma viscosity. However, during progressive cooling and plagioclase crystallization, magma viscosity in basaltic systems could initially decrease slightly, as changing liquid composition outweighs decreasing temperature and increasing crystal content. But with further cooling, magma viscosity will always increase as the physical effect of the entrained crystals begins to dominate.

It is also important to know at what point along the liquid line of descent the magma starts at. For example, in the BA series what is the viscosity at 1270°C? If a lava of composition BA42 comes out of the vent at 1310°C, it is at its liquidus temperature. As it cools and equilibrium crystallization occurs, the viscosity of the magma would be $10^{1.54}$ Pa s at 1270°C. If, however, the bulk composition was BA58 it would already contain crystals when erupted at 1310°C, and by 1270°C would have more crystals and a viscosity of $10^{2.26}$ Pa s. If the bulk composition was BA81 at 1270°C it would contain more than 40 volume % crystals.

4.4 Implications for Petrological Processes

Previous research on petrological processes places great importance on viscosity; however, in order to describe the processes in question they tend to oversimplify the effect of crystals. These previous studies assume the effect of crystals can be represented with a constant, assume their effect is negligible, or use outdated viscosity prediction models. Some examples of models that oversimplify magma viscosity are described next.

The FLOWGO model (Harris and Rowland 2001) was developed as a kinematic, self-adaptive, numerical model that predicts the growth of channelized lava flows. However, the FLOWGO model uses viscosity methodology dating back to Shaw (1972). Barmin et al. (2003) studied lava dome magma discharged through a conduit. This model treated the magma as a Newtonian liquid with a viscosity dependent on the volume fraction of crystals, but did not include the compositional change of liquid viscosity due to crystal generation. Gonnermann and Manga (2003) researched magma fragmentation during explosive volcanism. Their model developed for viscosity accounts for strain rate

and volatile content but they assume that the effect of crystal growth is represented by a simple increase in viscosity due to the physical effects of inclusions. This assumption does not account for the change in the liquid composition over time. This assumption may lead to incorrect estimates of the depth of magma fragmentation. McBirney and Murase (1984) reviewed the rheological properties of magmas, specifically on the interaction in the area between the liquidus and the solidus, and stated that "few fields of geological research hold greater potential for enhancing our understanding of basic magmatic and tectonic processes." The models mentioned above provide a good theoretical foundation but would greatly benefit from a more rigorous treatment of viscosity, and should include the chemical effect of progressive crystallization on melt composition.

The chemical effect of crystallization on viscosity can have a large effect on the igneous processes such as the ascent of a magma in a conduit. As a magma ascends it can change its composition by differentiation or maintain a constant bulk composition while partitioning itself into different phases. Fractional crystallization is a primary way a magma can differentiate, which was previously discussed in Chapter 3. These compositional changes result in changes of the viscosity along the liquid line of descent, which in some cases, may result in the liquid maintaining near-constant viscosity or even becoming less viscous as crystallization occurs. The evolving liquid viscosity can affect the behavior of a magma body. The two processes discussed in more detail below are crystal settling and magma ascent.

4.4.1 Crystal Settling

Crystal settling, commonly referred to as gravity settling, is a mechanism that can fractionate crystals from a melt. Settling in conjunction with the chemical effect of crystallization can thus reduce the viscosity of a melt below the original pre-crystallization viscosity or completely alter the viscosity path. The rate of crystal settling itself depends on liquid viscosity, and hence the chemical change caused by crystallization. To calculate the terminal settling velocity of a crystal, Stokes' Law is used (Equation 4.19).

$$V = \frac{2gr^2(\rho_s - \rho_l)}{9\eta} \qquad (4.19)$$

where V is the settling velocity, g is gravity, r is the radius of the crystal, ρ_s is the density of the crystal, ρ_l is the density of the liquid, and η is the viscosity of the liquid. Any increase in viscosity will slow the rate of crystal settling while a viscosity decrease results in more efficient crystal removal.

For example, if the magma viscosity for SM (Figure 4.7) is reexamined the varying settling rate along a series can be quantified. Between liquid SM44 at 1360°C and SM36 at 1320°C there is a small drop in viscosity which will increase the settling velocity of crystals. A 0.1 cm (r) plagioclase crystal settling in SM44 liquid at 1360°C it has a terminal settling velocity of 1.06×10^{-3} cm/s, compared to 1.13×10^{-3} cm/s at 1320°C for the SM36 liquid. If crystals separate faster from the melt, this will result in the magma viscosity and bulk composition staying closer to the liquid viscosity and liquidus composition. Therefore, bulk magma viscosity may also stay nearly constant or even decrease slightly in basaltic systems during the early stages of cooling and crystallization.

In dacitic systems, such as the SA series, the viscosity always increases along the liquid line of descent so a similar increase in terminal settling velocity would not be possible.

4.4.2 Magma Ascent Rate

The speed of magma ascent is inversely proportional to its viscosity. The average velocity of an ascending magma in a dike can be calculated using the following equation

$$V_{ave} = \frac{g\Delta\rho w^2}{12\eta} \qquad (4.20)$$

where g is gravity, $\Delta\rho$ is the density difference between the magma and the country rock, w is the width of the dike, and η is the viscosity of the magma (Petford et al. 1994). As with crystal settling, the ascent rate will increase with decreasing viscosity. Perhaps the largest assumption made in this study is in regard to equilibrium crystallization. Using phase diagrams to deduce the amount of crystals given at a specific temperature and composition results in assuming thermodynamic equilibrium which is not necessarily the case. In nature, some undercooling is required for crystallization to occur. If ascent and cooling are rapid, the system will not attain or maintain equilibrium. Evidence for this is presented in the form of glass either in the matrix (e.g. many basalts) or in some cases the whole-rock (e.g. obsidian). In Table 4.1 the two extreme cases of magma viscosity are demonstrated: first, total retention of crystals (equilibrium crystallization), and second complete crystal removal (perfect fractional crystallization). The difference between these two end-members is calculated in the column on the right (for reference see Figures 4.6-8).

Table 4.1 Difference between magma viscosity and liquid line of descent.

Liquidus T (°C)	Original Liquid η log (Pa s)	Liquidus Composition	Liquid η log (Pa s)	Magma η log (Pa s)	η Difference log (Pa s)
BA58					
1410	0.66	BA58	0.66	0.66	0.00
1378	0.87	BA52	0.84	1.00	0.16
1310	1.37	BA42	1.12	1.76	0.64
1270	1.61	BA36	1.32	2.26	0.94
SM52					
1400	1.09	SM52	1.09	1.09	0.00
1360	1.37	SM44	1.31	1.78	0.47
1320	1.68	SM36	1.26	2.22	0.96
SA47					
1440	1.21	SA47	1.21	1.21	0.00
1410	1.43	SA42	1.47	1.88	0.41
1350	1.91	SA31	1.94	2.91	0.98
1250	2.85	SA23	2.79	4.63	1.84

If a magma of composition BA58 retains all of its crystals until the eutectic point at 1270°C (liquidus composition BA36) the viscosity will be $10^{2.26}$ Pa s; however, if the magma retains none of the crystals it will follow the path of liquid descent and have a viscosity of $10^{1.32}$ Pa s. This results in a difference of approximately one order of magnitude in calculated magma viscosity and ascent rate. Similar effects can be seen for the SM series (Table 4.1). For the SA series a more drastic effect can be seen. At 1250°C the magma viscosity for bulk composition SA47 is $10^{4.63}$ (Pa s). The melt viscosity at the same temperature is $10^{2.79}$ (Pa s). This results in close to two orders of magnitude difference between the viscosities and hence also in calculated magma ascent rates. Crystallization will have a large effect on the ascent of a magma through a conduit particularly at the lower temperatures found in nature for intermediate to silicic magmas where the viscosity will be much greater than obtained here in the CMAS system.

4.4.3 Viscosity Paths

Depending on how a magma differentiates, the resulting magma viscosity could follow one of several different paths. The viscosity for a given starting composition can evolve in four possible ways; (i) if crystallization is impeded the magma viscosity will be the same as the viscosity of the liquid of the original bulk composition, (ii) if perfect fractionation occurs the melt will proceed along the liquid line of descent, (iii) if crystals form but are retained in the melt (equilibrium crystallization) the viscosity path will be described by the liquid line of descent modified by Einstein-Roscoe equation, or (iv) depending on the conditions imposed on the magma body it could be a combination of all three of the above patterns (Figures 4.10-12). The different lines in Figures 4.10-12, are first described in the diagram below (Figure 4.9). The first three are possibilities from the beginning composition (a) describes the liquid composition (no crystallization), (b) is the liquid line of descent (perfect fractionation), (c) represents the magma viscosity (equilibrium crystallization), and (d) is an impossible composition of the original bulk composition with crystals and ignoring the chemical effect of crystallization.

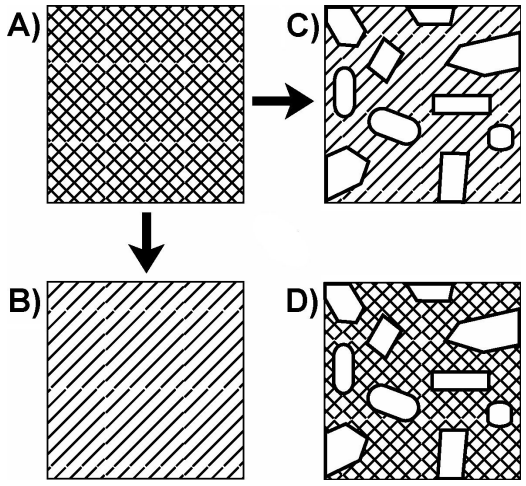

Figure 4.9. (a) liquid; (b) fractionated liquid; (c) equilibrium crystallization; (d) original liquid plus crystals (violates conservation of matter).

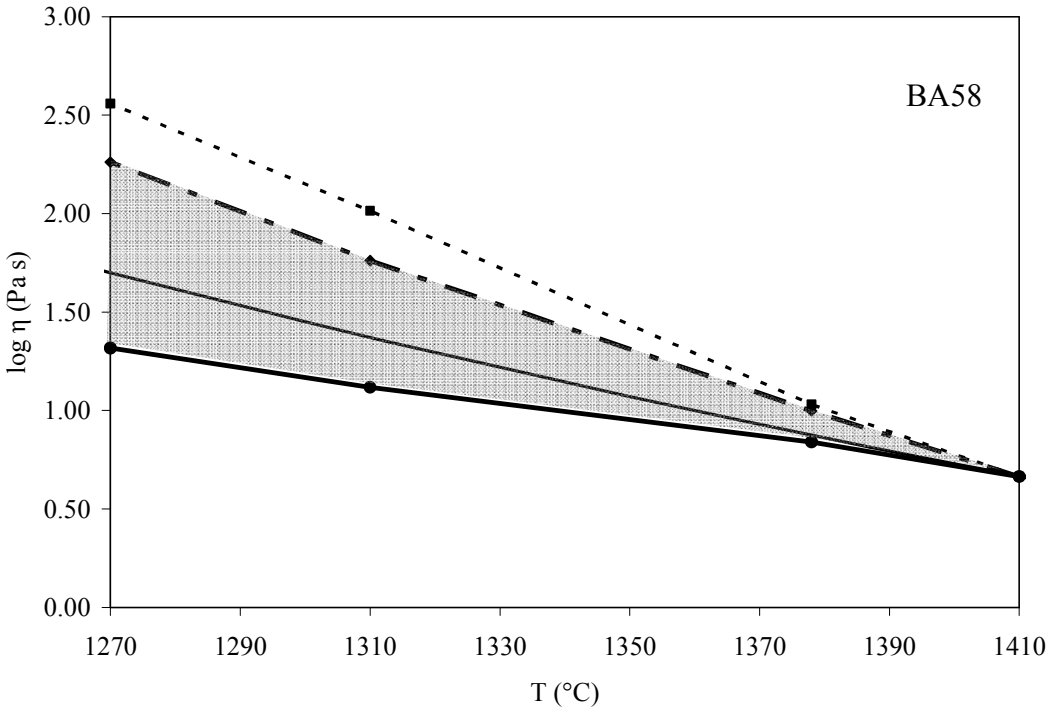

Figure 4.10. BA58 demonstrating the different viscosity paths: (a) BA58 liquid (thin black line); (b) liquid line of descent (bold black line); (c) magma viscosity with a changing liquid composition (bold dashed line); (d) BA58 liquid including the physical effect of crystals (thin dashed lines). The shaded area represents the possible range of viscosity.

Figures 4.10, 4.11, and 4.12 show possible viscosity paths for one specific composition from each of the three different series. For the SM and SA series the compositions selected are the closest to the bulk rock analyses for Santa Maria basaltic andesites and Santiaguito dacites, respectively. Also plotted is the magma viscosity assuming a constant liquid composition but including the effects of crystals. This is only a reasonable model for eutectic compositions, but it has been applied to non-eutectic compositions in the literature. Here we examine how this erroneous simplification affects calculated magma viscosity.

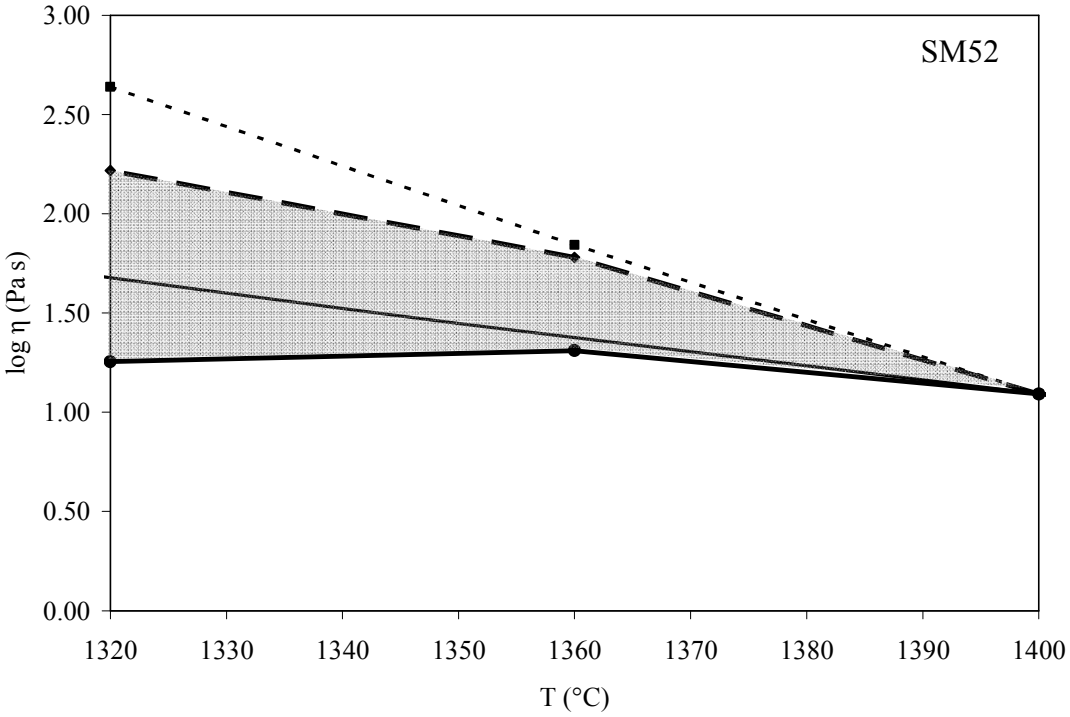

Figure 4.11. SM52 demonstrating the different viscosity paths: (a) SM52 liquid (thin black line); (b) liquid line of descent (bold black line); (c) magma viscosity with a changing liquid composition (bold dashed line); (d) SM52 liquid including the physical effect of crystals (thin dashed lines). The shaded area represents the possible range of viscosity.

The viscosity paths of the compositions are very different for each series. If liquid viscosity changes little as a function of composition within a series, as seen for the SA series, the difference between the liquid line of descent and the original liquid viscosity is negligible. Magma viscosity assuming perfect crystal retention is also the same, whether changing liquid composition is accounted for or not. The greatest difference in viscosity paths would be seen if the crystals would completely settle from the melt, which would rapidly cause a decrease in the viscosity path before more crystals begin to form. If there is a significant range of viscosity as a function of composition, as seen in the SM series, the pattern of the viscosity path would be very different from the original composition's viscosity curve. The larger the viscosity range within each series, the greater the error

resulting from ignoring the chemical effect of crystallization on residual liquid composition.

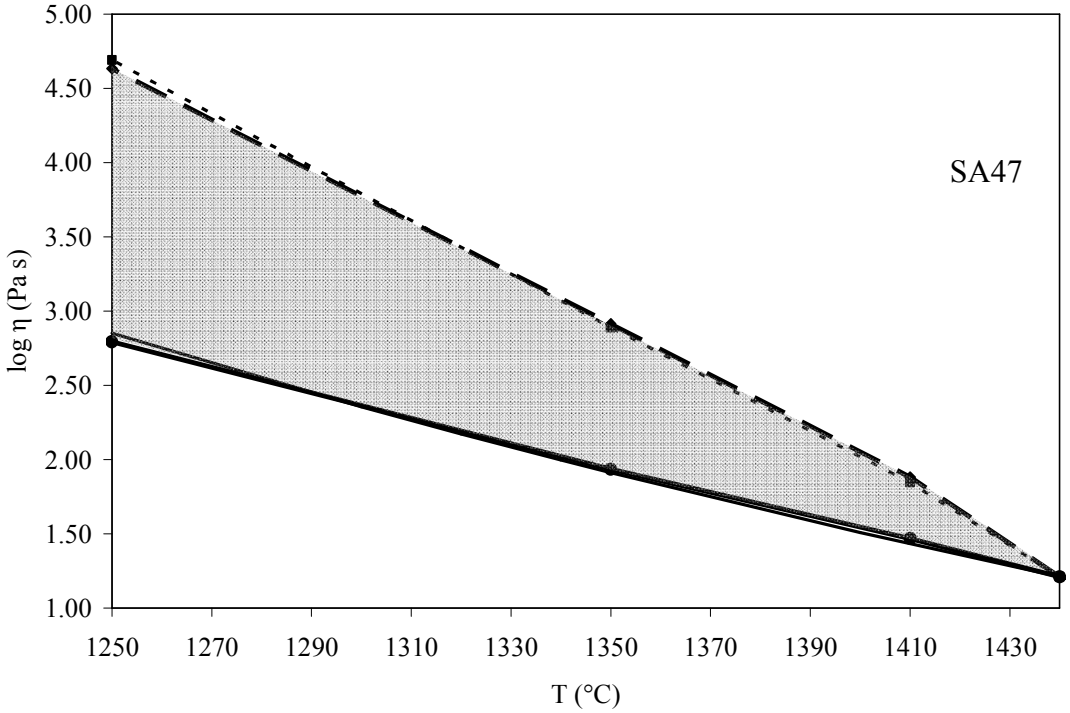

Figure 4.12. SA47 demonstrating the different viscosity paths: (a) SA47 liquid (thin black line); (b) liquid line of descent (bold black line); (c) magma viscosity with a changing liquid composition (bold dashed line); (d) SA47 liquid including the physical effect of crystals (thin dashed lines). The shaded area represents the possible range of viscosity.

In a real geologic setting, magma viscosity is more complicated than can be illustrated here using simple CMAS compositions. However, it is very beneficial to analyze these simple systems to identify what possible "options" a magma would have in nature because the phase diagrams are simple and experimentally verified. Depending on the thermal history of the magma, the magma viscosity could oscillate between the different paths described in Figures 4.9-11. Natural magmas mostly occur at lower temperatures than considered above, which would result in greater viscosity ranges for different paths because the viscosities of different silicate liquids diverge at lower

temperatures. It is imperative to understand that magma viscosity can increase, stay the same, or even decrease slightly during crystallization, depending on crystal retention. Broadly stating that crystals increase viscosity oversimplifies and devalues the importance the chemical effect can have on the melt viscosity and the overall behavior of the magma.

4.5 Concluding Remarks

In the preceding work a few factors that could greatly affect crystallization and viscosity are not discussed but also not forgotten. The factors include rate of crystal nucleation and growth, enthalpy of crystallization, introduction of volatiles, and changes in pressure. Crystal nucleation, growth, and growth rate could have a large effect on the viscosity of a magma. Poor or total lack of crystal nucleation could cause the viscosity path to follow the TVF curve and either quenching to a glass, or rapid disequilibrium crystallization, essentially skipping the intermediate magma mush stages.

Enthalpy is the description of the heat content of a system. As crystals form they release a latent heat as they change phase. Due to this latent heat the system would not cool as rapidly. Volatiles can have a large affect on viscosity, particularly the addition of water. Water will cause a decrease in viscosity, for example in a pure SiO_2 liquid near its glass transition temperature 0.1 wt % water will cause a 10-fold decrease in the viscosity (Hetherington et al. 1964). Finally, pressure could change how and when a melt crystallizes. The phase diagrams analyzed in this study are for thermodynamic equilibrium at 1 atmosphere, any pressure change would significantly alter this equilibrium thus changing the viscosity paths. A sudden decrease in pressure, for

example due to rapid ascent, could result in decompression melting and possibly superheating, again resulting in different viscosity paths.

Future paths for this research would include (i) extending the anorthite-forsterite-quartz series to their respective forsterite-quartz binary end-members and (ii) performing more viscosity measurements in both ternary systems with the eventual goal of achieving a reliable predictive viscosity model for these systems. The overall goal would be applying this type of analysis to include more complex compositions including synthetic glasses with more components, in particular alkalis, and natural melts, in order to apply these viscosities to natural magma crystal settling and magma ascent rates.

This work presents results that benefit many aspects of igneous petrology and volcanology. The purpose of this research was to study synthetic systems where phase equilibria were well understood but little viscosity data were available, examine the chemical effect of crystallization on liquid and magma viscosity, and demonstrate the importance of the results for physical models of igneous processes such as crystal settling, magma ascent, and eruption dynamics. Viscosity has a large impact on the formation, evolution, and emplacement of igneous rocks. Since the beginning of the sixteenth century, the number of casualties caused by pyroclastic and debris flows has exceeded 128,000 people (Fisher et al. 1997 and Dobran 2001). Volcanic activity is ever-present and imminent; consequently, understanding the factors that contribute both intrusively and extrusively to these devastating geologic wonders is important globally and in the world of igneous research.

4.6 Summary

- Currently available predictive models do not adequately predict liquid viscosity in the simple systems studied here.
- The viscosity of crystal bearing magma was calculated using the Einstein-Roscoe equation. The viscosity of a magma with entrained crystals will usually be greater than the viscosity of a melt of the same bulk composition.
- During the early stages of cooling and plagioclase crystallization in basaltic systems, magma viscosity may remain approximately constant over large temperature intervals, as changing liquid composition outweighs decreasing temperature and increasing crystal content. With further cooling, magma viscosity will always increase as the physical effect of the entrained crystals begins to dominate.
- Magma viscosity in the dacitic system An-En-Q always increases during cooling, because there is little change in liquid viscosity along the liquid line of descent.
- Igneous process such as crystal settling and magma ascent rate are heavily dependent on viscosity. For example an increase in the viscosity will decrease both rates; likewise, any change in viscosity brought on by the chemical effect of crystallization would result in a change in the rate of both of these processes.
- There are three distinct viscosity end-members that can determine viscosity paths, (i) original liquid (no crystallization), (ii) liquid line of

descent (perfect fractionation), and (iii) magma viscosity (equilibrium crystallization). Depending on the thermal history of the magma the viscosity could even jump from one path to another.

REFERENCES

Adam, G. and Gibbs, J.H. (1965) On the temperature dependence of cooperative relaxation properties in glass-forming liquids. *Journal of Chemical Physics* vol. 43, pp. 139–146.

Anderson, O. 1915. The system anorthite-forsterite silica. *American Journal of Science*, 4th series, vol. 39, pp. 407-454.

Bluth, G.J.S. and Rose, W.I., 2004. Observations of eruptive activity at Santiaguito volcano, Guatemala. *Journal of Volcanology and Geothermal Research*, vol. 136, pp. 297-302.

Bottinga, Y., Weill, D., 1972. The viscosity of magmatic silicate liquids: a model for calculation. *American Journal of Science*, vol. 272, pp. 438–475.

Bowen, N.L. 1915. The crystallization-differentiation in silicate liquids. *American Journal of Science*, vol. 39, pp.175-191.

Barmin, A., Melnik, O., and R.S.J. Sparks, 2002. Periodic behavior in lava dome eruptions, *Earth and Planetary Science Letters*, vol. 199, pp. 173-184.

Bouhifd, M.A., Richet, P., Besson, P., Roskosz, M., and I. Jannick, 2004. Redox state, microstructure and viscosity of a partially crystallized basalt melt, *Earth and Planetary Science Letters*, vol. 218, pp. 31-44.

Brookfield Engineering Labs., Inc. 2000. More solutions to sticky problems: A guide to getting more from your Brookfield Viscometer.

Conway, F.M., Diehl, J.F., Rose, W.I., and O. Matias, 1994. Age and magma flux of Santa Maria, Guatemala: Correlation of paleomagnetic waveforms with the Mono lake excursion, *Journal of Geology*, in review.

Confucius (1997), The Confucian Analects. Translated by Chichung Huang. Oxford University Press.

Cross, T. A., Iddings J.P., Pirsson, L.V., and Washington, H. S., 1902. A quantitative chemicomineralogical classification and nomenclature of igneous rocks. Journal of Geology, vol. 10, pp.555-690.

Dobran, F., 2001. Volcanic Processes: Mechanisms in Material Transport, Kluwer Academic, Plenum Publishers.

Dingwell, D.B., 1995. Relaxation in silicate melts: applications. In: Stebbins, J., McMillan, P.F., Dingwell, D.B. (Eds.), Structure, Dynamics and Properties of Silicate Melts. *Reviews in Mineralogy*, vol. 32. pp. 21–66.

Dingwell, D.B., and Webb, S.L., 1989. Structural relaxation in silicate melts and non-Newtonian melt rheology in geologic processes. *Physics and Chemistry of Minerals,* vol.16, pp. 508-516.

Eddings, D. 1998. King of the Murgos. Del Rey, Ballantine Books.

Fei, Y., 1995. Mineral Physics and Crystallography: A Handbook of Physical Constants, *AGU Reference Shelf* vol. 2, pp.29-44.

Fisher, V., Heiken, G., and Hullen, J.B. 1997. Volcanoes, Crucibles of Change. Princeton University Press, Princeton, NJ.

Francis, P. and Oppenheimer, C., 2004. Volcanoes. 2nd edition. Oxford University Press.

Fulcher, G.S., 1925. Analysis of recent measurements of the viscosityof glasses. *Journal of American Ceramic Society,* vol. 8, 339–355.

Giordano, D., Mangiacapra, A., Potuzak, M, Russell, J.K., Romano, C., Dingwell, D.B., Di Muro, A., 2006. An expanded non-Arrhenian model for silicate melt viscosity: A treatment for metaluminous, peraluminous and peralkaline liquids. *Chemical Geology*, vol. 229 pp. 42–56.

Giordano, D. and Dingwell, D.B., 2003a. Non-Arrhenian multicomponent melt viscosity: a model. *Earth and Planetary Science Letters*, vol. 208, pp. 337–349.

Gonnermann, H.M., and M. Manga, 2003. Explosive volcanism may not be an inevitable consequence of magma fragmentation, *Nature*, v. 426, pp. 432-435.

Harris, A.J.L., Flynn, L.P. and W.I. Rose, 2002. Temporal trends in lava dome extrusion at Santiaguito 1922-2000, *Bulletin of Volcanology*, vol. 65, pp. 77-89.

Harris, A.J.L., and S.K. Rowland, 2001. FLOWGO: A kinematic thermo-rheological model for lava flowing in a channel, *Bulletin of Volcanology.*, v. 63, pp. 20-24.

Hetherington G., Jack K. H., and Kennedy J.C. 1964. The viscosity of vitreous silica. *Physics and Chemistry of Glasses*, vol. 5 pp.130-136.

Kirkpatrick, R.J., 1977. Nucleation and growth of plagioclase, Makaopuhi and Alae lava lakes, Kilauea Volcano, Hawaii, *Geological Society of America Bulletin* vol. 88, pp.78-84.

Lejeune, A. M., Richet, P. (1995) Rheology of crystal-bearing silicate melts: An experimental study at high viscosities, *Journal of Geophysical Research* vol. 100, pp. 4215-4229.

Lange, R.A., and Carmichael, I.S.E., 1987. Densities of Na_2O-K_2O-CaO-MgO-FeO-Fe_2O_3-Al_2O_3-TiO_2-SiO_2 liquids: New Measurements and derived partial molar properties. *Geochimica et Cosmochimica Acta*, vol. 51, pp. 2931-2946.

Marsh, B. D., 1981. On the crystallinity, probability of occurrence, and rheology of lava and magma. *Contributions to Mineralogy and Petrology*, vol. 78, pp. 85-98.

McBirney, A.R., and T. Murase, 1984. Rheological properties of magmas, *Annual Review of Earth and Planetary Sciences*, vol. 12, pp. 337-357.

Morse, S.A. 1980. Basalts and phase diagrams. Springer-Verlag. New York.

Mysen, B.O., 1987. Magmatic silicate melts: Relations between bulk composition, structure and properties, *Geochemical Society Special Publication No. 1*, pp. 375-399.

Moynihan, C.T., 1995. Structural Relaxation and the Glass Transition. *Reviews in Mineralogy.* vol. 32, pp.1-19.

Mysen, B.O, Richet, P., 2005. Silicate glasses and melts: properties and structure. 1st ed Amsterdam; Boston: Elsevier.

Neuville, D.R., Courtial, P., Dingwell, D.B., Richet, P., 1993. Thermodynamic and rheological properties of rhyolite and andesite melts. *Contributions to Mineralogy and Petrology*, vol. 113, pp. 572–581

Neuville, D.R. and Mysen, B.O. (1996) Role of aluminium in the silicate network: In situ high-temperature study of glasses and melts on the join SiO_2-$NaAlO_2$. *Geochimica et Cosmochimica Acta*, vol. 60, pp. 1727–1737.

Neuville, D.R. and Richet, P. (1991) Viscosity and mixing in molten (Ca, Mg) pyroxenes and garnets. *Geochimica et Cosmochimica Acta*, vol. 55, pp. 1011–1019.

Petford, N., Lister J.R., Kerr, R.C., 1994. The ascent of felsic magmas in dykes. *Lithos*, vol. 32, pp. 161-168.

Richet, P., 1984. Viscosity and configurational entropy of silicate melts. *Geochimica et Cosmochimica Acta*, vol. 48, pp. 471–483.

Richet, P., Bottinga, Y., 1995. Rheology and configurational entropy of

silicate melts. In: Stebbins, J., McMillan, P.F., Dingwell, D.B. (Eds.), Structure, Dynamics and Properties of Silicate Melts. *Reviews in Mineralogy*, vol. 32. pp. 21–66.

Russell, J.K., Giordano, D., 2005. A model for silicate melt viscosity in the System $MgSi_2O_6$–$CaAl_2Si_2O_8$–$NaAlSi_3O_8$. *Geochimica et Cosmochimica Acta*, vol. 69, pp. 5333–5349.

Ryerson, F.J., Weed, H.C., A.J. Piwinshii, 1988. Rheology of subliquidus magmas 1. Picritic compositions, *Journal of Geophysical Research*, vol. 93, pp. 3421-3436.

Schmincke, H., 2004. Volcanism. Springer-Verlag Berlin Heidelberg, New York.

Shaw H.R., 1972. Viscosities of magmatic silicate liquids: an empirical method of prediction, *American Journal of Science,* vol. 272, pp. 870-893.

Shaw, H.R., Wrtight, T., L., Peck, C.L., and Okamura, R., 1968. The viscosity of basaltic magma: an analysis of field measurements in Makaopuhi lava lake, Hawaii: *American Journal Science*, vol. 266, pp. 225-264.

Shingen, T., 2000. Ideals of the Samurai: writings of Japanese warriors. Translated by W. S. Wilson, Ohara Publications, inc. Santa Clarita, California.

Smyth, J.R., and McCormick, T.C., 1995. Crystallographic Data for Minerals. A Handbook of Physical Constants, *AGU Reference Shelf 2* pp. 1-17.

Spera, F.J., 2000. Physical properties of magma. Encyclopedia of Volcanoes, Academic Press, pp. 171-190.

Tammann, G., Hesse, W., 1926. Die Abhängigkeit der Viskosität von der Temperatur bei unterkühlten Flüssigkeiten. Z. Anorg. Allg. Chem. 156, 245–257.

Tolkien, J.R.R. The Lord of the Rings, Boston: Houghton Mifflin Company, 902.

Vogel, D.H., 1921. Temperaturabhängigkeitsgesetz der Viskosität von Flüssigkeiten. Phys. Z. 22, 645–646.

Wright, T.L., and Okamura R.T., 1977. Cooling and crystallization of tholeiitic basalt, 1965. Makaopuhi lava lake, Hawaii. *USGS Professional Paper*, 1004.

APPENDIX

Original Theta Rotor Calibration Checks on 710a and 717a.

Table A-1.
710a Rotor Calibration Check[a].

T (°C)	log η (Pa s)	log η (Pa s)
Run 1		NIST TVF
1251.3	1.83	1.78
1250.2	1.81	1.79
1250.2	1.82	1.79
1115.1	2.53	2.49
1065.5	2.85	2.80
1016.1	3.20	3.15
996.5	3.36	3.31
976.7	3.52	3.47
956.9	3.69	3.64
937.1	3.89	3.82
917.3	4.10	4.01
907.5	4.20	4.11
897.5	4.34	4.21
Run 2		
1250.2	1.78	1.79
1214.3	1.96	1.96
1164.9	2.21	2.21
1115.3	2.50	2.49
1065.9	2.81	2.80
1016.2	3.17	3.15
1000.9	3.30	3.27
981.8	3.45	3.42

[a] Corresponds to Figure 2.11.

Table A-2.
717a Rotor Calibration Check[a].

T (°C)	log η (Pa s)	log η (Pa s)
		NIST TVF
1301.3	1.86	1.82
1301.1	1.86	1.82
1250.6	2.01	2.03
1210.9	2.22	2.20
1164.1	2.43	2.43
1111.2	2.73	2.72
1064.7	3.01	3.00
1015.4	3.34	3.34
995.8	3.48	3.48
976.0	3.63	3.63
956.2	3.79	3.79
936.3	3.95	3.96
916.5	4.13	4.14
906.7	4.23	4.23
896.8	4.33	4.33

[a] Corresponds to Figure 2.12.

Modified Spindle Calibration Checks on 710a and 717a.

Table A-3.
710a Spindle Calibration Check[a].

T (°C)	log η (Pa s)	log η (Pa s)
		NIST TVF
1502.6	0.79	0.88
1459.6	0.89	1.01
1410.6	1.06	1.17
1405.8	1.06	1.19
1361.7	1.25	1.34
1312.7	1.45	1.53
1305.5	1.47	1.55
1263.4	1.66	1.73
1213.6	1.90	1.96
1204.4	1.95	2.00
1164.2	2.16	2.21
1105.8	2.51	2.54
1014.9	3.13	3.16
965.3	3.54	3.57
915.8	4.02	4.03
901.3	4.17	4.18
891.3	4.28	4.28
866.2	4.57	4.56
851.3	4.75	4.74

[a] Corresponds to Figure 2.14.

Table A-4.
717a Spindle Calibration Check[a].

T (°C)	log η (Pa s)	log η (Pa s)
		NIST TVF
1304.8	1.84	1.80
1254.6	2.01	1.77
1213.4	2.18	1.96
1163.8	2.45	2.21
1114.1	2.72	2.49
1014.0	3.36	3.17
964.7	3.73	3.57
914.7	4.15	4.04
905.1	4.24	4.13
895.3	4.34	4.24

[a] Corresponds to Figure 2.15.